ORIGINAL PAGE IS
OF POOR QUALITY

SAMPLE

TECHNICAL REPORT STANDARD TITLE PAGE

1. REPORT NO.	2. GOVERNMENT ACCESSION NO.	3. RECIPIENT'S CATALOG NO.
4. TITLE AND SUBTITLE Application of Satellite Data in Observational and Theoretical Studies of the Evolving Structure of Baroclinic Waves		5. REPORT DATE August 1987 6. PERFORMING ORGANIZATION CODE
7. AUTHOR(S) Barry Saltzman		8. PERFORMING ORGANIZATION REPORT #
9. PERFORMING ORGANIZATION NAME AND ADDRESS Department of Geology and Geophysics Yale University P.O. Box 6666 New Haven, CT 06511		10. WORK UNIT NO. 11. CONTRACT OR GRANT NO. NAS8-34903
12. SPONSORING AGENCY NAME AND ADDRESS National Aeronautics and Space Administration Washington, D.C. 20546		13. TYPE OF REPORT & PERIOD COVERED Contractor Report 7/29/82 - 7/31/87 Final Report 14. SPONSORING AGENCY CODE

15. SUPPLEMENTARY NOTES Prepared for the Marshall Space Flight Center, AL 35812
Technical Monitors: Mr. John W. Kaufman, Dr. George H. Fichtl, and Dr. Timothy L. Miller

16. ABSTRACT

A variety of observational and theoretical studies are performed designed to clarify the relationship between satellite measurements of cloud and radiation and the evolution of transient and stationary circulations in middle latitudes. Satellite outgoing longwave radiation data are used to (1) estimate the generation of available potential energy due to infrared radiation and (2) show the extent to which these data can provide the signature of high and low frequency weather phenomena including blocking. In a significant series of studies the nonlinear, energetical, and predictability properties of these blocking situations, and the relationship of blocking to the planetary, scale longwave structure are described. These studies form the background for continuing efforts to describe and theoretically account for these low-frequency planetary wave phenomena in terms of their bimodal, "almost intransitive", properties.

On another related topic, a model containing only the essential spatial resolution, non-geostrophy, and hydrologic physics, is developed to represent the main dynamical processes involved in the formation and evolution of the "comma" type clouds commonly observed in satellite photographs. It is shown that almost all of the complex features associated with this phenomena can be deduced, encouraging the hope that simplified hydrologic considerations can be incorporated in more general low order dynamical systems models of global weather and their satellite signatures.

17. KEY WORDS	18. DISTRIBUTION STATEMENT

19. SECURITY CLASSIF. (of this report)	20. SECURITY CLASSIF. (of this page)	21. NO. OF PAGES	22. PRICE

MSFC - Form 3292 (Rev December 1972) For sale by National Technical Information Service, Springfield, Virginia 22151

Application of Satellite Data in Observational and Theoretical Studies of the Evolving Structure of Baroclinic Waves

1. Introduction

During the contract period we completed a variety of observational and theoretical studies aimed at elucidating the relationship between satellite measurements of cloud and radiation and the evolution of transient and stationary features of the circulation in middle latitudes.

In broad outline, our efforts can be divided into four main categories: (1) the application of satellite radiation data in global weather analysis, (2) studies of blocking weather patterns, (3) studies of finite amplitude baroclinic waves including hydrologic processes, and (4) the development of a low-order dynamical systems model for the nonlinear evolution of stationary and transient planetary waves. A listing of the papers published with the support of this grant, and the complementary USRA grant NAS8-34010, follows.

I. APPLICATION OF SATELLITE RADIATION DATA IN GLOBAL WEATHER ANALYSIS

1) Hansen, A.R. and R.L. Nagle, 1984: Estimates of the generation of available potential energy by infrared radiation. Mon. Weath. Rev., 112, 1370-1377.

2) Nagle, R.L., 1984: Climatological aspects of the outgoing longwave radiation field of the northern hemisphere mid-latitudes. M.S. Thesis, Yale University, pp. 59.

II. STUDIES OF BLOCKING WEATHER PATTERNS

3) Hansen, A.R. and A. Sutera, 1984: A comparison of the spectral energy and enstrophy budgets of blocking versus nonblocking periods. Tellus, 36A, 53-63.

4) Hansen, A.R. and A. Sutera, 1984: Observational aspects of the predictability of atmospheric blocking. Predictability of Fluid Motions, (G. Holloway and B.J. West, eds.) American Inst. Physics, 441-447.

5) Benzi, R., A.R. Hansen and A. Sutera, 1984: On stochastic perturbation of simple blocking models. Quart. J. Roy. Met. Soc., 110, 393-409.

6) Brown, P.S., A.R. Hansen, and J.P. Pandolfo, 1986: Circulation regime-dependent nonlinear interactions during northern hemisphere winter. J. Atmos. Sci., 43, 476-485.

III. STUDIES OF FINITE AMPLITUDE BAROCLINIC WAVES INCLUDING HYDROLOGIC PROCESSES

7) Tang, C.-M. and G.H. Fichtl, 1983: The role of latent heat release in baroclinic waves - without b-effect. J. Atmos. Sci., 40, 53-72.

8) Tang, C.-M. and G.H. Fichtl, 1984: Non-quasi-geostrophic effects in baroclinic waves with latent heat release. J. Atmos. Sci., 41, 1498-1512.

9) Saltzman, B. and C.-M. Tang, 1985: The effect of finite-amplitude baroclinic waves on passive, low-level, atmospheric constituents, with applications to comma cloud evolution. Tellus, 37A, 41-55.

10) Tang, C.-M. and B. Saltzman, 1985: Comma cloud development in a two-layer baroclinic model with vertical water vapor flux at mid-level. Papers in Meteorol. Res., 8, 45-52.

2. Summary of Research Results

In two major applications of an 8-year record of satellite-derived outgoing longwave radiation (OLR) we have (1) computed the generation of available potential energy due to infrared radiative fluxes and (2) examined the extent to which these data can provide signatures of high and low frequency weather phenomena including blocking. Using conventional temperature data along with the satellite OLR data it has been estimated by Hansen and Nagle (1984) that the global pattern of infrared radiation causes a destruction of both zonal and eddy available

potential energy of magnitudes $G_Z \sim -5.0 W\ m^{-2}$ and $G_E \sim -0.6\ w\ m^{-2}$ respectively. The destruction in the eddies is almost entirely due to the very long stationary disturbances of wavenumbers one and two. In R.L. Nagle's Masters thesis it is demonstrated that the OLR data contains the signatures of intermittent blocking phenomena embedded in higher frequency baroclinic wave activity that can be correlated with observed longwave amplified states.

Significant contributions to forming the observational foundation for a theory of blocking are provided in the sequence of papers by A.R. Hansen and collaborators. For example, Hansen and Sutera (1984a, b) show the differences in the energy and enstrophy cascades in blocking and non-blocking situations, establishing that pronounced upscale flow of <u>both</u> of these quantities, from intermediate to planetary scales, occurs during blocking episodes. The upscale flux of enstrophy, in particular, suggests that the persistence of blocking periods may be due to reduced dissipation of the large scale circulation and therefore entail some above normal predictability. The observational results (Brown, Hansen and Pandolfo 1986) also indicate that smaller scale transient eddies play an important, regime-dependent, role in interactions with atmospheric circulations on the scale of blocking.

In a theoretical study (Benzi, Hansen, and Sutera, 1984) some of the effects of these smaller scale, higher-frequency, eddies are modelled as both a stochastic white and red noise forcing of a bistable orographically induced stationary flow of the type studied by Charney and Devore. An important new time

constant thus emerges, namely the 'exit time' for reversal between the two attractor domains of the steady flow representing blocking and normal states. These exit times were found to range widely as a function of the zonal forcing, and in the red noise case it is found that the bimodal nature of the barotropic model can be obscured depending on the prescribed variance of the perturbations and the model parameters.

Our third area of work concerned the development of a minimal model of finite amplitude baroclinic waves and of their satellite signatures. These signatures usually take the form of evolving cloud patterns that, in the mature stage, often have the well-known "comma" structure. In Saltzman and Tang (1985a) we discuss the dynamical processes involved in such comma cloud formation, as well as the more general question of the redistribution of a low-level passive tracer in a growing baroclinic wave. An analytical solution has been obtained demonstrating the complex nongeostrophic flow pattern involved in (i) the redistribution of constituents trapped in the lower layers of a finite amplitude baroclinic wave, and (ii) in the formation of the typical humidity and cloud distributions in such a wave. This model is extended in Tang and Saltzman (1985b) to include the vertical flux of moisture across the middle (e.g., 500 mb) level to and from the upper level. The results show that there is a tendency for the upper-level maximum mixing ratio to shift to the east relative to the lower-level maximum mixing ratio. This is consistent with the eastward tilt with height of the common form cloud in the "cold-conveyor" cross-section and

the poleward tilt of the cloud in the "warm-conveyor" cross-section as observed by Carlson (1980).

3. Recommendations and Conclusions

The emerging results from our contract studies, and complementary work done by other scientists associated with our efforts (e.g., Sutera, Speranza, Benzi, Hansen at Control Data Corporation), provide a new outlook on the problem of low-frequency weather variability, one that offers some hope that increased predictability may be in the offing if we can properly treat the longwave bimodality that has been established. We have been pursuing this new opening vigorously under our new contract now in effect (NAS8-36356). In particular we have been developing a generalized low-order model capable of yielding solutions exhibiting bimodality in planetary wave structure along with a unimodal probability distribution in the zonal wind field. In its ultimate form this model will include explicit reference to the hydrologic processes that determine the cloud and radiative fields measureable from satellite platforms.

At the same time we have been pursuing observational studies of time-series satellite data using mathematically-sophisticated methods of attractor analysis to determine the minimum level of complexity needed to model the data and to determine the extent to which rapid transitions associated with bimodality can be identified in the data.

Results from these new approaches are not reported here, but are discussed in the Quarterly Reports of contract NAS8-36356, and in a new series of papers published, in press, or in preparation.

APPENDIX

Reprints of papers published with support of NASA contract NAS8-34903.

OBSERVATIONAL ASPECTS OF THE PREDICTABILITY OF ATMOSPHERIC BLOCKING

Anthony R. Hansen
Yale University, New Haven, CT 06511

Alfonso Sutera
Center for the Environment and Man, Inc., Hartford, CT 06120

ABSTRACT

Enstrophy and kinetic energy flux functions calculated from observed data from the winters of 1976-77 and 1978-79 are examined to compare the nonlinear cascading properties of blocking and nonblocking periods. During 1978-79 a more pronounced upscale cascade of kinetic energy as well as an upscale cascade of enstrophy from intermediate to planetary-scale wavenumbers was found during block periods as compared to nonblocking. During 1976-77, similar results appeared for a case of Rex blocking but not for the persistent, greatly amplified planetary wave pattern in January and February 1977 (as identified by Charney, et al.[1]).

The predictability time[2] based on the enstrophy flux function showed an increased predictability for the January-February 1977 event but no significant differences between the other blocking cases compared to the nonblocking sample. However, the reversal of the low wavenumber enstrophy cascade during blocking does suggest that blocking may be more persistent (due to reduced dissipation of the large-scale circulation) and therefore more predictable. Some possible implications for theoretical modelling are discussed.

INTRODUCTION

In the present study, we will attempt to identify any systematic differences in the energy and enstrophy cascading statistics of blocking events compared to nonblocking periods using data from two recent winters (1976-77 and 1978-79). It is generally accepted that the existence of persistent features such as blocking highs will allow better medium range forecast skill in numerical weather prediction models. Recently, Bengtsson[3] has shown from numerical simulations that the atmosphere is in general more predictable during blocking events than during nonblocking periods. We are interested to see if any diagnostic evidence exists for the greater predictability of blocking found by Bengtsson by qualitatively estimating a predictability time based on two dimensional turbulence theory. Although our sample is fairly small, some interesting features appear.

This report is part of a more complete set of diagnostic calculations to appear in Tellus[4].

0094-243X/84/1060441-07 $3.00

DATA AND PROCEDURES

The data used in this study are the horizontal wind (u, v) from the twice daily operational analysis of the National Meteorological Center for the winters of 1976-77 and 1978-79. Fourier coefficients of u and v were computed for every 2.5° of latitude at the 10 mandatory levels in the troposphere with the wavenumber expansion truncated after wavenumber 18.

Following Steinberg et al.[5], the kinetic energy and enstrophy flux functions can be defined as

$$\frac{\delta F_K(m)}{\delta m} = - C_K (m|n,l) \qquad (1)$$

and

$$\frac{\delta F_E(m)}{\delta m} = - C_E (m|n,l) \qquad (2)$$

assuming $F_K(0) = F_E(0) = 0$. $C_K(m|n,l)$ and $C_E(m|n,l)$ represent the gain in wavenumber m kinetic energy and enstrophy, respectively, due to nonlinear, triad interactions with all possible combinations of wavenumbers n and l. These equations were integrated from 30°N to 80°N and from 1000 mb to 100 mb.

Our primary goal is to study persistent, large-scale blocking events compared to predominantly zonal circulations which may include short duration, low amplitude, small-scale features. Therefore, we restrict ourselves to cases of stationary or slowly propagating ridges where the departure of the 500 mb height from the zonal mean, averaged over every 2.5° of latitude from 55°-80°N, exceeded 250 m for 7 days or more. Any observation not falling in a blocking period was included in the nonblocking sample.

In addition, a case of very large negative height departures occurred during January and February 1977. We will use the dates given by Charney, et al.[1] for 2 periods of persistent height departures from the climatological mean in our diagnostic calculation. Because of the existence of large amplitude features of one type or another throughout the 1976-77 winter, no nonblocking days from this winter are included in our nonblocking sample. A summary of the blocking and nonblocking days for the 2 winters is given in Table I.

Comparison of the periods of large, persistent height departures with synoptic charts indicates that these periods satisfy (for the most part) the conventional, subjective definition of blocking.

RESULTS

The results for the 1978-79 winter are given in Figure 1. Normally, enstrophy is cascaded from the longest to the shortest wavelengths[5]. This characteristic also appears in our nonblocking sample (Fig. 1a, dashed line). However, the absence of an enstrophy flux out of the lowest 5 wavenumbers during blocking and the change in sign of the enstrophy flux function near wavenumber 2 is evident

Table I Tabulation of blocking and nonblocking days from the 1978-79 winter and the 1976-77 winter determined from persistent height departures

1978-79

blocking days (90 observations)

0000 GMT 1 Dec. - 1200 GMT 7 Dec.
0000 GMT 20 Dec. - 1200 GMT 27 Dec.
1200 GMT 29 Dec. - 0000 GMT 10 Jan.
0000 GMT 14 Jan. - 1200 GMT 26 Jan.
0000 GMT 16 Feb. - 0000 GMT 22 Feb.

nonblocking days (85 observations)

0000 GMT 8 Dec. - 1200 GMT 19 Dec.
0000 GMT 28 Dec. - 1200 GMT 28 Dec.
1200 GMT 10 Jan. - 1200 GMT 13 Jan.
0000 GMT 27 Jan. - 1200 GMT 15 Feb.
1200 GMT 22 Feb. - 1200 GMT 28 Feb.

1976-77

blocking days (36 observations)

1200 GMT 11 Dec. - 0000 GMT 29 Dec.

Charney et al.[1] negative anomalies (76 observations)

30 December - 17 January
2 February - 22 February

in Fig. 1a (solid line). Also, a much larger flux of kinetic energy from the intermediate to the long waves occurred during blocking as can be seen clearly in Fig. 1b.

A comparison of the energy and enstrophy flux functions for the December 1976 case of blocking and the negative anomalies of January and February 1977 are given in Fig. 2. The December 1976 event exhibited a very striking reversal of the low wavenumber enstrophy flux function (Fig. 2a), and the same enhanced upscale kinetic energy flux as the 1978-79 blocking cases (Fig. 2b). The similarity in the behavior of Rex-type blocking in the 2 winters lends support to the significance of this result.

The January-February 1977 enstrophy flux (Fig. 2a, dashed line) is more like the 1978-79 nonblocking sample. However, notice the much lower enstrophy flux function for the January-February 1977 case in a nearly constant range from roughly wavenumbers 8 to 15. The enstrophy flux function in the same range for the December 1976 blocking case is virtually identical to the 1978-79 blocking and nonblocking samples. The kinetic energy flux for the 1977 case is dominated by exchanges amongst the lowest wavenumbers (Fig. 2b, dashed line).

It is well known that the rate of error growth in numerical

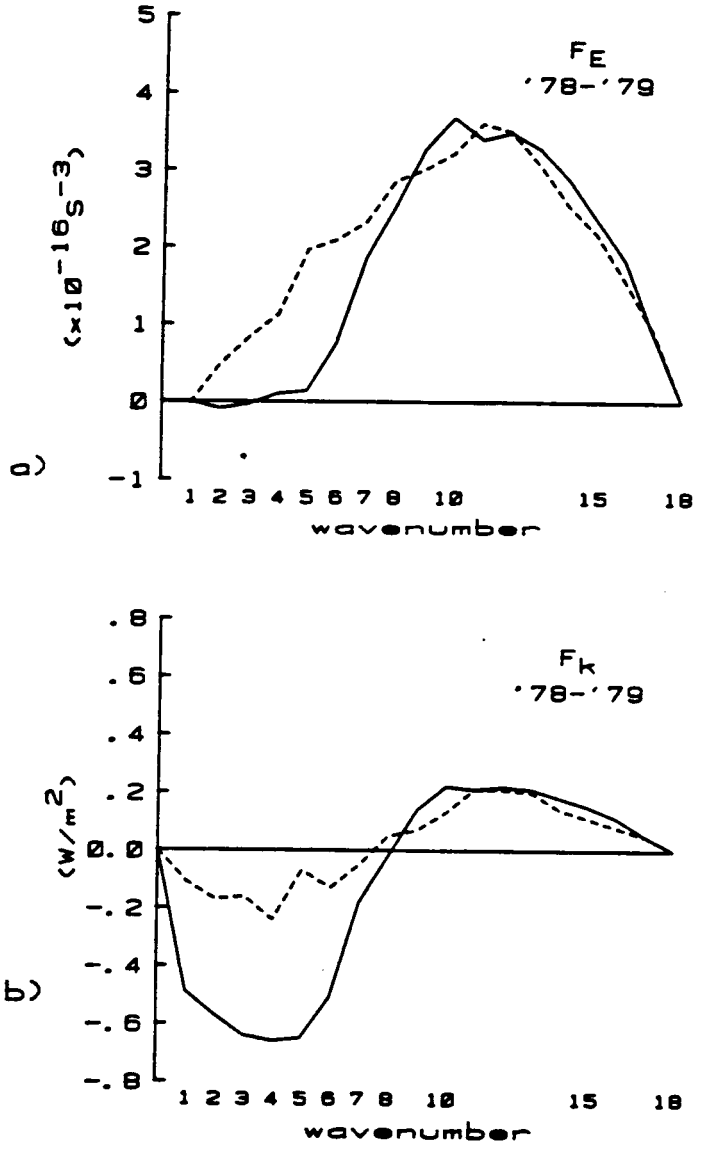

Fig. 1. The nonlinear flux functions for a) enstrophy, F_E and b) kinetic energy, F_K for blocking (solid line) and nonblocking (dashed line) for the 1978-79 winter.

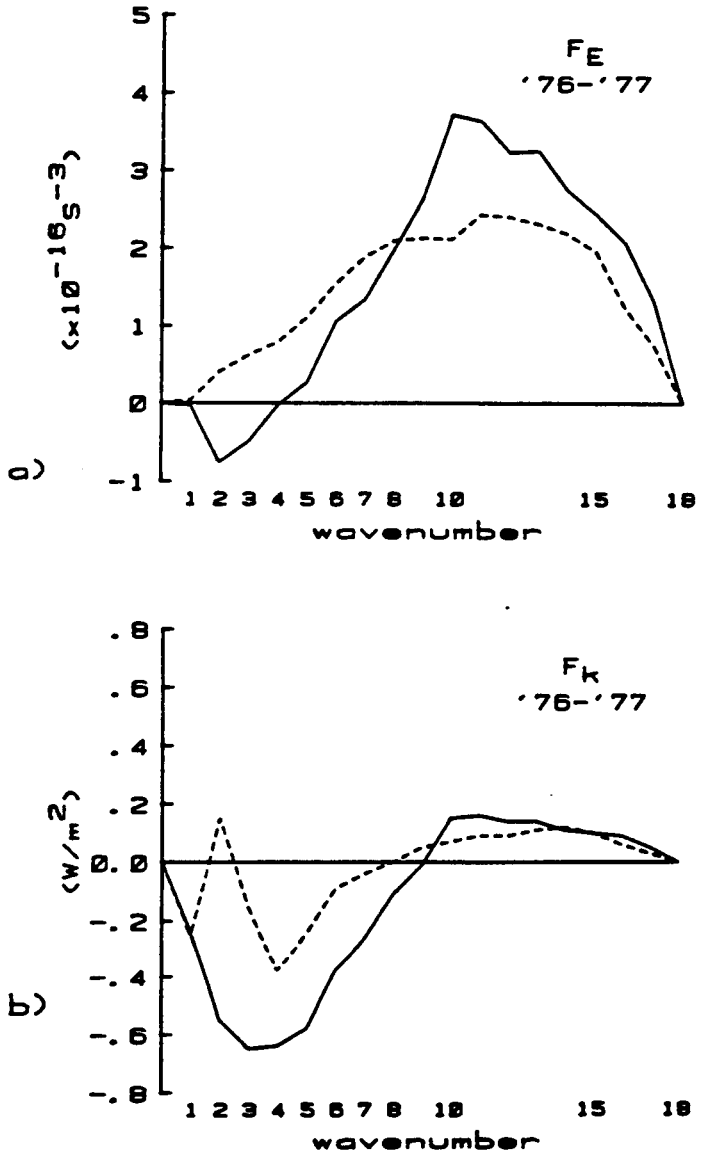

Fig. 2. The nonlinear flux functions for a) enstrophy and b) kinetic energy for the December 1976 blocking case (solid line) and the January-February 1977 negative anomalies (dashed line).

weather prediction models due to small-scale inaccuracies in the initialization can be related to the rate of downscale enstrophy cascade in a constant enstrophy flux inertial subrange of a two-dimensional turbulent fluid[6]. The characteristic time of this process can be called the predictability time and is inversely proportional to the cube root of the constant rate of enstrophy transfer to higher wavenumbers in a constant enstrophy flux inertial subrange[2,6]. The fact that the atmosphere at the larger scales behaves predominantly like a two-dimensional fluid in which the kinetic energy spectrum obeys a -3 power law [7,8,9] suggests that a qualitative estimate of the predictability time for blocking compared to nonblocking situations based on the enstrophy flux function may be made. The estimate can only be done in a qualitative way because the numerical value of the enstrophy flux function, F_E, in the constant range is dependent upon the truncation used[5]. The reason for this sensitivity is that finite amount of enstrophy is lost when the wavenumber expansion of the wind field is truncated at wavenumber 18. This will cause aliasing problems in the nonlinear enstrophy interaction in our truncated dataset that will cause changes in the shape of the enstrophy flux function at high wavenumbers. Unfortunately, the accuracy of our data at wavenumbers higher than 18 is poor so this problem cannot be alleviated. However, we will assume the values of the flux function that we have are qualitatively correct for comparison purposes.

As noted earlier, the enstrophy flux function in the constant range is nearly identical in both blocking and nonblocking situations [Figs. 1a and 2a (solid line)] suggesting no greater predictability for Rex-type blocking. However, the January-February 1977 low anomaly event exhibited a roughly 1/3 smaller enstrophy flux rate (Fig. 2a, dashed line). This result allows us to speculate that the persistent low anomalies in 1977 were inherently more predictable than either the nonblocking or Rex blocking cases.

An explanation of the greater predictability of the Rex-type blocking found by Bengtsson[2] might be found in the reversal of low wavenumber enstrophy flux function, and the absence of an enstrophy flux out of the lowest 5 wavenumbers during blocking as opposed to the normal case. This may indicate that the destruction of large-scale vorticity by down-scale cascade and eventual dissipation is greatly reduced or eliminated during blocking events. As a result, blocking patterns may be more persistent and therefore more predictable. In addition the enstrophy cascade reversal may be an indication of intermittent behavior[10] in the large-scale flow requiring no particular low wavenumber instability.

CONCLUDING REMARKS

Because of the evidently strong interaction between baroclinic cyclone-scale waves and planetary-scale waves during blocking[4,11], it would appear that theoretical models should incorporate the effects of transient, baroclinic eddies. An effort in this direction has recently been put forward by Benzi et al[12]. Using a low-order, barotropic

model[13], they suggest that the inclusion of baroclinic activity as a parameterized forcing of the mean flow (as a red process), acts to mask the role of any underlying orographic instability that otherwise might be present.

ACKNOWLEDGEMENTS

This study was supported by NASA under grant NAS8-34903 at Yale University and by the National Science Foundation under grant ATM81-06034 at the Center for the Environment and Man, Inc. Computations were performed at the National Center for Atmospheric Research which is supported by the National Science Foundation.

REFERENCES

1. J.G. Charney, J. Shukla, and K.C. Mo, J. Atmos. Sci., 38, 762 (1981).
2. D.K. Lilly in Dynamic Meteorology, edited by P. Morel (D. Reidel, Dordrecht, 1970), p. 353-418.
3. L. Bengtsson, Tellus, 33, 19 (1981).
4. A. R. Hansen and A. Sutera, Tellus (in press) (1983).
5. H.L. Steinberg, A. Wiin-Nielsen, and C.H. Yang, J. Geophys. Res., 76, 8829 (1971).
6. C.E. Leith and R.H. Kraichnan, J. Atmos. Sci., 29, 1041 (1972).
7. T.-C. Chen and J.J. Tribbia, Tellus, 33, 102 (1981).
8. P.R. Julian, W.M. Washington, L. Hembree, and C. Ridley, Jr. Atmos. Sci., 27, 376 (1970).
9. A. Wiin-Nielsen, Tellus, 19, 540 (1967).
10. G.K. Batchelor, The Theory of Homogeneous Turbulence (Cambridge University Press, Cambridge, 1960).
11. A.R. Hansen and T.-C. Chen, Mon. Wea. Rev., 110, 1146 (1982).
12. R. Benzi, A.R. Hansen, and A. Sutera, Q. J. Roy. Meteor. Soc., (submitted) (1983).
13. J.G. Charney and J.G. Devore, J. Atmos. Sci., 36, 1205 (1979).

Quart. J. R. Met. Soc. (1984), **110**, pp. 393–409 551.511.32 : 551.513.2 : 519.21

On stochastic perturbation of simple blocking models

By ROBERTO BENZI
Centro Scientifico of IBM, Rome, Italy,
ANTHONY R. HANSEN
Department of Geology and Geophysics, Yale University, New Haven, CT., USA
and
ALFONSO SUTERA*
The Center for the Environment and Man, Inc., Hartford, CT., USA

(Received 16 May 1983; revised 3 November 1983; communicated by Dr G. D. Robinson)

SUMMARY

In this paper we discuss some problems connected with the stochastic dynamics generated by the effect of small random perturbations acting on prototype equations governing large-scale flows. We focus on the features of the process which occur when the main instability is the result of orographic forcing on simple barotropic motion. In particular, we study a three-mode truncation of barotropic flow over topography when a stochastic white forcing acts on the system. We found analytical estimates of the exit times from the attraction domains of the steady solutions of the model. The exit times were found to range widely as a function of the zonal forcing.

In addition, we included a representation of the large-scale forcing in terms of a red process. We found that as a function of the variance of the perturbing process and the model's parameters, the bimodal nature of the barotropic model can be obscured.

1. INTRODUCTION

A most striking feature of complex phenomena such as atmospheric motion is the enormous number of degrees of freedom cooperating to determine a particular observed pattern. On the other hand, if we are concerned with long enough time scales, we may observe that only a few of the many degrees of freedom play a relevant role in determining the long-term patterns. It is, therefore, relevant to design a model where the large-scale, long-term behaviour is predicted by governing equations applied to a finite number of components of the system and to parametrize the short-term, smaller scales as a small, random perturbing process.

Schematically, the governing equation for the n-active components assumes the form

$$\dot{\mathbf{x}} = \mathbf{b}(\mathbf{x}) + \mathbf{W} \tag{1}$$

where x is an n-dimensional vector, b is an n-component vector field, W is a n-dimensional stochastic forcing, and the over-dot denotes a time derivative.

It is customary to measure the strength of W by its variance $E(W^2) = \varepsilon$ (ε might be time- and x-dependent), where E is the mathematical expectation operator. We recall that the total effect of W must be small, therefore ε will be assumed to be a small parameter; i.e. small in relation to certain properties associated with the nature of b.

If we consider W as a white process, (1) is a system of stochastic differential equations. Since Einstein's application of them to the theory of Brownian motion, such systems have provided a good framework for describing deterministic motion in a random environment, in particular the macroscopic variability.

Inspection of (1) reveals that the stochastic perturbations force the deterministic ($\varepsilon = 0$) motion, changing instantaneously the local (in time) behaviour of the system. However, the most important effect of their action is that, in the long term, they may dramatically change the averaged motion. These facts were discussed by Sutera (1980)

* Present address: European Centre for Medium Range Weather Forecasts, Reading.

in the framework of the Lorenz (1963) model (which remains a remarkable test-bed model for investigating features that may be important in the atmosphere). They were further considered by Moritz and Sutera (1981). Here we wish to stress a few quantitative facts that were neglected in the previously mentioned papers (which addressed different aspects of the same problem, such as the role of metastable chaos in prototype models).

If ε, as we said, is the variance of the noise, the large departures from the purely deterministic motion occur only on the time scale $O(\varepsilon^{-1}) = T_\varepsilon$. Hence, within the time interval $(0, t < T_\varepsilon)$ no appreciable differences between deterministic and stochastic behaviour would be expected. What will happen for times longer than T_ε depends again on b, i.e. on the laws governing the evolution of the averaged quantities (that is, the average taken over an ensemble of realizations of W). Since departures from this average depend on the *work done* by the random forcing against the deterministic forcing, it is of *predominant interest* to estimate this quantity. This paper is, therefore, dedicated to the calculation of the work done by stochastic perturbation of simple low-order models of orographically forced barotropic flows. We shall see that T_ε, for these models, ranges widely as a function of the zonal forcing and that the equations obtained by considering steady forcing are insufficient for the purpose of a 'realistic' description of the phenomena studied.

We suggest inclusion of a time variability of the forcing by considering it to be a red process with a given amplitude and decorrelation time. We find that, in this case, the probabilistic nature of the barotropic model may be so much changed as to obscure its bimodal structure.

2. The models

In this paper we confine our study to the behaviour of a simple barotropic orographically forced flow in a β channel and exclude models on the sphere such as those of Källen (1981, 1982) and Legras and Ghil (1983). Moreover, we will concentrate on highly truncated variants of these models, excluding studies where more modes are considered, by comparing the behaviour of two different models: those of Charney–Devore (1979) (hereafter CDV), and Egger (1982) (hereafter E).

We first write the governing equation. Let H be the mean height of a homogeneous fluid on a plane. Let y and x be the northward and eastward directions, respectively. The fluid is confined in a β channel by zonal walls at $y = 0$ and $y = \pi L$. The lower boundary elevation is described by $z = h(x, y)$. Let η be a perturbation of the upper free surface. If the motion is quasi-geostrophic then, following Charney (1974), the governing equation is given by conservation of potential vorticity

$$\frac{\partial}{\partial t}(\nabla^2\psi - \psi/\lambda^2) + J\{\psi, (\nabla^2\psi + (h/2H)f_0 + \beta y)\} = -K\nabla^2(\psi - \psi^*) \qquad (2)$$

where ∇^2 is the Laplacian operator, $\psi = g\eta/f_0$, g is the gravitational acceleration gravity, $f_0 = 2\Omega \sin\phi_0$, $\phi_0 = 45°$, $\lambda^2 = gH/f_0^2$, $\beta = (2\Omega\cos\phi_0)/a$ where a is the earth's radius and Ω the angular velocity of the earth's rotation, and $J(a, b) = (\partial a/\partial x)(\partial b/\partial y) - (\partial a/\partial y)(\partial b/\partial x)$.

The right-hand side of (2) contains the effect of Ekman dissipation $(-K\nabla^2\psi)$ and a fictitious vorticity source $(K\nabla^2\psi^*)$, simulating a large-scale forcing presumably of baroclinic nature. In reviewing the nature of low-order models, Lorenz (1982) described the procedure to be adopted for obtaining such models by starting from the continuum equations describing the fields. It consists of considering a set of orthonormal functions satisfying the same boundary conditions that the fields satisfy with the additional constraint that if f_{ni} and f_{im} are any two functions of this set then $\langle f_{ni} f_{im} \rangle = \delta_{nm}$ where the

brackets denote a horizontal average. The expansion is performed by assuming

$$\psi(x,y,t) = \sum_{mn} \psi_{nm}(t) f_{nm}. \tag{3}$$

CDV and E chose f_{nm} as the set of eigenfunctions of the Laplacian operator satisfying the condition of no normal flow at the boundaries. With this choice, the set is readily constructed with trigonometric functions. Moreover, the same set is employed in expanding the stationary forcing ψ^* and the topography h. If ψ^*_{nm} and h_{nm} are the coefficients of the expansion in ψ^* and h, by simple substitution (2) is transformed into

$$d\boldsymbol{\psi}/dt = \mathbf{b}(\boldsymbol{\psi}, \boldsymbol{\psi}^*, \mathbf{h}), \tag{4}$$

where $\boldsymbol{\psi}$, $\boldsymbol{\psi}^*$ and $\mathbf{h}$ are vectors in the infinite dimensional space spanned by f_{nm} and $\mathbf{b}$ is a vector field on it. The passage from (2) to (4) is straightforward, but the statement (3) is not because it implies that $\Sigma_{nm} f_{nm}$, whatever f_{nm} may be, is a steady solution of (2). To our knowledge there are few cases in which (2) has known steady solutions of the form (3), and they are restricted to very specific physical situations. However, it can be demonstrated that in (2) if K is very large, then asymptotically (in K) we may neglect the Jacobian term and hence the above-mentioned choice of f_{nm} is properly made.

Nevertheless, neglecting the previously discussed difficulty, (2) is transformed to the form (4). As an additional assumption to make any analysis of (4) tractable, we must require that all but a few components of the vectors $\boldsymbol{\psi}$, $\boldsymbol{\psi}^*$ and $\mathbf{h}$ be zero for all time. By employing this assumption we reduce our problem to studying a finite system of ordinary differential equations. In CDV and E only three orthonormal functions are considered, reducing the infinite system to one with only three equations. The functions are:

$$g_A = \sqrt{2}\cdot\cos(y/L), \qquad g_K = 2\cos(nx/L)\sin(y/L), \qquad g_L = 2\sin(nx/L)\sin(y/L).$$

The topography is represented by the expansion $h(x,y) = h_{01}\cos(nx/L)\sin(y/L)$.

In this paper, the stationary forcing is assumed to be $\psi^*(x,y) = \psi^*_A \cos(y/L)$. We use dimensionless time scale $\tilde{t} = t\cdot f$, space scale $\tilde{x}$ (or $\tilde{y}$) $= x$ (or y)$/L$, and $\tilde{h} = h/H$. The expansion for the dimensionless ψ is given by

$$\psi = \bar{\psi}_A g_A + \bar{\psi}_K g_K + \bar{\psi}_L g_L;$$

and the corresponding low-order model is

$$\dot{\bar{\psi}}_A = -\dot{K}(\bar{\psi}_A - \bar{\psi}^*_A) + \tilde{h}_{01}\bar{\psi}_L \tag{5a}$$

$$\dot{\bar{\psi}}_K = -b_{n1}\bar{\psi}_L - \dot{K}\bar{\psi}_K \tag{5b}$$

$$\dot{\bar{\psi}}_L = +b_{n1}\bar{\psi}_K - \dot{K}\bar{\psi}_L - \tilde{h}_{n1}\bar{\psi}_A \tag{5c}$$

where

$$\tilde{h}_{01} = (\gamma_{n1}/(1+\lambda^{-2}))(h_{01}/2H) \qquad \tilde{h}_{n1} = (\gamma_{n1}/(n^2+1+\lambda^{-2}))(h_{01}/2H)$$

$$b_{n1} = \alpha_{n1}\bar{\psi}_A - \beta_{n1} \qquad \alpha_{n1} = (8\sqrt{2}/3\pi)(n^3/(n^2+1))$$

$$\beta_{n1} = (L/a)(n/(n^2+1))\cot\phi_0 \qquad \gamma_{n1} = (8\sqrt{2}/3\pi)n.$$

Hereafter we choose $n = 2$, $\dot{K} = 10^{-2}$ and $L/a = \frac{1}{2}$, as in CDV. The form of system (5) is a feature common to E.

Since we force the barotropic flow only in its zonal component, it is legitimate to consider stochastic perturbations only on that component. We notice that in this case

the stochastic forcing acts on the total angular momentum only and this assumption might be considered unrealistic. However, recent observations (Barnes *et al.* 1983) seem to indicate that, besides its well-known seasonal oscillations, the total angular momentum is randomly fluctuating with an amplitude even larger than the one here assumed.

Of course, a more realistic assumption would consist of stochastically perturbing the wave equations (i.e. ψ_K and ψ_L) also; for the sake of simplicity we restrict ourselves in forcing only the mean flow. By choosing a Wiener process as the perturbing random force, system (5) describes a diffusion process. In the next section we shall study it in detail for the CDV model. The results carry over identically to the E case. Henceforth, we will drop the overbar notation for dimensionless quantities.

3. Diffusion against the flow

It is known that the model (5) exhibits multiple equilibria, specifically that the steady-state equations possess three solutions $\mathbf{x}_b$, $\mathbf{x}_{in}$, and $\mathbf{x}_z$, where $\mathbf{x} \equiv (\psi_A, \psi_K, \psi_L)$, for selected values of the mountain height h and driving forcing ψ_A^*. Moreover, $\mathbf{x}_b$ and $\mathbf{x}_z$ are asymptotically stable solutions, and $\mathbf{x}_{in}$ is an unstable one. If D_1 and D_2 are the attraction domains of $\mathbf{x}_b$ and $\mathbf{x}_z$ respectively, then an initial condition chosen in D_1 or D_2 will approach $\mathbf{x}_b$ or $\mathbf{x}_z$ respectively (see Fig. 1).

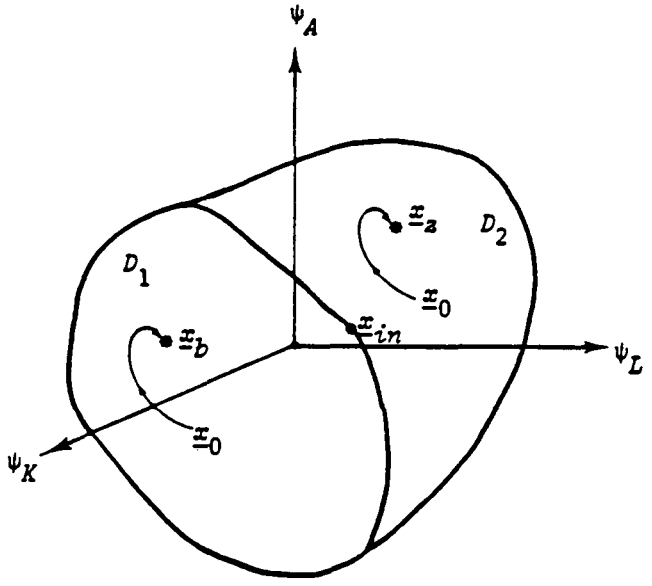

Figure 1. Schematic diagram of the phase space for the CDV model. The symbols are explained in the text.

The effect of stochastic forcing on time scales T_ε will be to drive trajectories starting from any initial conditions to points outside the domain of attraction to which those initial conditions belong. How do the trajectories behave for small ε?

For $\mathbf{x}_0$ in D_1, $\mathbf{x}(t)$ will roll down into a neighbourhood of $\mathbf{x}_b$ along the deterministic trajectory. The trajectories then stay in a small neighbourhood of $\mathbf{x}_b$, making excursions to other points of D_1 from time to time and returning. Finally, after a long time, T_ε, the trajectory deviates so far from $\mathbf{x}_b$ that it goes over into D_2 and rolls down into a neighbourhood of $\mathbf{x}_z$. Then the process will begin again. This process is completely described by the joint probability distribution P. Recalling that the noise acts only on

ψ_A, the Fokker–Planck equation for P is

$$\partial P(\psi_A, \psi_K, \psi_L, t)/\partial t = \tfrac{1}{2}\varepsilon \partial^2 P/\partial \psi_A^2 - \operatorname{div}(\mathbf{b} \cdot P) \tag{6}$$

where $\mathbf{b} = \{-K(\psi_A - \psi_A^*) + h_{01}\psi_L, -K\psi_K - b_{n1}\psi_L, -K\psi_L + b_{n1}\psi_K - h_{n1}\psi_A\}$, and div is the three-dimensional divergence operator defined in the (ψ_A, ψ_K, ψ_L) space. E solves (6) by numerical integration.

In this paper we will try to estimate P in a different fashion. First we notice that two time scales are present in our system, namely $1/K$ and $1/\varepsilon$. If $1/K \ll 1/\varepsilon$, in the sense discussed in appendix A, the asymptotic behaviour of our problem is approximated by the single stochastic differential equation

$$d\psi_A = -(\partial V/\partial \psi_A)dt + \varepsilon^{1/2} dW \tag{7}$$

where $V(\psi_A)$ is given by

$$\begin{aligned} V(\psi_A) &= -\int F(\psi_A) d\psi_A \\ &= -\int [\{-(\psi_A - \psi_A^*)K^2 - b_{n1}^2(\psi_A - \psi_A^*) - h_{n1}h_{01}\psi_A\}/(2K + b_{n1}^2/K)] \cdot d\psi_A. \end{aligned} \tag{8}$$

In appendix A we propose a way to obtain (7) by employing a technique resembling the diffusion limit of the theory of stochastic differential equations (Schuss 1980, pp. 132–134). We are aware that to solve our problem, other asymptotic techniques are available (Schuss 1980), and we have employed them finding the same result. Since our purpose is to use our result for a wide range of the parameters (leaving, however, K and ε unchanged), we have tested our approximation numerically and the results are presented in appendix B. It appears from these results that the approximation is valid. The situation described by the approximation (7) is identical to the one discussed by Sutera (1981) and the steady joint probability distribution is given by

$$P(\psi_A) = N' \exp(-2V(\psi_A)/\varepsilon) \tag{9}$$

where N' is a normalization constant.

However, for (7), in the limit $\varepsilon \to 0$, a very important statistical quantity can be calculated. Let us consider the process $\tau_b(\mathbf{x}_b, \mathbf{x})$ defined by

$$\tau_b(\mathbf{x}_b, \mathbf{x}) \doteq \{\text{if } \mathbf{x}(0) \text{ is in } D_1, \mathbf{x}(\tau_b) \text{ is not in } D_1\}, \tag{10a}$$

τ_b being the exit time of the process starting in D_1. Analogously, $\tau_z(\mathbf{x}_z, \mathbf{x})$ is defined by

$$\tau_z(\mathbf{x}_z, \mathbf{x}) \doteq \{\text{if } \mathbf{x}(0) \text{ is in } D_2, \mathbf{x}(\tau_z) \text{ is not in } D_2\}. \tag{10b}$$

As discussed in Sutera (1981) for the case of three steady states of which two are stable solutions and the third is an unstable one as in (7), the following estimations of the expectation value of the exit times hold:

$$E\{\tau_b(\psi_A^b, \psi_A)\} \leqslant E\{\tau_b(\psi_A^b, \psi_A^{in})\} \simeq \pi |V''(\psi_A^b) \cdot V''(\psi_A^{in})|^{-1} \exp(2\Delta_1 V/\varepsilon) \tag{11a}$$

$$E\{\tau_z(\psi_A^z, \psi_A)\} \leqslant E\{\tau_z(\psi_A^z, \psi_A^{in})\} \simeq \pi |V''(\psi_A^z) \cdot V''(\psi_A^{in})|^{-1} \exp(2\Delta_2 V/\varepsilon) \tag{11b}$$

where ψ_A^b, ψ_A^z, ψ_A^{in} are the blocking, zonal, and intermediate equilibria, respectively, V'' denotes the second derivative of V with respect to ψ_A calculated at the arguments, $\Delta_1 V = |V(\psi_A^b) - V(\psi_A^{in})|$ and $\Delta_2 V = |V(\psi_A^z) - V(\psi_A^{in})|$. (Equations (11a, b) hold for the limit $\varepsilon \to 0$. Benard LeGras (private communication) has calculated the next order

(in $1/\varepsilon$) correction for larger ε. We have not employed his correction in this paper in order to limit its length. We thank LeGras for his communication.)

Equation (9), together with (11a, b), allow exploration of the parameter space on which $V(\psi_A)$ depends. Here the main differences between this work and E are found. In concluding this section we are amused to remark that the main approximation employed (i.e. Eq. (7)) has been assumed valid in the same spirit in which the orthonormal basis has been chosen. In fact, the equation

$$J(\psi, \nabla^2\psi + f_0 h/H + \beta y) = -K(\nabla^2\psi - \nabla^2\psi^*) \tag{12}$$

in the limit $1/K \to 0$, converges to

$$\nabla^2(\psi - \psi^*) = 0. \tag{13}$$

Therefore, eigenfunctions of the Laplacian are also steady solutions of (2) in this limit.

4. Exploring the parameter space

In this section we employ the analytical formulas developed in the previous section (and verified in appendix B) to study the parameter space on which the models of CDV and E depend. We choose to study the behaviour of the exit time and probability distributions as functions of h_{01}/H and the zonal forcing (ψ_A^* or u_0^* for E case). Hence all the other parameters are left unchanged from the ones adopted by CDV and E.

TABLE 1. Barrier heights and exit times for the Charney-DeVore model as a function of the zonal forcing. ψ_A^*

ψ_A^* (n.d.)	$V(1) - V(2)$ ($\times 10^{-5}$)	$V(2) - V(3)$ ($\times 10^{-5}$)	τ (block) (days)	τ (zonal) (days)
(a) $h_{01}/H = 0{\cdot}05$				
0·10	2·17	0·004	76·6	180·1
0·12	1·76	0·61	18·1	43·6
0·14	1·48	1·79	10·8	49·8
0·16	1·24	3·43	7·6	79·2
0·18	1·05	5·51	5·8	159·5
0·20	0·88	8·02	4·6	395·6
0·22	0·73	11·00	3·9	$1{\cdot}2 \times 10^3$
0·24	0·61	14·30	3·4	$4{\cdot}3 \times 10^3$
0·26	0·49	18·10	3·0	$1{\cdot}8 \times 10^4$
0·28	0·40	22·20	2·8	$9{\cdot}6 \times 10^4$
0·30	0·31	26·80	2·7	$5{\cdot}8 \times 10^5$
(b) $h_{01}/H = 0{\cdot}10$				
0·14	11·10	0·13	$1{\cdot}3 \times 10^3$	81·9
0·16	10·40	1·15	532·7	59·6
0·18	9·83	2·78	298·8	84·7
0·20	9·30	4·91	189·3	164·0
0·22	8·83	7·52	128·7	402·9
0·24	8·40	10·60	92·0	$1{\cdot}2 \times 10^3$
0·26	8·01	14·10	68·1	$4{\cdot}4 \times 10^3$
0·28	7·64	18·00	51·8	$1{\cdot}9 \times 10^4$
0·30	7·30	22·40	40·4	$1{\cdot}1 \times 10^5$
0·32	6·98	27·20	32·1	$6{\cdot}7 \times 10^5$

The indices 1, 2, 3 refer to blocking, orographic instability, and zonal steady states. τ (block) and τ (zonal) are the times for the blocking-to-zonal and zonal-to-blocking transitions, respectively.

TABLE 2. BARRIER HEIGHTS AND EXIT TIMES FOR THE EGGER MODEL AS A FUNCTION OF THE ZONAL FORCING. u_0

u_0^* (m s^{-1})	$V(1)-V(2)$ ($\times 10^{-5}$ m^2 s^{-1})	$V(2)-V(3)$ ($\times 10^{-5}$ m^2 s^{-1})	τ (block) (days)	τ (zonal) (days)
(a) $h_{01}/H = 0{\cdot}05$				
7·0	0·94	0·13	18·6	57·1
8·0	0·80	0·47	12·1	43·2
9·0	0·69	0·95	9·0	41·8
10·0	0·59	1·55	7·4	45·9
11·0	0·52	2·27	6·2	55·1
12·0	0·44	3·10	5·5	70·7
13·0	0·38	4·04	5·0	96·4
14·0	0·32	5·09	4·6	139·3
15·0	0·27	6·25	4·3	212·5
(b) $h_{01}/H = 0{\cdot}10$				
10·0	6·01	0·02	216·8	159·7
11·0	5·67	0·32	92·7	65·6
12·0	5·39	0·84	62·2	58·1
13·0	5·15	1·52	46·1	62·4
14·0	4·92	2·34	35·6	74·1
15·0	4·72	3·29	28·9	96·4
16·0	4·53	4·36	23·6	133·8
17·0	4·36	5·50	20·0	196·0
18·0	4·19	6·64	17·0	289·8

The indices 1, 2, 3 refer to blocking, orographic instability, and zonal steady states. τ (block) and τ (zonal) are the times for the blocking-to-zonal and zonal-to-blocking transitions, respectively.

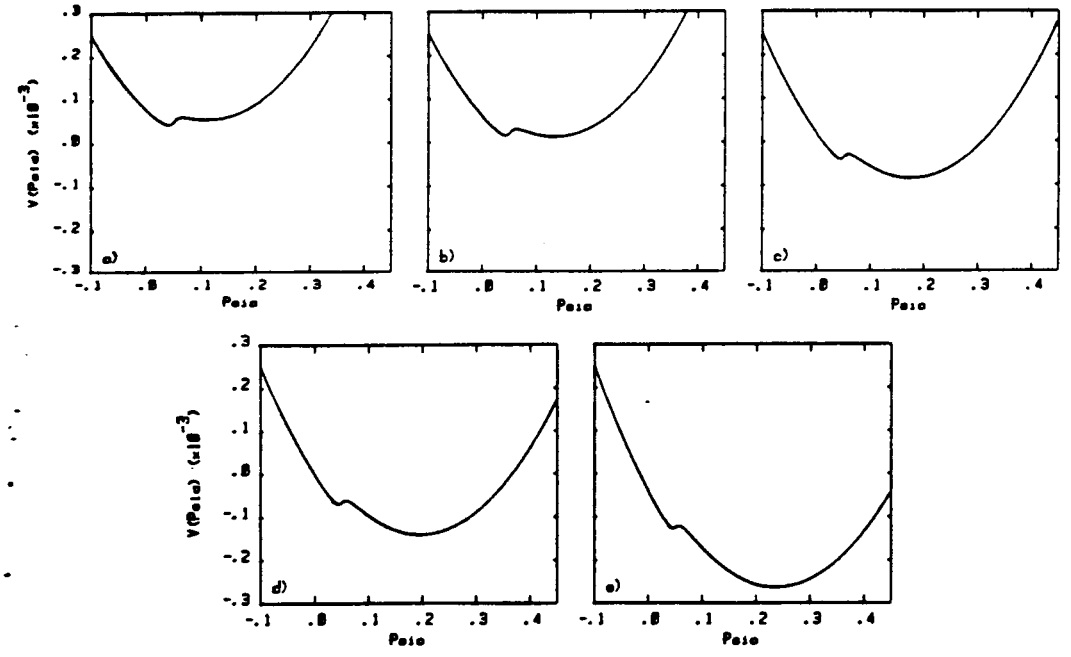

Figure 2. The CDV model potential, $V(\psi_A)$, for $h_{01}/H = 0{\cdot}05$ as a function of the zonal forcing ψ_A^*. (a) $\psi_A^* = 0{\cdot}12$; (b) $\psi_A^* = 0{\cdot}14$; (c) $\psi_A^* = 0{\cdot}18$; (d) $\psi_A^* = 0{\cdot}20$, (e) $\psi_A^* = 0{\cdot}24$. *Psia* denotes ψ_A.

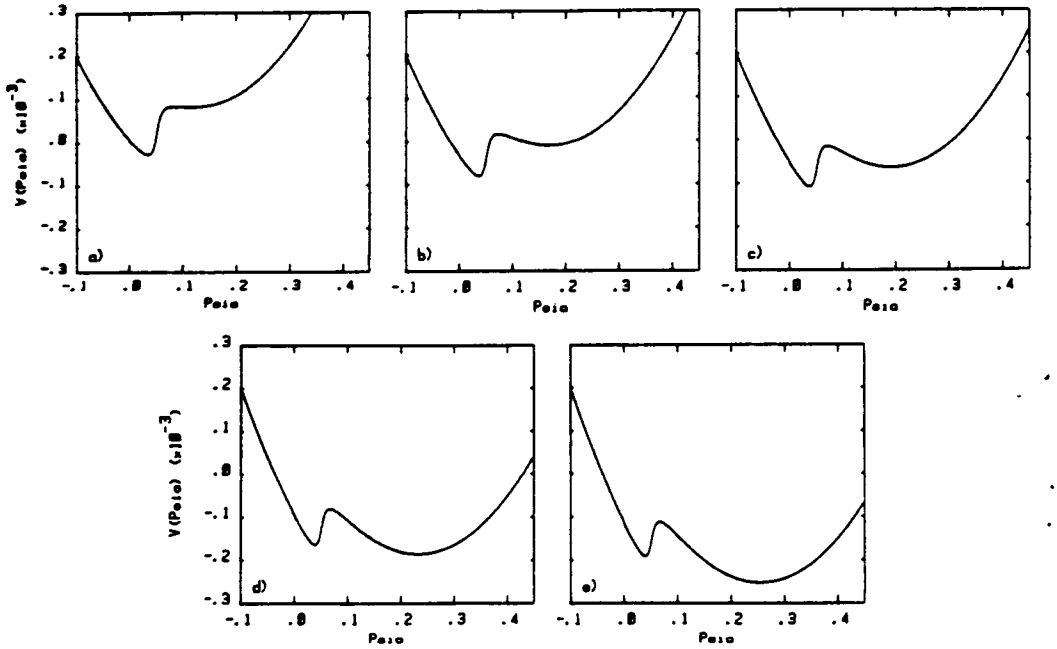

Figure 3. The CDV model potential, $V(\psi_A)$, for $h_{01}/H = 0{\cdot}10$ as a function of the zonal forcing ψ_A^*. (a) $\psi_A^* = 0{\cdot}14$; (b) $\psi_A^* = 0{\cdot}18$; (c) $\psi_A^* = 0{\cdot}20$; (d) $\psi_A^* = 0{\cdot}24$; (e) $\psi_A^* = 0{\cdot}26$.

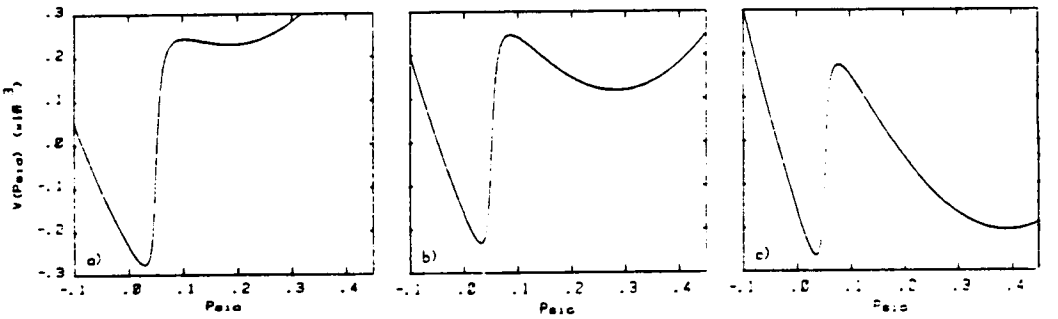

Figure 4. The CDV model potential $V(\psi_A)$, for $h_{01}/H = 0{\cdot}20$ as a function of the zonal forcing ψ_A^*. (a) $\psi_A^* = 0{\cdot}22$; (b) $\psi_A^* = 0{\cdot}30$; (c) $\psi_A^* = 0{\cdot}40$.

Moreover, the noise level in dimensionless units has been fixed following E as $\varepsilon = 5 \times 10^{-5}$. The results are reported in Tables 1(a) and (b) for the CDV case (where a transformation into natural units has been performed for the exit times), and Tables 2(a) and (b) for the E case. Figures 2 to 4 contain the potential $V(\psi_A)$ for the CDV cases (the E case does not present remarkable differences). It can be noticed that the basin of attraction of the zonal state is a very shallow one. The feature has been captured by employing the term $\{2K + (b_{n1}b_{n1})/K\}$ as a weighting factor.

Recently, Dole and Gordon (1983) analysed the statistical nature of anomalies in the atmosphere and found that potentials of the nature presented here would fit the data. However, according to Dole and Gordon a shallow basin would describe a 'blocked' circulation rather than the zonal one we found.

5. The inclusion of red noise

A first look at the tables presented in the previous section shows that although there are combinations of parameters which make the models quite attractive, slight changes in the zonal forcing are able to change interesting quantities such as exit times in a dramatic fashion.

Barotropic models have been employed traditionally to gain a first insight into the phenomena under investigation. The need for a better modelling of the zonal forcing is a peculiar characteristic of these models and since the fictitious source of vorticity corresponds to no particular physical process in the governing equation, we may speculate about its nature.

A possible assumption may be formulated by considering this forcing to be a stochastic process obeying a stochastic equation. In this section, we shall consider the case when the zonal forcing, ψ_A^*, is itself the solution of a stochastic process. We will model ψ_A^* by employing a forcing with a red spectrum. This case has relevance in our problem because in the atmosphere this forcing may be associated with baroclinic processes. There is some observational evidence that blocking events are initiated and influenced by a forcing from transient, baroclinic, cyclone-scale waves (see Hansen and Chen 1982; Hansen and Sutera 1984).

For simplicity we postulate that

$$\psi_A^* = \bar{\psi}_A^* + y + (\varepsilon^{\frac{1}{2}}/K)dW \tag{14}$$

with ε as previously defined and $\bar{\psi}_A^*$ a constant. Let us assume that y obeys

$$dy = -\Delta\omega\, y\, dt + (\varepsilon_1 \Delta\omega)^{\frac{1}{2}} dW. \tag{15}$$

Hence the process y will be an Ornstein–Uhlenbeck process (see, for example, Sutera 1981) with decorrelation time $1/\Delta\omega$.

We shall study the following problem:

$$d\psi_A = -\{\partial V(\psi_A; \psi_A^*, y)/\partial\psi_A\}dt + \varepsilon^{\frac{1}{2}} dW \tag{16a}$$

$$dy = -\Delta\omega\, y\, dt + (\varepsilon_1 \Delta\omega)^{\frac{1}{2}} dW. \tag{16b}$$

If $\Delta\omega \gg \varepsilon_1$, then on time scales $O(\varepsilon_1^{-1})$ the process y may be considered δ-correlated; i.e.

$$E[y] = 0 \tag{17a}$$

$$E[y(t)y(0)] = (\varepsilon_1/2\Delta\omega)\,\delta(t), \tag{17b}$$

and it is Gaussian. Hence, (16a, b) reduce to

$$d\psi_A = \bar{\bar{F}}\, dt + g(\psi_A) y\, dt + \varepsilon^{\frac{1}{2}} dW. \tag{18}$$

The functions $\bar{\bar{F}}$ and g are defined as follows:

$$\bar{\bar{F}} = (-K^2(\psi_A - \bar{\psi}_A^*) - b_{n1}^2(\psi_A - \bar{\psi}_A^*) - h_{01}h_{n1}\psi_A)(2K + b_{n1}^2/K)^{-1} \tag{19a}$$

$$g(\psi_A) = (K^2 + b_{n1}^2)(2K - b_{n1}^2/K)^{-1}. \tag{19b}$$

In (18) the stochastic forcing enters in a twofold way. We have additive ($\varepsilon^{\frac{1}{2}} dW$) and multiplicative ($g(\psi_A)y$) sources. In the limit described by (17a, b), the appropriate

Fokker–Planck equation corresponding to (18) is given by (see Schuss 1980, p. 95)

$$\frac{\partial}{\partial t}P = -\frac{\partial}{\partial \psi_A}\left(\bar{\bar{F}} + \frac{\varepsilon_1}{2\Delta\omega}\frac{\partial}{\partial \psi} g^2(\psi_A)\right)P + \frac{1}{2}\frac{1}{2\Delta\omega}\frac{\partial^2}{\partial \psi_A^2}(R + g^2(\psi_A))P \tag{20}$$

where $R = 2\Delta\omega\varepsilon/\varepsilon_1$. A stationary solution of (20) is

$$P_s(\psi_A) = \frac{1}{(R + g^2(\psi_A))^{\frac{1}{2}}} \exp\frac{4\Delta\omega}{\varepsilon_1}\int \frac{\bar{\bar{F}}}{R + g^2(\psi_A)}\, d\psi_A. \tag{21}$$

We plot the probability distribution, $P(\psi_A)$, obtained from (9) where only additive white noise is present ($\varepsilon = 5 \times 10^{-5}$) compared with that obtained from (21) in Figs. 5(a) and 5(b), respectively. In Fig. 5(b) we have taken $\varepsilon_1 = 2 \times 10^{-4}$, $\Delta\omega = 0{\cdot}02$ (corresponding to a decorrelation time of ~5 days) and $\varepsilon = 5 \times 10^{-5}$. The inclusion of both multiplicative and additive noise (Fig. 5(b)) has the effect of leaving the maximum

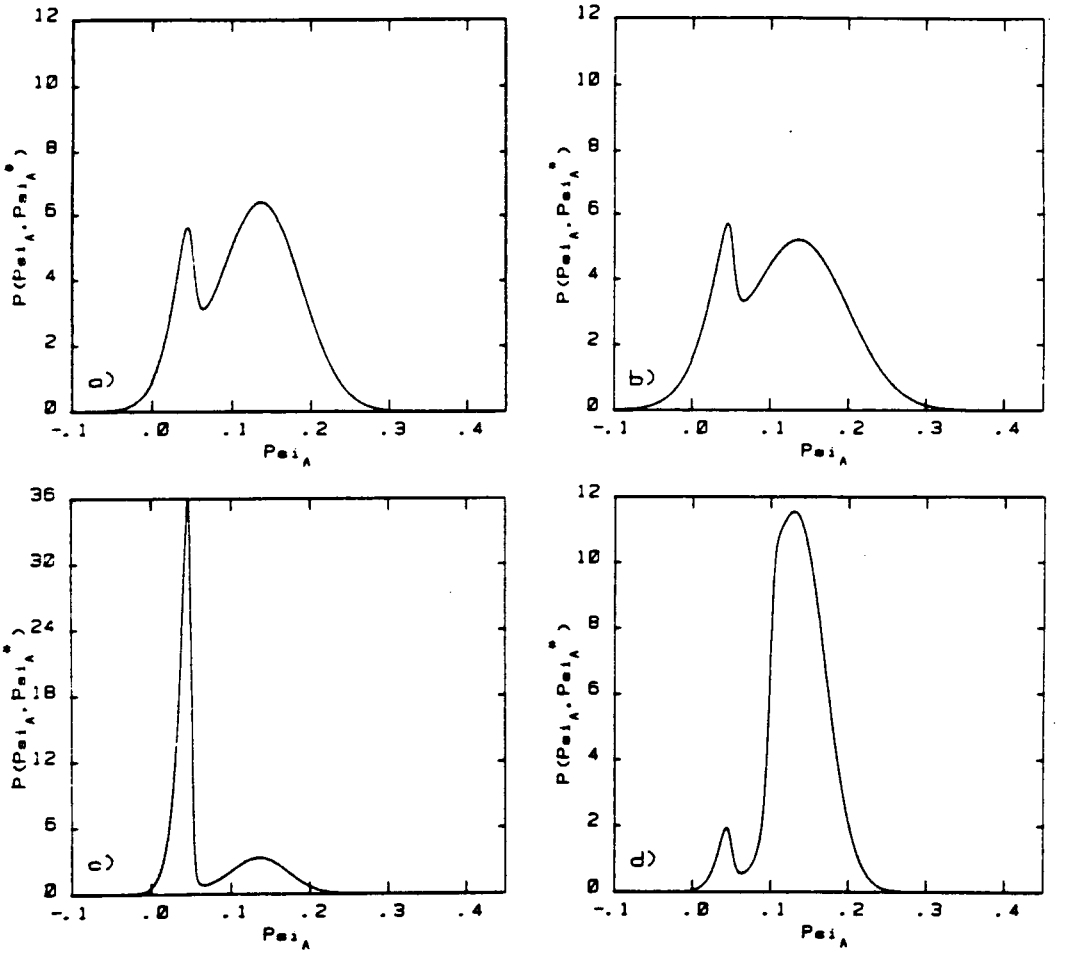

Figure 5. Normalized probability distribution for the parameters $\bar{\bar{\psi}}_A^* = 0{\cdot}14$, $h_{01}/H = 0{\cdot}05$ and $K = 0{\cdot}01$. (a) $P(\psi_A)$ from (9) with $\varepsilon = 5 \times 10^{-5}$; (b) $P_s(\psi_A)$ from (21) with $\varepsilon = 5 \times 10^{-5}$, $\varepsilon_1 = 2 \times 10^{-4}$ and $\Delta\omega = 0{\cdot}02$; (c) $P_s(\psi_A)$ with $\varepsilon_1 = 2 \times 10^{-4}$, $\Delta\omega = 0{\cdot}02$ but with $\varepsilon = 0$ (i.e. no additive noise); and (d) same parameters as (b) but where $g(\psi_A)$ has its minimum on the zonal side of the instability. (This change was obtained by setting $\alpha_{n1} = 1$ and is intended as an illustration only.)

likelihood of the blocked state unchanged while reducing the maximum likelihood of the zonal circulation compared with a system in which only additive white noise is present (Fig. 5(a)). This effect is associated with the function b_{n1}. In fact, the function $g(\psi_A)$ has a minimum where $b_{n1} = 0$, namely, where $\psi_A = (\beta_{n1}/\alpha_{n1})$. This value of ψ_A lies between the blocking equilibrium and the orographic instability. Therefore, if only red noise is present (Fig. 5(c)), the process will tend to remain on the blocked side of the double potential well. All this is expressed by (21) and confirmed by numerical calculation (not shown). If the point where $g(\psi_A)$ is minimum fell on the zonal side of the orographic instability, the system would tend to remain in a zonal configuration (Fig. 5(d)) in the absence of additive white noise ($\varepsilon = 0$). Extended numerical integrations of both the approximation (16a, b) and the full CDV mode (5) in which ψ_A^* is modelled as in (14) yield histograms of the residence density of ψ_A that are qualitatively similar to the analytical results presented in Figs. 5(a) to (d).

These results lead to some speculation about the nature of an atmospheric signal. According to the simple barotropic model proposed by CDV, we should expect that such a signal would be bimodal. However, if we record this signal in a baroclinic environment as in the atmosphere, it is not obvious that such bimodality should be observable unless we were able to filter the red component of the signal. Hansen and Sutera (1983) compared statistics for blocking and non-blocking periods and, although no evidence of bimodality was present in their statistics, active baroclinic processes were present both during blocking and non-blocking periods. Thus, in the context of the results presented here, this baroclinic activity might mask the effect of an underlying barotropic mechanism which would otherwise generate a bimodal signal.

6. Concluding remarks

We have presented a set of results concerning the use of stochastic perturbations in simple models of barotropic flow over large-scale topography. We found that stochastic forcing may drive the motion against the deterministically stable flow. We were able to calculate the rate at which different equilibria would be visited as a function of the models' parameters. If we interpret the multiple equilibria of these models to represent different equilibrium states of the atmospheric circulation (e.g. low and high index equilibria), the following conclusions may be drawn from our calculation:

First, the exit time calculations show that such equilibria may be so energetically separated that the distribution of their occurrences may be meaninglessly uneven. Moreover, even when their exit times are roughly in agreement with the observed duration of these patterns, a small change in the external, large-scale flow forcing has a dramatic effect. When the dynamics of the forcing are simulated by some red process, we noticed that the bimodality of the probability distribution may be obscured.

Acknowledgments

We are grateful to Dr G. D. Robinson and Prof. B. Saltzman for reviewing and improving the original manuscript, and to Ms M. G. Atticks for editing and preparing the final submission. We thank Prof. M. Ghil and Drs C. Leith and P. Thompson for discussions. One of us (Sutera) presented part of the contents of this paper during seminars held at the Laboratoire de Meteorologie Dynamique of CNSR and at the Courant Institute of Mathematical Sciences. He is grateful to these institutions and their members for the warm hospitality and useful comments. This paper has been supported

by the division of Atmospheric Sciences, National Science Foundation under grant ATM81-06034 at the Center for the Environment and Man, Inc., grant ATM70-25013 at Yale University, and by the National Aeronautical and Space Administration under grant NAS 8-34903 at Yale University.

APPENDIX A

In this appendix we describe the procedure used in deriving Eq. (7). The model is

$$\dot{\psi}_A = -K(\psi_A - \psi_A^*) + h_{01}\psi_L + \varepsilon^{\frac{1}{2}}\dot{W} \tag{A.1a}$$

$$\dot{\psi}_K = -K\psi_K - b_{n1}\psi_L \tag{A.1b}$$

$$\dot{\psi}_L = -K\psi_L + b_{n1}\psi_K - h_{n1}\psi_A. \tag{A.1c}$$

We introduce the transformation

$$\eta = -K(\psi_A - \psi_A^*) + h_{01}\psi_L. \tag{A.2}$$

In these new coordinates, the system (A,1a, b, c) transforms into

$$\dot{\psi}_A = \eta + \varepsilon^{\frac{1}{2}}\dot{W} \tag{A.3a}$$

$$\dot{\psi}_K = -K\psi_L - (b_{n1}/h_{01})\{\eta + K(\psi_A - \psi_A^*)\} \tag{A.3b}$$

$$\dot{\eta} = -2K\eta - K^2(\psi_A - \psi_A^*) + b_{n1}h_{01}\psi_K - h_{01}h_{n1}\psi_A - K\varepsilon^{\frac{1}{2}}\dot{W} \tag{A.3c}$$

We notice that in (A.3a, b, c) two time scales are involved, namely K and ε. Moreover, K/ε is a large parameter ($O(10^3)$) using the values considered in the text.

Setting $\tau = \varepsilon t$, the previous system is transformed to

$$\dot{\psi}_A = (1/\varepsilon)\eta + \dot{W} \tag{A.4a}$$

$$\dot{\psi}_K = -(K/\varepsilon)\psi_K - (b_{n1}/\varepsilon h_{01})\{\eta + K(\psi_A - \psi_A^*)\} \tag{A.4b}$$

$$\dot{\eta} = -(2K/\varepsilon)\eta - (1/\varepsilon)\{-K^2(\psi_A - \psi_A^*) + b_{n1}h_{01}\psi_K - h_{01}h_{n1}\psi_A\} - K\dot{W} \tag{A.4c}$$

where the fact $\dot{W}(t) = \dot{W}(\tau/\varepsilon) = \varepsilon^{\frac{1}{2}}\dot{W}(\tau)$ has been used. We may formally integrate (A.4a) to obtain (all integrals run from 0 to τ)

$$\psi_A = \psi_0 + (1/\varepsilon)\int \eta\, ds + \int \dot{W}\, ds. \tag{A.5}$$

Let

$$\eta = x + y \tag{A.6}$$

where

$$dy/d\tau = -(2K/\varepsilon)y + K\dot{W}(\tau) \tag{A.7a}$$

and

$$y(0) = \eta(0), \tag{A.7b}$$

then

$$d\eta/d\tau = dy/d\tau + dx/d\tau = -(2K/\varepsilon)y + K\dot{W} + dx/d\tau. \tag{A.8}$$

It follows that

$$dx/d\tau = (2K/\varepsilon)y - K\dot{W} - (2K/\varepsilon)\eta - \\ - (1/\varepsilon)\{-K^2(\psi_A - \psi_A^*) + b_{n1}h_{01}\psi_K - h_{01}h_{n1}\psi_A\} + K\dot{W} \tag{A.9}$$

or

$$(dx/d\tau) = -(2K/\varepsilon)x - (1/\varepsilon)\{-K^2(\psi_A - \psi_A^*) + b_{n1}h_{01}\psi_K - h_{01}h_{n1}\psi_A\}. \quad \text{(A.10)}$$

Equation (A.10) has the solution

$$x = \int \exp\{-(2K/\varepsilon)(\tau - s)\} \times \times [-(1/\varepsilon)\{-K^2(\psi_A - \psi_A^*) + b_{n1}h_{01}\psi_K - h_{01}h_{n1}\psi_A\}]\, ds. \quad \text{(A.11)}$$

On the other hand, the solution of (A.7a, b) is

$$y = \exp\{-(2K/\varepsilon)\tau\}y(0) + \tfrac{1}{2}\varepsilon(2K/\varepsilon)\exp\{-(2K/\varepsilon)\tau\}\int \exp\{(2K/\varepsilon)r\}\dot{W}(r). \quad \text{(A.12)}$$

Now let us recall that $\dot{W}$ is not a differential function; hence the last integral of (A.12) must be evaluated by parts. It follows that

$$\begin{aligned}
&\tfrac{1}{2}\varepsilon(2K/\varepsilon)\exp\{-(2K/\varepsilon)\tau\}\int \exp\{(2K/\varepsilon)r\}\dot{W}(r) \\
&\quad = \tfrac{1}{2}\varepsilon[\exp\{-(2K/\varepsilon)\tau\}|(2K/\varepsilon)\exp\{(2K/\varepsilon)r\}W(r)|_0^{\tau} - \\
&\qquad - \exp\{-(2K/\varepsilon)\tau\}(4K^2/\varepsilon^2)\int \exp\{(2K/\varepsilon)r\}W(r)\,dr] \quad \text{(A.13)} \\
&\quad = \tfrac{1}{2}\varepsilon[(2K/\varepsilon)W(\tau) - \exp\{-(2K/\varepsilon)\tau\}(4K^2/\varepsilon^2)\int \exp\{(2K/\varepsilon)r\}W(r)\,dr].
\end{aligned}$$

Substituting (A.13), (A.12) and (A.11) in (A.6), and taking into account (A.7b), we have

$$\begin{aligned}
\eta = {} & \exp\{-(2K/\varepsilon)\tau\}\eta(0) + (1/2K)\int (2K/\varepsilon)\exp\{-(2K/\varepsilon)(\tau - s)\} \times \\
& \times \{K^2(\psi_A - \psi_A^*) + b_{n1}h_{01}\psi_K - h_{01}h_{n1}\psi_A\}\, ds + \quad \text{(A.14)} \\
& + \tfrac{1}{2}\varepsilon\{(2K/\varepsilon)W(\tau) - \exp\{-(2K/\varepsilon)\tau)\}(4K^2/\varepsilon^2)\int \exp\{(2K/\varepsilon)r\}W(r)\,dr\}.
\end{aligned}$$

On the other hand, from (A.4b) it follows:

$$\begin{aligned}
\psi_K = {} & \exp\{-(K/\varepsilon)\tau\}\psi_K(0) - \\
& - (1/\mathrm{K})\int (\mathrm{K}/\varepsilon)\exp\{-(K/\varepsilon)(\tau - s)\}(b_{n1}/h_{01})\{\eta + K(\psi_A - \psi_A^*)\}ds. \quad \text{(A.15)}
\end{aligned}$$

Now we take the limit $(K/\varepsilon) \to \infty$ and notice that

$$\lim[(K/\varepsilon)\exp\{-(K/\varepsilon)(\tau - s)\}] \to \delta(\tau - s). \quad \text{(A.16)}$$

In this limit, (A.14) and (A.15) may be written as

$$\eta = (1/2K)\{-K^2(\psi_A - \psi_A^*) + b_{n1}h_{01}\psi_K - h_{01}h_{n1}\psi_A\} \quad \text{(A.17a)}$$

$$\psi_K = -(1/K)(b_{n1}/h_{01})\{\eta + K(\psi_A - \psi_A^*)\}. \quad \text{(A.17b)}$$

Solving for η and substituting in (A.5) we get

$$\psi_A = \psi_A(0) + \frac{1}{\varepsilon}\int \frac{-K^2(\psi_A - \psi_A^*) - b_{n1}^2(\psi_A - \psi_A^*) - h_{01}h_{n1}\psi_A}{2K + b_{n1}^2/K}\, ds + \int \dot{W}(r). \quad \text{(A.18)}$$

After changing back to time t, (A.18) is equivalent to the stochastic equation used in the text (Eq. (7)). We remark that in (A.18) we are left only with term $O(K^2/\varepsilon)$, i.e. about two orders of magnitude smaller than K/ε.

The crucial point of our approximation resides in assumption (A.16). The numerical value of K/ε is 10^3. We believe that this is a proper asymptotic limit and the numerical calculation in appendix B supports our belief. The next step would be to carry on the expansion of the function $(K/\varepsilon)\exp\{-(K/\varepsilon)(\tau - s)\}$ in powers of K/ε.

We remark that the technique here employed resembles and generalizes a way to demonstrate the diffusion limit for Brownian motion and also known as the Smoluchowski approximation (Schuss 1980 p. 132, compare the introduction of the variables x and y). Many other proofs of the Smoluchowski approximation are available including one based upon asymptotic expansion of the Fokker–Planck equation corresponding to the process. We have performed such an expansion and found the same result as in (A.18).

APPENDIX B

In this appendix we present numerical evidence about the approximation derived in appendix A. In Figs. 6 to 8 we present sample trajectories for the full model and for

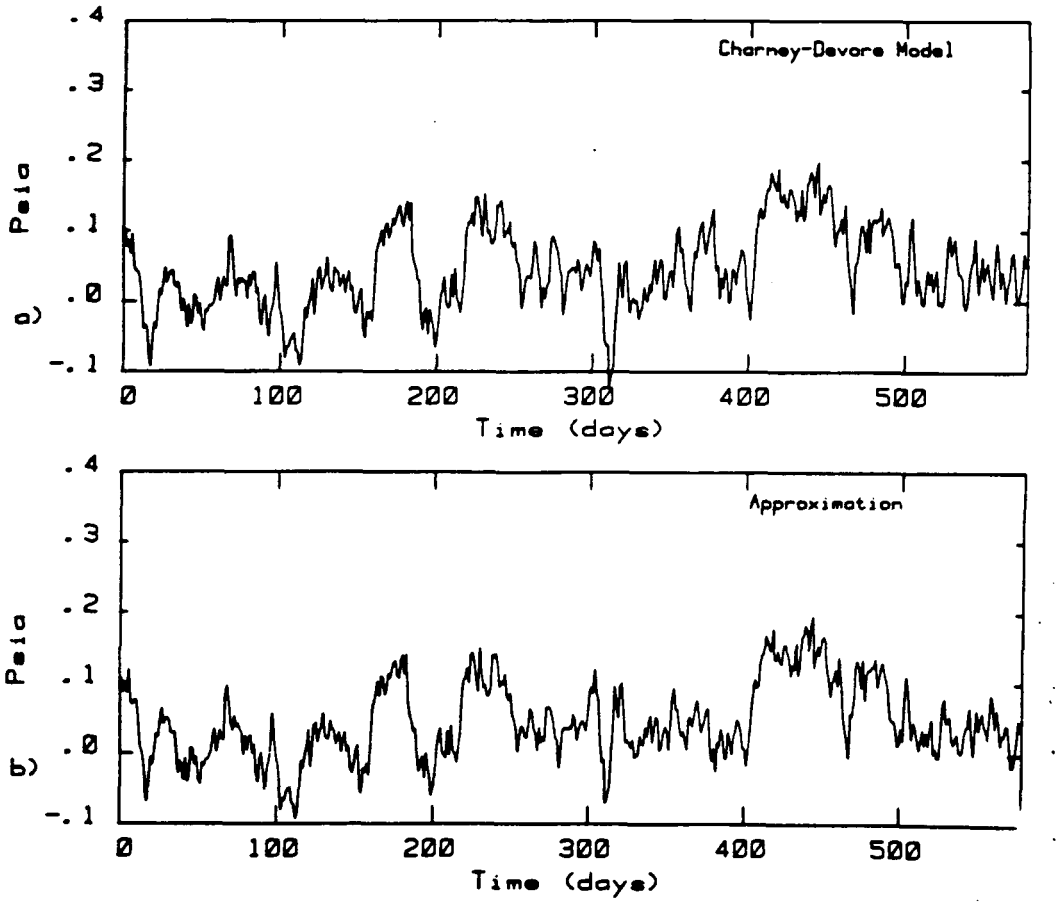

Figure 6. Sample solution of the CDV model with $\psi_A^* = 0{\cdot}10$, $h_{01}/H = 0{\cdot}05$, $K = 0{\cdot}01$ for (a) the full mode. (b) the approximation.

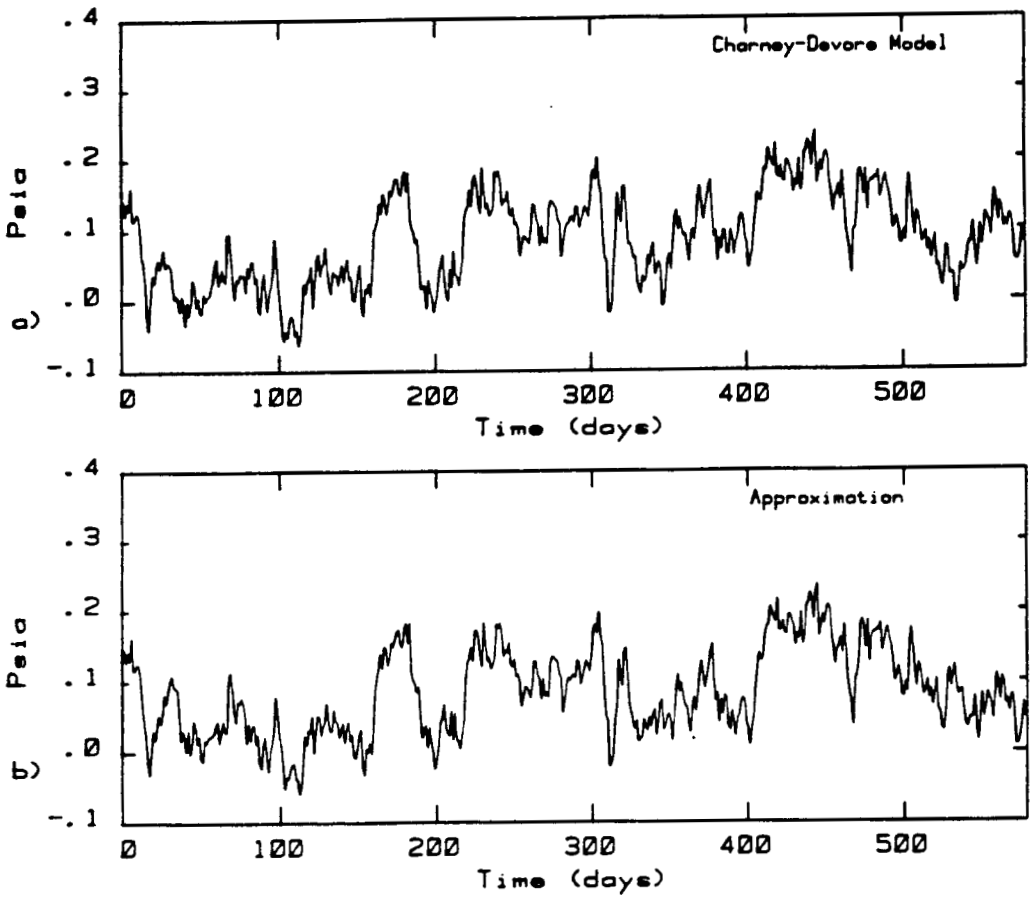

Figure 7. Sample solution, as Fig. 6 except $\psi_A^* = 0{\cdot}14$.

the approximation. We choose three cases. In the first (Fig. 6) the blocking solution is most probable. In the second (Fig. 7) the two equilibria are equally probable solutions and the zonal solution is most probable in the third case (Fig. 8). Statistically, we remark at the similarity between the two signals. For $\varepsilon = 5 \times 10^{-5}$, we have integrated the two models for a time equivalent to 5787 days counting the number of exits from one domain to the other one. The results are summarized in Table B1. We also calculate the residence time of the process. It is defined as the fraction of time spent by the trajectory in a cell of the phase-space. The cross-section along the ψ_A axis is presented in Fig. 9. From all this we may conclude that our approximation has a very good performance.

Finally we remark that our study is independent of the use of a perturbing process in only one component of the system. In fact, in the case of a perturbing process projected on all three equations, the technique is almost the same.

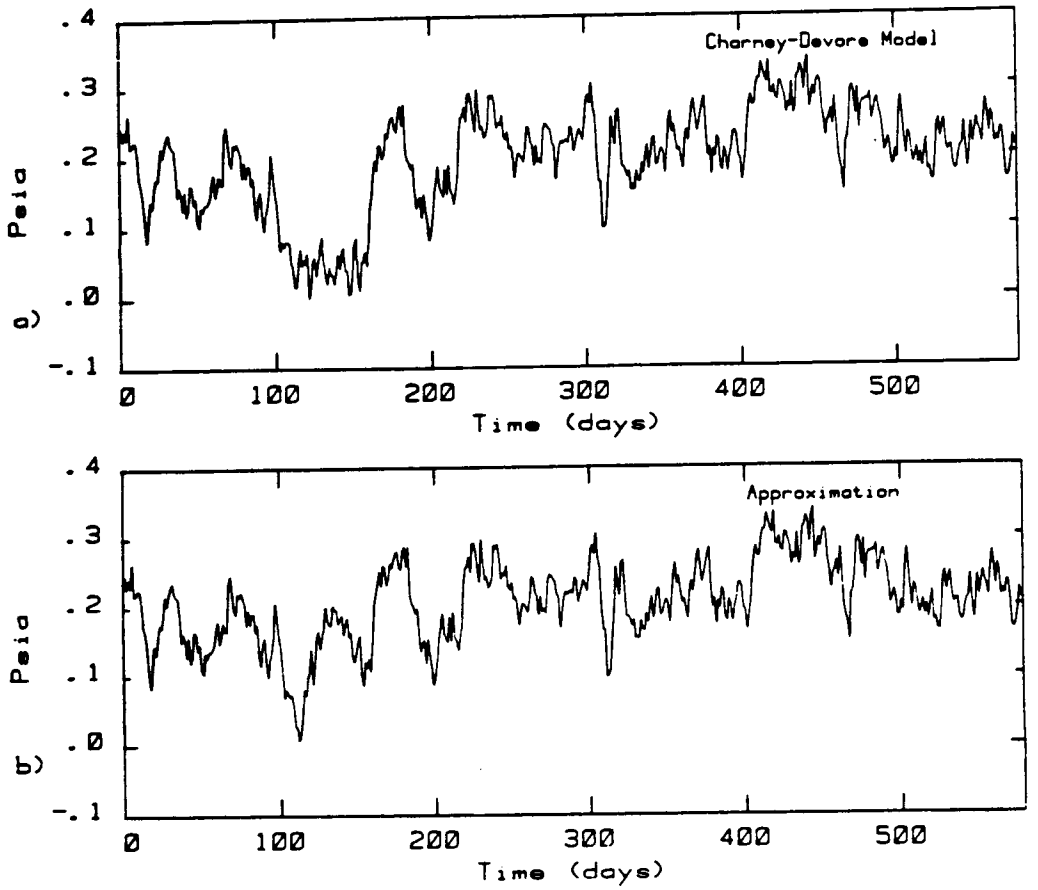

Figure 8. Sample sclution, as Fig. 6 except $\psi_A^* = 0{\cdot}24$.

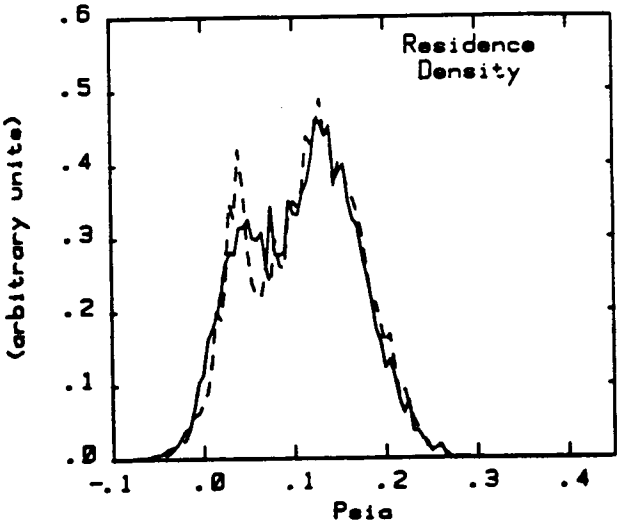

Figure 9. Residence time of the solution of the full model (solid line) and the approximation (dashed line) along the ψ_A axis. Here $h_{01}/H = 0{\cdot}05$ and $\psi_A^* = 0{\cdot}14$.

TABLE B1. STATISTICS ON THE EXIT TIMES (IN DAYS) OBTAINED BY INTEGRATING THE FULL MODEL AND THE APPROXIMATION FOR 5787 DAYS

	Number of exits	Average exit time	Standard deviation
Full model			
Zonal → Blocking	130	31·40	43·00
Blocking → Zonal	166	8·69	8·00
Approximation model			
Zonal → Blocking	122	34·70	45·60
Blocking → Zonal	133	10·30	10·44

$h_{01}/H = 0{\cdot}05$ and $\psi_A^* = 0{\cdot}14$

REFERENCES

Barnes, R. T. H., Hide, R., White, A. A. and Wilson, C. A. 1983 Atmospheric angular momentum fluctuations length-of-day changes and polar motion. *Proc. R. Soc. London A* **387**, 31–73.

Charney, J. G. 1974 Planetary fluid dynamics. *Dynamic Meteorology*, P. Morel (Ed.), D. Reidel, Dordrecht, Holland, pp. 99–351.

Charney, J. G. and DeVore, J. G. CDV 1979 Multiple flow equilibria in the atmosphere and blocking. *J. Atmos. Sci.*, **36**, 1205–1216.

Dole, R. M. and Gordon, N. D. 1983 Persistent anomalies of the extratropical Northern Hemisphere wintertime circulation: geographical distribution and regional persistance characteristics. Submitted to *Mon. Wea. Rev.*

Egger, J. E 1982 Stochastically driven large-scale circulation with multiple equilibria. *J. Atmos. Sci.*, **39**, 2606–2618.

Hansen, A. R. and Chen, T. C. 1982 A spectral energetics analysis of atmospheric blocking. *Mon. Wea. Rev.*, **110**, 1146–1165.

Hansen, A. R. and Sutera, A. 1983 A comparison of the spectral energy and enstrophy budgets of blocking compared to nonblocking periods. *Tellus* (August issue).

Källen, E. 1981 The nonlinear effects of orographic forcing and momentum forcing in a low order, barotropic model. *J. Atmos. Sci.*, **39**, 2150–2163.

1982 Bifurcation properties of quasi-geostrophic, barotropic models and their relation to atmospheric blocking. *Tellus*, **34**, 255–265.

Legras, B. and Ghil, M. 1983 Stationary, periodic and aperiodic solutions of atmospheric flows. Submitted to *J. de Mecanique*.

Lorenz, E. N. 1963 Deterministic nonperiodic flow. *J. Atmos. Sci.*, **20**, 130–141.

1982 Low order models of atmospheric circulations. *J. Meteorol. Soc., Japan*, Ser. II., **60**, 255–267.

Moritz, R. E. and Sutera, A. 1981 The predictability problem: effects of stochastic perturbation in multiequilibrium systems. *Adv. in Geophys.*, **23**, 345–383.

Schuss, Z. 1980 *Theory and Application of Stochastic Differential Equations*. Wiley and Sons, New York.

Sutera, A. 1980 Stochastic perturbation of a pure convection motion. *J. Atmos. Sci.*, **37**, 245–249.

1981 On stochastic perturbation and long term climate behaviour. *Quart. J. R. Met. Soc.*, **107**, 137–151.

Tellus (1985), *37A*, 41–55

The effect of finite-amplitude baroclinic waves on passive, low-level, atmospheric constituents, with applications to comma cloud evolution

By BARRY SALTZMAN, *Department of Geology and Geophysics, Yale University, New Haven, CT 06511, USA* and CHUNG-MUH TANG, *Universities Space Research Association, The American City Building, Suite 311, Columbia, MD 21044, USA*

(Manuscript received February 10; in final form June 13, 1984)

ABSTRACT

The redistribution of a low-level, passive constituent of the atmosphere under the influence of a growing baroclinic wave is examined by a series of analytical calculations based on a two-level, highly truncated model. It is shown that a constituent confined to the lower half of the atmosphere, and initially homogeneous in the horizontal, will tend to achieve maximum concentration in the low pressure/warm sector portion of the wave and minimum concentration in the high pressure/cold outbreak region with sharpest gradient between the maxima and minima roughly coinciding with the cold front. This distribution is further accentuated if an initial meridional gradient of the constituent exists.

If we assume, as a rough first approximation, that water vapor can be considered to be such a passive constituent, it is shown that the implied relative humidity field and cloud distribution will tend to evolve into the comma-type form commonly observed on satellite images of mid-latitude cyclone waves. Moreover, the solution is shown to replicate the complex flow regime associated with the comma formation, elucidating the dynamical rôles of vertical motion and advection in the cloud evolution.

1. Introduction

One consequence of the motions associated with growing baroclinic waves in middle latitudes is the redistribution of any passive atmospheric constituents (or tracers) that may be present at the time of inception of the waves. We shall investigate this redistribution with the two-level, β-channel, model of the evolution of finite-amplitude baroclinic waves developed previously (for a review see Saltzman and Tang (1982). The fundamental question we pose and discuss is the following: suppose a baroclinic wave forms in a field containing a constituent of horizontally uniform low-level mixing ratio ε, or of zonally uniform meridional gradient $(\partial\varepsilon/\partial y)$. To what finite-amplitude distribution will the constituent evolve under the influence of the motions generated by the baroclinic wave?

Secondly, we ask whether the above inferences are consistent with the observed distribution of water vapor and cloud in a baroclinic wave, the latter of which is often characterized by a distinct "comma" form. It will be assumed for this purpose that, as a first-order approximation, we can treat water vapor as such a passive constituent and that we can identify cloud coverage with some critical values of the relative humidity and vertical motion. Although it is clear that a full dynamical description of these cloud and moisture phenomena must depend on more detailed numerical models, it is also of value (at least from a pedagogical viewpoint) to deduce the essentials of the phenomena and its dynamics with the simplest model capable of analytical solution. In fact, one may argue that only from such "minimum" physical models do we gain a true "understanding" of complex phenomena. It is toward this end that this,

as well as our previous studies, have been directed. As we shall see, using our simple model it is indeed possible to account qualitatively for many of the main features of the comma cloud dynamics as revealed by detailed synoptic and satellite observations (Carlson, 1980).

2. The model

The symbols to be used in this study are the same as used previously (Saltzman and Tang, hereafter called S-T, 1972, 1975, 1982) and are defined in Appendix A. For present purposes we now add to this list the dependent variable ε, the mixing ratio for an arbitrary constituent of the atmosphere. The full set of basic equations governing the dependent variables ψ (stream function), χ (velocity potential), ω (individual pressure change), and ε are (S-T 1972),

$$\frac{\partial}{\partial t}\nabla^2\psi + \mathbf{V}_\psi \cdot \nabla(\nabla^2\psi) + \beta\frac{\partial\psi}{\partial x} - f\frac{\partial\omega}{\partial p} + N = 0, \tag{1}$$

$$f\frac{\partial^2\omega}{\partial p^2} + \frac{S}{f}\nabla^2\omega - \frac{\partial}{\partial p}[\mathbf{V}_\psi \cdot \nabla(\nabla^2\psi)] - \beta\frac{\partial^2\psi}{\partial p\,\partial x} + \nabla^2\left[\mathbf{V}_\psi \cdot \nabla\frac{\partial\psi}{\partial p}\right] - P = 0, \tag{2}$$

$$\nabla\cdot\mathbf{V}_\chi + \frac{\partial\omega}{\partial p} = 0, \tag{3}$$

$$\frac{\partial\varepsilon}{\partial t} + \mathbf{V}\cdot\nabla\varepsilon + \omega\frac{\partial\varepsilon}{\partial p} - \mathscr{S}_\varepsilon = 0, \tag{4}$$

where

$$N = \mathbf{V}_\chi\cdot\nabla(\nabla^2\psi) + \beta v_\chi + \omega\frac{\partial}{\partial p}\nabla^2\psi - \nabla^2\psi\frac{\partial\omega}{\partial p} + k\cdot\nabla\omega\frac{\partial\mathbf{V}_\psi}{\partial p},$$

$$P = \left\{\frac{\partial N}{\partial p} - \nabla^2\left[\mathbf{V}_\chi\cdot\nabla\frac{\partial\psi}{\partial p}\right]\right\},$$

$$S = \frac{R}{p}\left(\frac{RT}{c_p p} - \frac{\partial T}{\partial p}\right),$$

$\mathscr{S}_\varepsilon$ = source function for ε.

As in the previous studies we consider the two-layer system portrayed in Fig. 1, applied to a fundamental harmonic region of a β-plane having a meridional width D and zonal extent L (representing the wavelength of maximum baroclinic instability). For simplicity we assume that the constituent is confined only to the lower layer wherein its vertical mean concentration is given by ε_3 and the mean production $\mathscr{S}_\varepsilon$ is assumed to be zero. This would be the case, for example, if ε were constrained to the following vertical distribution,

$$\varepsilon(p) = \begin{cases} 2p_2^{-1}(p - p_2)\,\varepsilon_3 & (p > p_2) \\ 0 & (p \leqslant p_2) \end{cases}$$

corresponding physically to the behavior of a constituent whose initial source is near the surface and whose concentration always decreases markedly with height. The variable ε_3 is, therefore, a measure of the mass of the constituent in the complete vertical column (or, in the special case of water vapor, of the "precipitable water").

Next, we expand each of the dependent variables $\xi = (\psi, \chi, \omega, \varepsilon)$ into a zonal mean part $\bar{\xi}\,(y, t)$ and an eddy part $\xi'\,(x, y, t)$, as in S-T (1975), i.e.,

$$\xi = \bar{\xi} + \xi',$$

and further resolve each of these parts into an initial, basic, zonal field denoted by the superscript (0); a primary, quasigeostrophic, field denoted by the superscript (1) (Phillips, 1954); and a second order, non quasi-geostrophic, field denoted by the

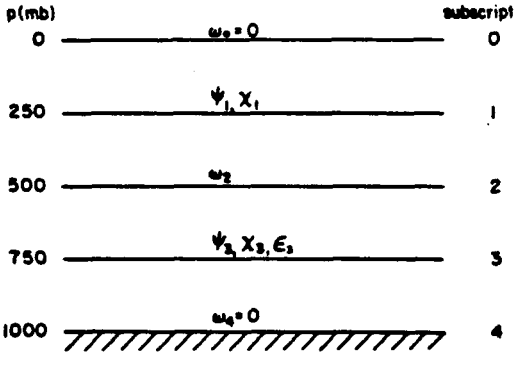

Fig. 1. Two-level model of baroclinic flow as represented by the dependent variables ψ, χ, ω and ε. The pressure levels are shown at the left and the corresponding subscript notation is shown at the right.

superscript (2); i.e.,

$$\tilde{\xi} = \tilde{\xi}^{(0)} + \tilde{\xi}^{(1)} + \tilde{\xi}^{(2)},$$

$$\xi' = \xi^{(1)} + \xi^{(2)},$$

so that, e.g., for $\xi = \varepsilon$, we have,

$$\varepsilon = \tilde{\varepsilon}^{(0)}(y) + \varepsilon^{(1)}(x, y, t) + \tilde{\varepsilon}^{(1)}(y, t) + \varepsilon^{(2)}(x, y, t). \tag{5}$$

We can then derive systems of equations for each of the above components, which will differ from those summarized in S-T (1982) only by the addition of equations for ε. The systems of equations take the following forms:

(I) Equations for the primary wave, $[\psi^{(1)}, \omega^{(1)}, \chi^{(1)}, \varepsilon^{(1)}]$:

$$\frac{\partial}{\partial t}\nabla^2\psi^{(1)}_{1,3} + \left(\tilde{u}^{(0)}\frac{\partial}{\partial x}\nabla^2\psi^{(1)}\right)_{1,3} + \beta\frac{\partial\psi^{(1)}_{1,3}}{\partial x} \mp \frac{f\omega^{(1)}_2}{p_2} = 0, \tag{6a}$$

$$\frac{S}{f}\nabla^2\omega^{(1)}_2 - \frac{2f}{p_2^2}\omega^{(1)}_2 + \frac{2\beta}{p_2}\frac{\partial\psi^{(1)}_T}{\partial x} + \frac{4}{p_2}\tilde{u}^{(0)}_T\frac{\partial}{\partial x}\nabla^2\psi^{(1)}_2 = 0, \tag{6b}$$

$$\nabla^2\chi^{(1)}_{1,3} = \mp\frac{\omega^{(1)}_2}{p_2}, \tag{6c}$$

$$\frac{\partial}{\partial t}\varepsilon^{(1)}_3 + \tilde{u}^{(0)}_3\frac{\partial\varepsilon^{(1)}_3}{\partial x} = -\frac{\partial\psi^{(1)}_3}{\partial x}\frac{\partial\tilde{\varepsilon}^{(0)}_3}{\partial y} - \tilde{\varepsilon}^{(0)}_3\frac{\omega^{(1)}_2}{p_2}. \tag{6d}$$

(II) Equations for the forced zonal state $[\tilde{\psi}^{(1)}, \tilde{\omega}^{(1)}, \tilde{\chi}^{(1)}, \tilde{\varepsilon}^{(1)}]$:

$$\frac{S}{f}\frac{\partial^2\tilde{\omega}^{(1)}_2}{\partial y_2} - \frac{2f}{p_2}\tilde{\omega}^{(1)}_2 = A(\psi^{(1)}), \tag{7a}$$

$$\frac{\partial}{\partial t}\left(\frac{\partial^2\tilde{\psi}^{(1)}}{\partial y^2}\right)_{1,3} = -[\mathbf{V}^{(1)}_\bullet\cdot\nabla(\nabla^2\psi^{(1)})]_{1,3} \pm \frac{f}{p_2}\tilde{\omega}^{(1)}_2, \tag{7b}$$

$$\frac{\partial^2\tilde{\chi}^{(1)}_{1,3}}{\partial y^2} = \mp\frac{\tilde{\omega}^{(1)}_2}{p_2}, \tag{7c}$$

$$\frac{\partial\tilde{\varepsilon}^{(1)}_3}{\partial t} = -\frac{\partial}{\partial y}(\overline{v^{(1)}_\bullet\varepsilon^{(1)}})_3 - \left(\tilde{v}^{(1)}_x\frac{\partial\tilde{\varepsilon}^{(0)}}{\partial y}\right)_3 - \tilde{\varepsilon}^{(0)}_3\frac{\tilde{\omega}^{(1)}_2}{p_2}. \tag{7d}$$

(III) Equations for the secondary wave fields, $[\psi^{(2)}, \omega^{(2)}, \varepsilon^{(2)}]$:

$$\frac{\partial}{\partial t}\nabla^2\psi^{(2)}_{1,3} + \left(\tilde{u}^{(0)}\frac{\partial}{\partial x}\nabla^2\psi^{(2)}\right)_{1,3} + \beta\frac{\partial\psi^{(2)}_{1,3}}{\partial x} \mp \frac{f}{p_2}\omega^{(2)}_2 = B(\psi^{(1)}, \omega^{(1)}, \chi^{(1)}; \tilde{\psi}^{(1)}, \tilde{\omega}^{(1)}, \tilde{\chi}^{(1)}), \tag{8a}$$

$$S\nabla^2\omega^{(2)}_2 - \frac{2f^2}{p_2^2}\omega^{(2)}_2 = C(\psi^{(1)}, \psi^{(2)}, \tilde{\psi}^{(1)}), \tag{8b}$$

$$\frac{\partial}{\partial t}\varepsilon^{(2)}_3 + \left(\tilde{u}^{(0)}\frac{\partial\varepsilon^{(2)}}{\partial x}\right)_3 = -\Bigg[v^{(1)}_x\frac{\partial\tilde{\varepsilon}^{(0)}}{\partial y} + \left(u^{(1)}_x\frac{\partial\varepsilon^{(1)}}{\partial x}\right)' + \left(v^{(1)}_x\frac{\partial\varepsilon^{(1)}}{\partial y}\right)' - \left(\varepsilon^{(1)}\frac{\partial\omega^{(1)}}{\partial p}\right)' + \tilde{u}^{(1)}_\bullet\frac{\partial\varepsilon^{(1)}}{\partial x} + v^{(1)}_\bullet\frac{\partial\tilde{\varepsilon}^{(1)}}{\partial y} + v^{(1)}_x\frac{\partial\tilde{\varepsilon}^{(1)}}{\partial y} - \tilde{\varepsilon}^{(1)}\frac{\partial\omega^{(1)}}{\partial p} + v^{(2)}_\bullet\frac{\partial\tilde{\varepsilon}^{(0)}}{\partial y} + v^{(2)}_x\frac{\partial\tilde{\varepsilon}^{(0)}}{\partial y} - \tilde{\varepsilon}^{(0)}\frac{\partial\omega^{(2)}}{\partial p}\Bigg]_3. \tag{8c}$$

Where double signs appear in these equations, the upper sign refers to level 1 (250 mb) and the lower sign to level 3 (750 mb); S is assumed to be a horizontally uniform value of the static stability representative of conditions prevailing near the wave center (i.e., near $y = \frac{1}{2}D$, and A, B, and C represent non-homogeneous forcing due to the lower order fields, the expressions for which are given in S-T (1972, 1975) and are restated in Appendix B in a unified notation. In the present calculations, we approximate C ($=F_s + F_a$, S-T 1975) by including only the linear terms in F_a. We also neglect $\tilde{\omega}^{(2)}_2$, which is relatively small over the time span of wave evolution we shall consider (i.e., 5.6 days).

Note that our model still contains many of the deficiencies that were inherent in the previous studies, e.g. (i) the two-level approximation eliminates the possibility for treating the true vertical structure of developing cyclone waves in complete detail, (ii) the latitudinal boundaries are "soft" in

the sense that although they are closed for geostrophic (non-divergent) flow, they are open for non-geostrophic (divergent) flow (cf., Moen, 1974; Paegle and MacDonald, 1974), (iii) in treating a single primary wave we neglect barotropic wave-wave, as well as wave-mean flow, interactions and, (iv) no feedbacks to the basic zonal thermal state ($\bar{\psi}^{(0)}$, $\bar{S}^{(0)}$) are included as they were in S-T (1982), so that the primary wave grows exponentially without saturating (i.e., without reaching the occlusion stage) and we can only consider the early stages of wave growth during which the finite-amplitude wave attains its fundamental structure. One consequence of this latter deficiency is that, along with the unabated growth of the amplitude of the motion field, the amplitude of the mixing ratio field ε will also tend to grow beyond realistic bounds. Potentially, this could even lead to nega-

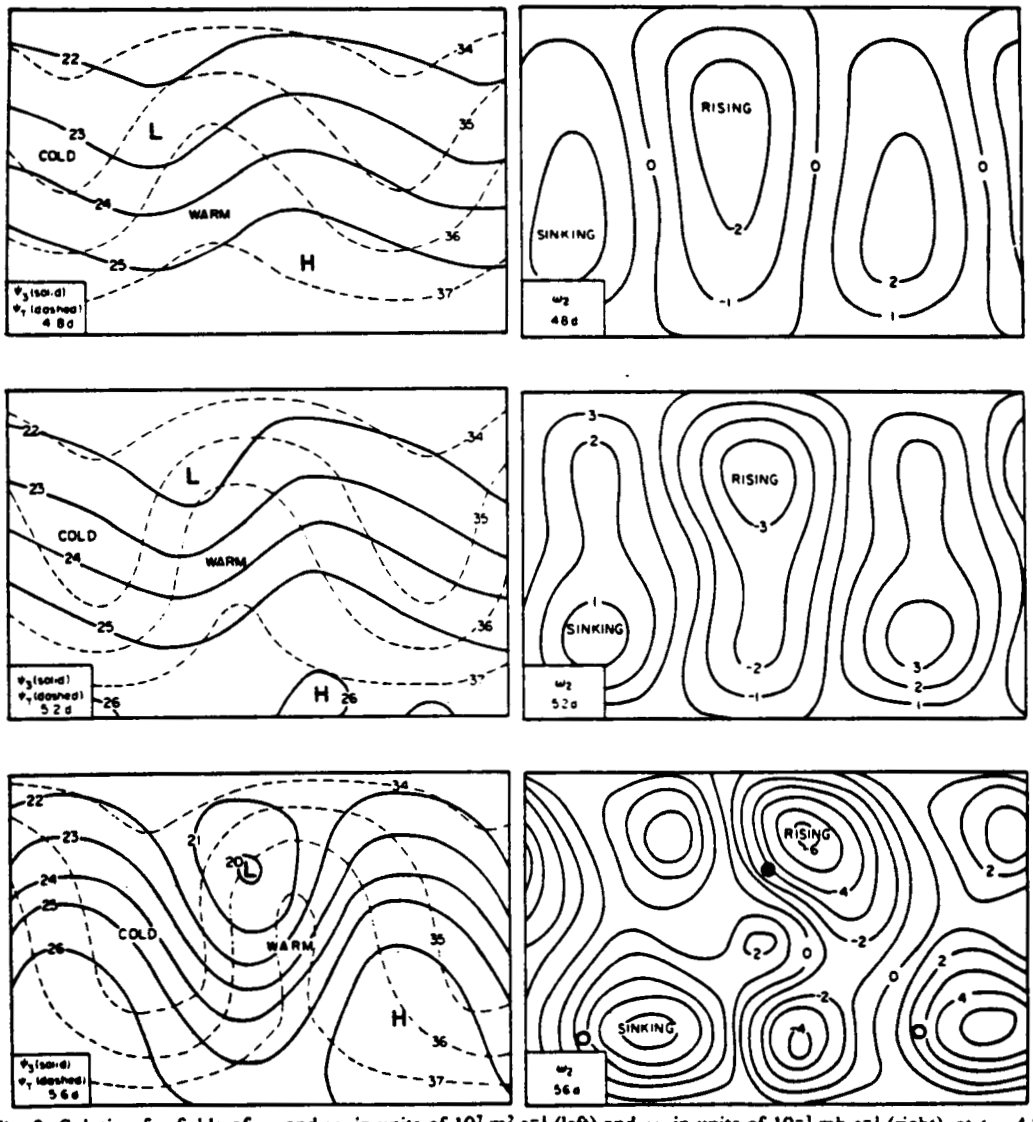

Fig. 2. Solution for fields of ψ_2 and ψ_T in units of 10^7 m^2 s^{-1} (left) and ω_2 in units of 10^{-3} mb s^{-1} (right), at $t = 4.8$, 5.2, and 5.6 days. For $t = 5.6$ days, full and open dots denote closed centers of 750 mb lows and highs, respectively (also shown in Figs. 3, 5 and 6).

tive values of ε_3. For all of these reasons, our results can only be expected to give a qualitative understanding of the rôle of baroclinic, non-geostrophic processes in the early evolution of the wave and its associated constituent concentrations.

3. Solutions for the fields of passive constituents

The analytical solution of (6a, b, c) (7a, b, c) and (8a, b) for the evolution of a baroclinic wave are given in S-T (1972, 1975) and will not be repeated here. In Fig. 2 we plot the solution, corresponding to the same basic state and initial conditions given in S-T (1972), at roughly 10 h intervals for three points in time after the introduction of the initial perturbation: $t = 4.8$, 5.2, and 5.6 days, the last of which (5.6 days) was discussed previously in S-T (1972, Fig. 11a, b; 1975, Fig. 4). According to the solution, the wave progresses eastward at the phase speed $c_r = 16$ m s^{-1}. The analytical solutions of (6d), (7d), and (8c), governing the separate components of ε_3, are given in Appendix C.

Suppose we consider, as Case I, that a non-interacting (passive) constituent, confined to the lower layer, is uniformly distributed horizontally at the time of inception of the wave at $t = 0$ and has an arbitrary mixing ratio, $\tilde{\varepsilon}_3^{(0)} = \bar{\varepsilon}_3^{(0)} = 2 \times 10^{-3}$. In Fig. 3 we show the composite distribution of ε_3 (x, y, t) at $t = 4.8$, 5.2, and 5.6 days obtained by summing the solutions of (6d, 7d, and 8c) given in Appendix C, in accordance with (5).

In Fig. 4 we show the separate components $\varepsilon_3^{(1)}$, $\tilde{\varepsilon}_3^{(1)}$, and $\varepsilon_3^{(2)}$ that comprise the complete field shown in Fig. 3 for $t = 5.6$ days. We can see that the first-order eddy solution $\varepsilon_3^{(1)}$ alone would give a symmetrical field related to the field of divergence (or, equivalently, of $\omega^{(1)}$, S-T 1972) generated by the first order baroclinic wave. However, the second-order, non-geostrophic processes that become large as the wave evolves lead to a more asymmetric pattern in which the maximum and minimum concentrations are displaced to coincide more closely to the low and high pressure regions, respectively, with a relatively strong gradient between them roughly in the region of the thermal front.

If we consider, as Case II, an initial state in which the constituent is not uniformly distributed, but is characterized by a constant equatorward

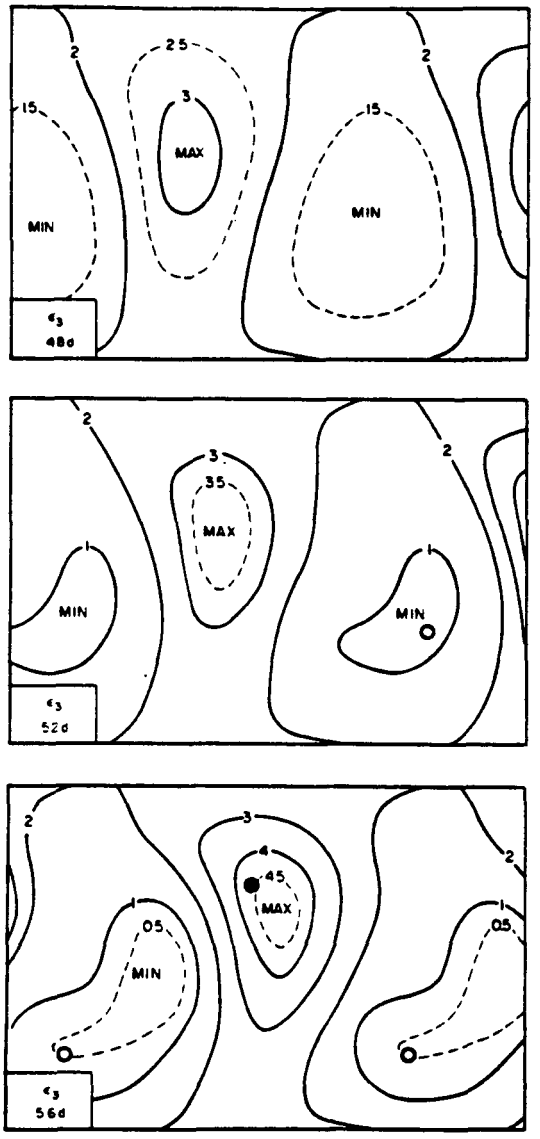

Fig. 3. Solution for field of ε_3 in units of 10^{-3}, for Case I [$\bar{\varepsilon}_3^{(0)} = 2 \times 10^{-3}$ and $\partial\bar{\varepsilon}^{(0)}/\partial y = 0$] at $t = 4.8$, 5.2, and 5.6 days.

gradient, $-\partial\bar{\varepsilon}_3^{(0)}/\partial y = +3 \times 10^{-10}$ m^{-1}, the first-order solution will contain a contribution from meridional advection as well as from divergence. In this case, the sequential solution for $t = 4.8$, 5.2, and 5.6 days is of the form shown in Fig. 5. As noted in Section 2, one obvious deficiency of the solution shown in Fig. 5 is that under the influence of the unabated exponential growth of the baro-

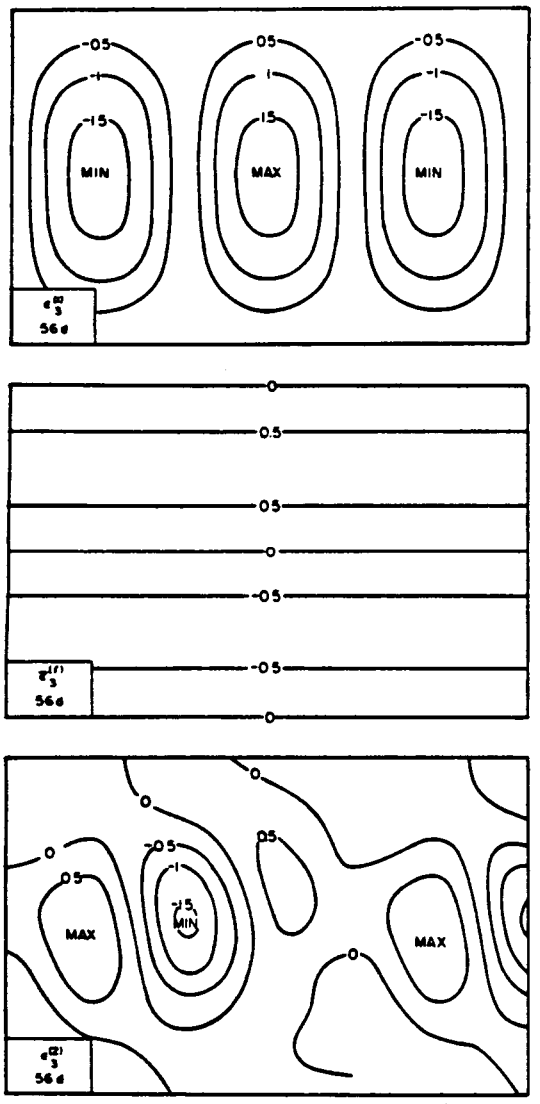

Fig. 4. Component solutions, $\varepsilon_3^{(1)}$, $\tilde{\varepsilon}_3^{(1)}$, and $\varepsilon_3^{(2)}$, at 5.6 days, for the complete Case I solution shown in Fig. 3.

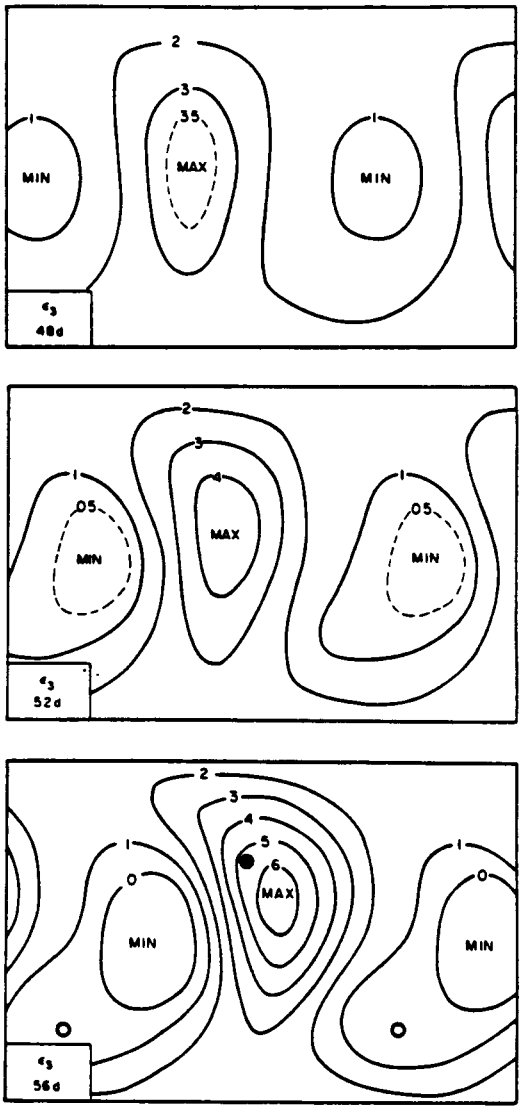

Fig. 5. Solution for field of ε_3 in units of 10^{-3}, for Case II [$\tilde{\varepsilon}_3^{(0)} = 2 \times 10^{-3}$ and $\partial\tilde{\varepsilon}_3^{(0)}/\partial y = -3 \times 10^{-10}$ m^{-1}] at $t =$ 4.8, 5.2, and 5.6 days.

clinic wave, the amplitude of ε also grows at an unrealistic rate so that, depending on the initial mean value of ε, negative values may even be generated. This occurred at $t = 5.6$ days. Although this is physically unacceptable, it is likely that if proper account were taken of wave occlusion processes (e.g., S-T, 1982) this unrealistic feature would be removed without altering the general nature of this solution. Aside from this increase in amplitude, this solution for $\partial\tilde{\varepsilon}^{(0)}/\partial y \neq 0$ is similar in form and phase to the solution shown in Fig. 3 for $\partial\tilde{\varepsilon}^{(0)}/\partial y = 0$.

4. Inferences concerning water vapor and cloud distribution in baroclinic waves

As is well-known, water vapor is not a "passive" constituent of the atmosphere; condensation

and evaporation are continually taking place, and the condensation process entails release of latent heat that can modify the temperature and motion fields of the waves. Nonetheless, we shall assume that these processes are small enough relative to the advective processes that we can neglect them as a first approximation and explore the implications of our solutions for the distributions of water vapor and cloud in baroclinic waves. Thus, if we let $\varepsilon = \varepsilon_v$ (water vapor mixing ratio) we see from Fig. 5 that under the influence of a growing baroclinic wave, an initial "climatological" basic state characterized by $\bar{\varepsilon}_{v3}^{(0)}(\frac{1}{2}D) = 2 \times 10^{-3}$ and $\partial\bar{\varepsilon}_{v3}^{(0)}/\partial y = -3 \times 10^{-10}$ m^{-1} would become eddied into a high concentration pool in the low pressure region and low concentration pool in the high pressure region separated by a strong east-west gradient in the frontal region. Although, for the reasons given previously, we find unrealistic values of the maxima and minima at $t = 5.6$ days, we assume the distributions are qualitatively correct, and can even imagine that the neglected evaporation, condensation, and precipitation processes would at least partially offset these unrealistic maxima and minima. That is, to some degree we can identify supersaturation with the transformation of vapor to liquid water.

With the above limitation in mind, we next obtain from the mixing ratio distribution and the thermal field of the wave (extrapolated to level 3) a qualitative estimate of the field of relative humidity r, defined by

$$r(x, y) = \frac{\varepsilon_{v3}(x, y)}{\varepsilon_{vsat}(T_3(x, y))}, \qquad (9)$$

where $T_3 = T_2 + 18K$. For this purpose, we simply set $\varepsilon_v = 0$ where $\varepsilon_v < 0$ and allow r to achieve highly supersaturated values (>100%) where ε_v is large. The patterns of r obtained for $t = 4.8$, 5.2, and 5.6 days are shown in Fig. 6.

If as in many dynamical models, we assume that cloud amount is proportional to r (e.g., Smagorinsky, 1960; Vallis, 1982); we can see that the solution qualitatively portrays the evolution of the "comma-cloud" structure commonly observed in satellite images of developing mid-latitude cyclones. Further, if as in some other models (Lewis, 1957) we relate cloud coverage to some arbitrary critical values of r *and also* vertical motion ($\sim -\omega_2$), we can obtain cloud distributions that may exhibit even more realistic evolutions to

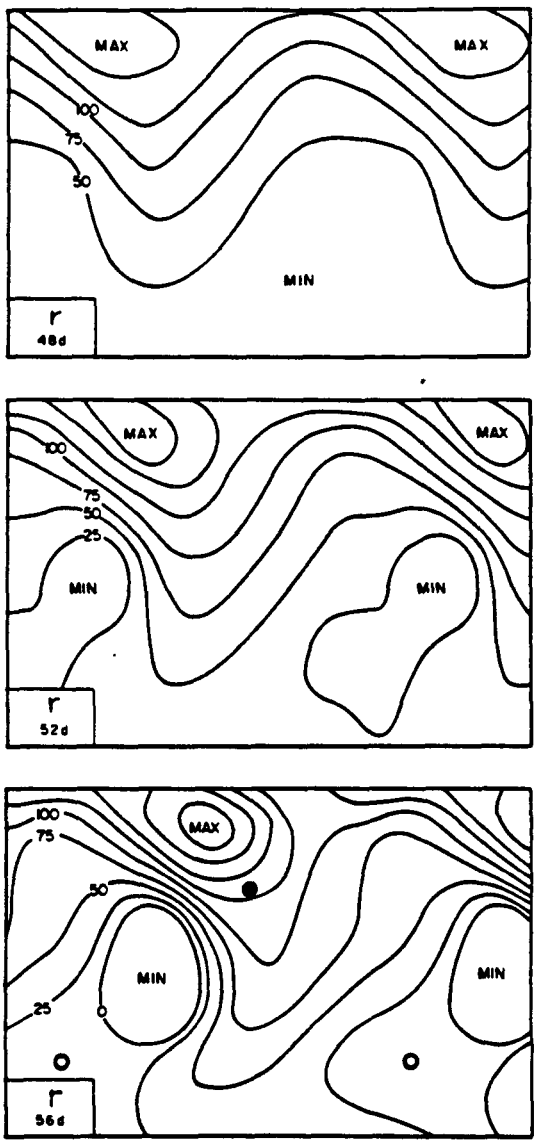

Fig. 6. Field of relative humidity r, in units of %, corresponding to ε_3 fields for Case II shown in Fig. 5, for $t = 4.8$, 5.2, and 5.6 days.

the comma-shape. For example, in Fig. 7 we show the cloud coverage obtained by applying the conditions $r > 0.60$ and $\omega < 0$ to the results shown in Figs. 2 and 6. This sequence can be seen to compare favorably with the schematic cloud evolution sequence in a cyclone wave given by Anderson and Veltishchev (1973, Fig. III.5.5), and with Fig. 8 showing a sequence of GOES infrared

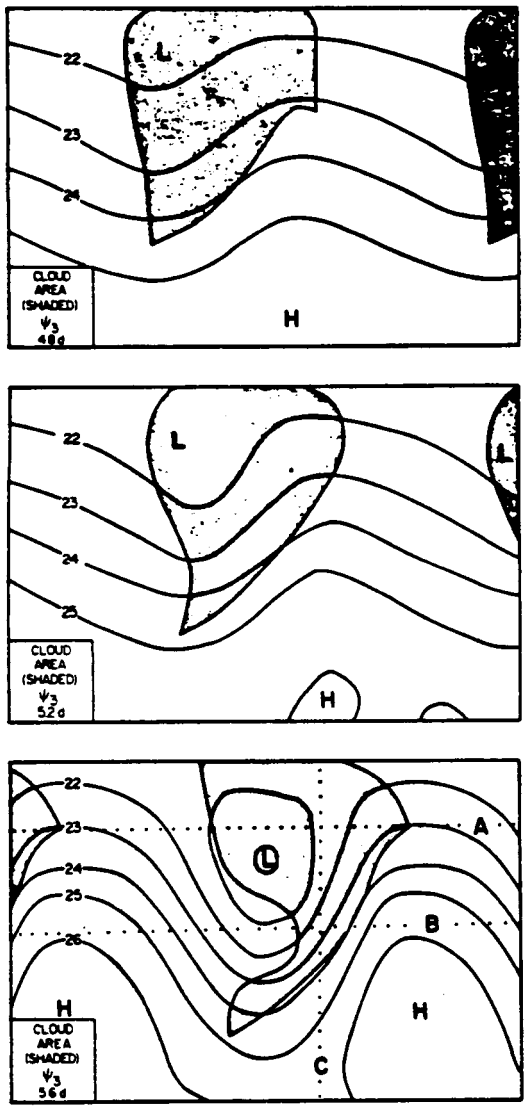

Fig. 7. Cloud areas deduced for Case II from the condition ($r > 0.60$, $\omega < 0$) applied to Fig. 6, for $t = 4.8$, 5.2, and 5.6 days. Dotted lines labeled A, B, and C, for $t = 5.6$ days, are those along which the vertical cross sections shown in Figs. 10, 11, and 12 are drawn.

images spaced roughly 10 h apart (as in our solutions) for a cyclone-wave development over the eastern United States. In the last figure of this GOES sequence (Fig. 8d), the storm is beyond the occlusion stage and is strongly under the influence of non-adiabatic processes over the ocean. The first three images can be roughly compared to the results shown in Fig. 7 for $t = 4.8$, 5.2, and 5.6 days. We note the important rôles played in the comma development at $t = 5.6$ days by the emergence of a strong subsidence region and associated low-level divergence in the region just equatorward of the low-pressure center which generates the dry clear zone (see ω_2, Fig. 2, 5.6 days) and by the horizontal advective processes that sweep water vapor poleward around the low-pressure center at low levels.

An excellent discussion of the synoptic features associated with comma-cloud development has been given by Carlson (1980). His analysis suggests that two main cloud-producing streams of air relative to the moving storm system are involved in the generation of the comma cloud. One is characterized as a potentially-warm "conveyor belt" bringing moist air from the low latitudes, in which middle- and high-level cloud form in the "tail" and eastern portion of the comma; the other is a potentially-cooler low-level "conveyor belt" from the east in which the stratus shield constituting the western portion of the comma forms. In spite of the limitations of our two-level model, these flow features, summarized in Carlson's Figs. 9 and 10 (1980), seem to be well replicated by our solution. The upper and lower level air streams, *relative to our eastward moving baroclinic wave* system containing the qualitative comma cloud, are shown in Fig. 9 (left) along with the satellite infrared cloud image shown in Fig. 8c (right). Also shown in Fig. 9 (left) is the branching of the flow at level 3 (dashed streamline) near the tip of the comma tail, as described by Carlson (1980). In Figs. 10, 11, and 12 we show the vertical cross sections of the solution flow along the three slices labeled A, B, and C in Figs. 7 and 9, including a representation of the variations of temperature and moisture along section C. The low level "cold conveyor" is depicted in section A (Fig. 10); the cold front and adjacent dry-descending and warm-moist-ascending poleward air streams are depicted in section B (Fig. 11); the upper level "warm conveyor" is depicted in the north-south section C (Fig. 12). Although these features emerge naturally in detailed numerical forecasting solutions, we believe the present, two-layer, highly-truncated model is the "minimum" low-order system capable of demonstrating that these complex features follow, qualitatively at least, from the basic laws governing atmospheric behavior.

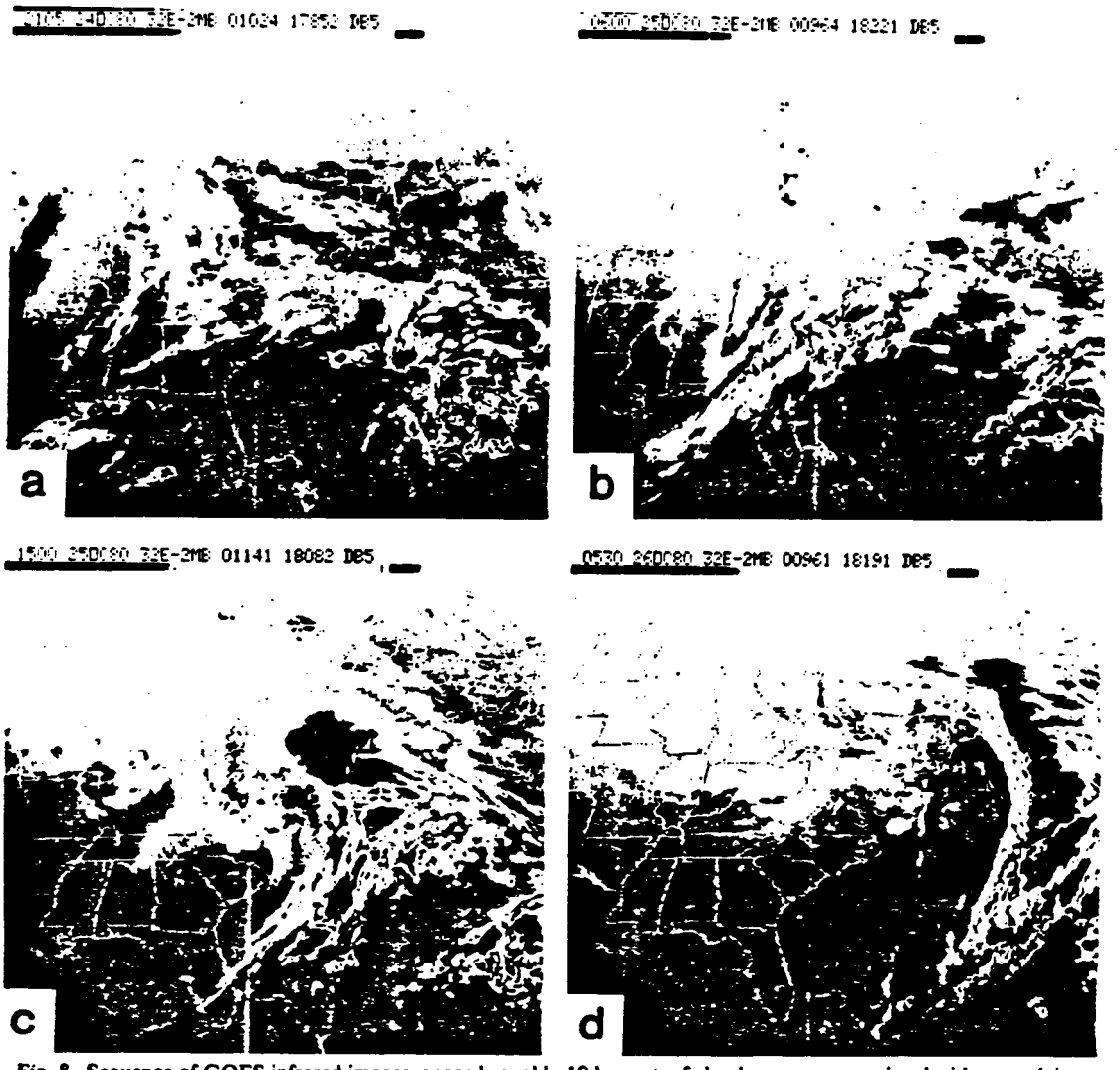

Fig. 8. Sequence of GOES infrared images, spaced roughly 10 h apart, of cloud coverage associated with an evolving cyclone-wave over the eastern United States, (a) 2105 GMT, 24 OCT, (b) 0600 GMT, 25 OCT, (c) 1500 GMT, 25 OCT, (d) 0530 GMT, 26 OCT.

5. Concluding remarks

As we have noted, the present study is meant to complement the more detailed numerical modeling efforts aimed at accounting for and predicting large-scale weather phenomena. It is at least of pedagogical value to be able to show that major observational features can be explained in terms of highly idealized, simple, models that contain a minimum of essential physical ingredients.

In the present case, we have (1) deduced the evolving distribution of an arbitrary low-level passive tracer or pollutant under the influence of a growing baroclinic wave, and (2) applied this solution to show that a two-level, adiabatic, baroclinic model including non-geostrophic, finite-amplitude, passive-advective effects is apparently sufficient to yield a qualitative solution for the mean features and underlying dynamics of comma cloud formation. It is clearly possible and potentially instructive to improve upon our simple model by many further additions short of a full numerical

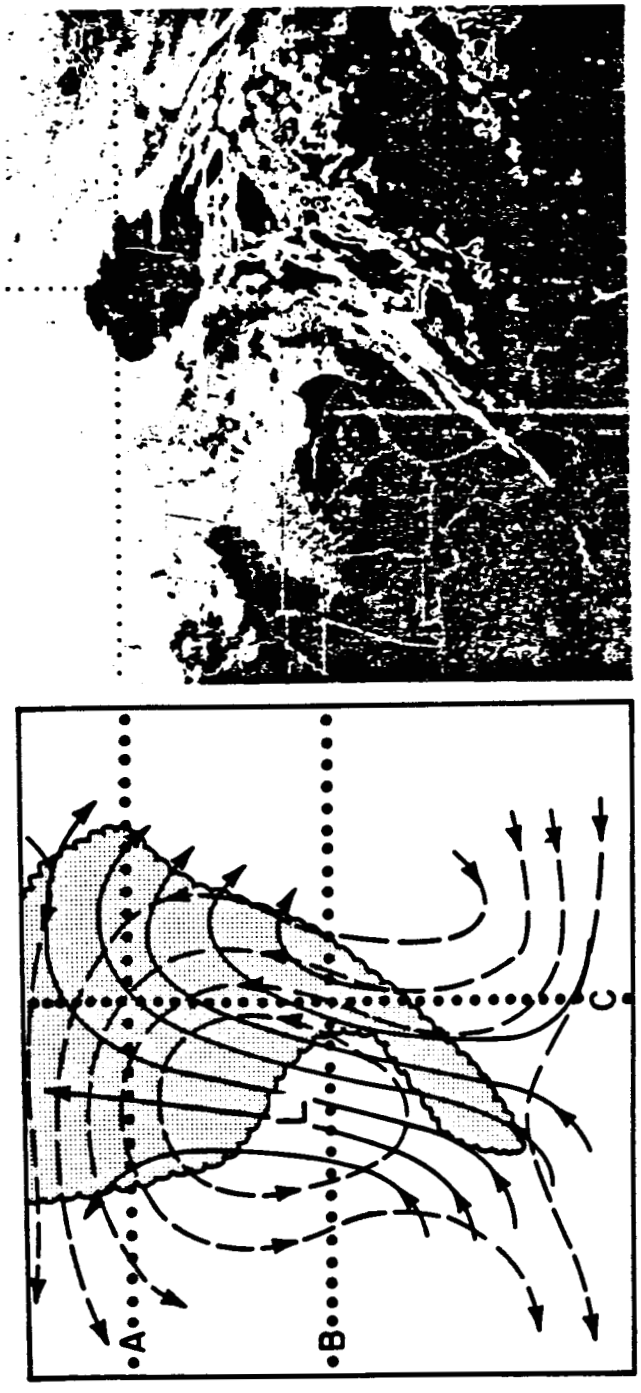

Fig. 9. Left: The solution at 5.6 days showing the level 2 upper streamlines (solid lines) and level 3 lower streamlines (dashed lines), both relative to the *moving* wave, in the vicinity of the comma cloud (scalloped area). Air is rising throughout the comma cloud area. Right: Comparable GOES infrared image of a comma cloud as shown in Fig. 8c. Dotted lines indicate section cross sections shown in Figs. 10, 11, and 12.

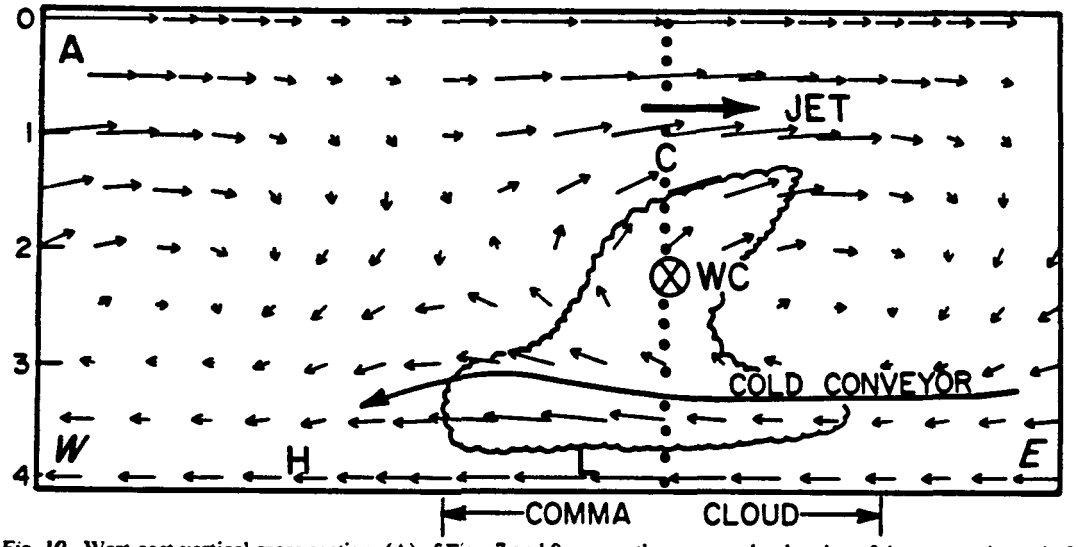

Fig. 10. West-east vertical cross section, (A) of Figs. 7 and 9, across the comma cloud region of the wave poleward of the surface low pressure center, showing the solution vector air motions relative to the eastward moving wave. Note the low-level "cold conveyor", upper-level "jet stream", and "warm conveyor" streamflow (labeled "WC") into the plane along cross section C of Fig. 7. The locations of the surface low and high are indicated by L and H. The comma cloud region is labeled on the abscissa, and a schematic conceptualization of the probable cloud cross section is shown by the scalloped region.

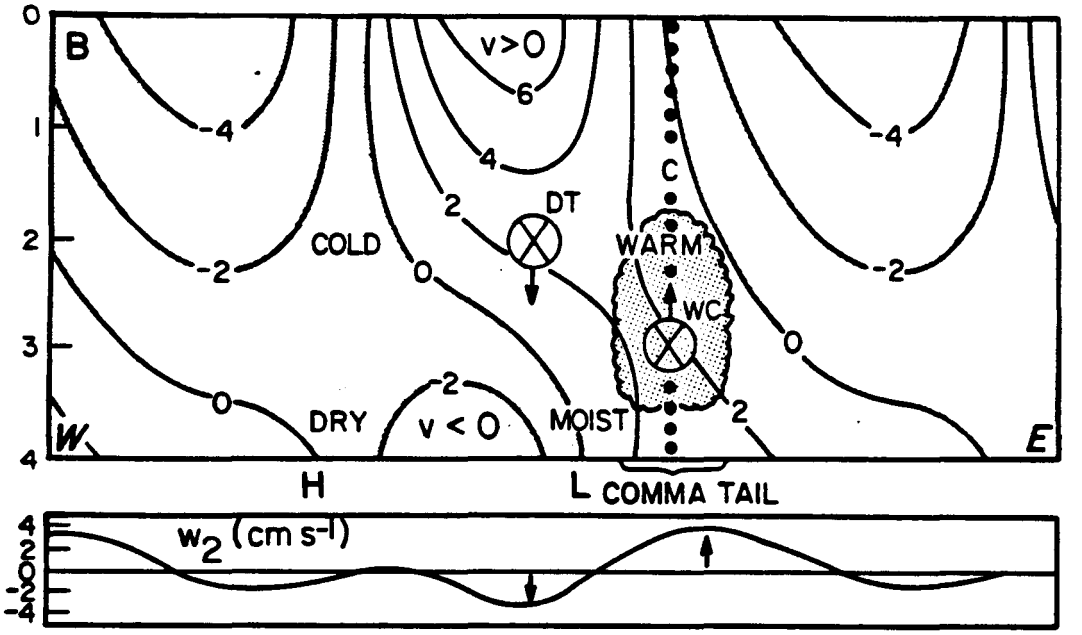

Fig. 11. West-east vertical cross section, (B) of Fig. 9, across the middle latitude of the wave, showing the meridional component of the wind v (in units of 10 m sec^{-1}), the maxima of temperature T and relative humidity r. Note the *high-level* northward-moving "dry tongue", DT, and adjacent *low-level* northward-moving moist warm "conveyor", WC, streamflow paralleling the frontal region. The distribution of vertical motion ω at level 2 is shown in the lower panel.

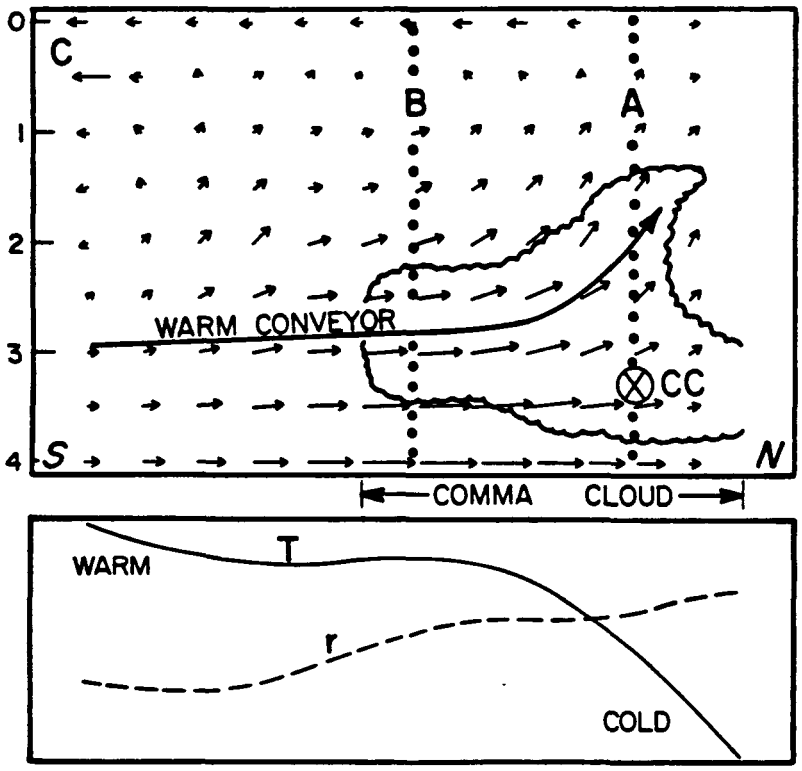

Fig. 12. South-north vertical cross section (C) of Fig. 7, showing the "warm conveyor" flow overriding the east-west "cold conveyor" flow into the plane of the cross section marked by CC. The distributions of T and r along this section are shown in the lower panel. The comma cloud extent is indicated on the abscissa, and a hypothetical cloud cross section is shown by the scalloped region.

treatment. These include additional levels in the vertical, wave-wave and wave-meanflow interactions, wave saturating feedbacks with the basic state, constituent fluxes to and from the upper half of the atmosphere, and the replacement of our semi-empirical model for cloud by simple representations of cloud and precipitation physics including the non-adiabatic effects of latent heat release.

6. Acknowledgments

This study was supported by the National Aeronautics and Space Administration under contract NAS 8-34903 at Yale University and NAS 8-34010 at the Universities Space Research Association.

7. Appendix A

List of symbols

x	distance eastward
y	distance northward
z	height above sea level
p	pressure
t	time
u	eastward wind speed
v	northward wind speed
ω	dp/dt
g	acceleration of gravity
c_p	specific heat at constant pressure
R	gas constant for air
f	Coriolis parameter, $2\Omega \sin \phi$
Ω	angular speed of earth's rotation
ϕ	latitude
β	df/dy

Φ geopotential, gz
ψ geostrophic streamfunction, $f^{-1}\Phi$
χ velocity potential
T temperature, $-pfR^{-1}\,\partial\psi/\partial p$
α specific volume
θ potential temperature, $R^{-1}p_4^{\kappa}p^{1-\kappa}\alpha$
S static stability, $-\alpha\partial \ln \theta/\partial p$
κ R/c_p
i unit vector eastward
j unit vector northward
k unit vector upward
∇ $i\,\partial/\partial x + j\,\partial/\partial y$
V vector horizontal wind, $ui + vj = V_\psi + V_\chi$
V_ψ non-divergent (geostrophic) wind component, $k \times \nabla\psi = u_\psi i + v_\psi j$ $(u_\psi = -\partial\psi/\partial y,\ v_\psi = \partial\psi/\partial x)$
V_χ irrotational wind component, $\nabla\chi = u_\chi i + v_\chi j$ $(u_\chi = \partial\chi/\partial x, v_\chi = \partial\chi/\partial y)$
ζ vertical component of vorticity, $k\cdot\nabla\times V = \nabla^2\psi$
δ horizontal divergence, $\nabla\cdot V = \nabla^2\chi$

and, with reference to Fig. 1, we also define

$$\psi_2 = \tfrac{1}{2}(\psi_1 + \psi_3).$$

$$\psi_T = \tfrac{1}{2}(\psi_1 - \psi_3).$$

$$T = T_2 = \frac{2f}{R}\psi_T.$$

$$u_T = -\frac{\partial\psi_T}{\partial y},$$

$$v_T = \frac{\partial\psi_T}{\partial x}.$$

8. Appendix B

Forcing terms in eqs. (7a), (8a) and (8b)

$$A = -\frac{4}{p_2}\left[\overline{V_T^{(1)}\cdot\nabla(\nabla^2\psi_2^{(1)})} - k\cdot\left(\overline{\frac{\partial V_{\psi 2}^{(1)}}{\partial x}\times\frac{\partial V_T^{(1)}}{\partial x}} + \overline{\frac{\partial V_{\psi 2}^{(1)}}{\partial y}\times\frac{\partial V_T^{(1)}}{\partial y}}\right)\right],$$

$$B = -\left\{\left[V_\psi^{(1)}\cdot\nabla(\nabla^2\psi^{(1)})\right]' + \left[\tilde{u}^{(1)}\frac{\partial}{\partial x}\nabla^2\psi^{(1)} + v_\psi^{(1)}\frac{\partial}{\partial y}\left(\frac{\partial^2\tilde{\psi}^{(1)}}{\partial y^2}\right)\right] + \left(\beta v_\chi^{(1)} - \frac{\partial\omega^{(1)}}{\partial y}\frac{\partial\tilde{u}^{(0)}}{\partial p}\right)\right.$$

$$+ \left[V_\chi^{(1)}\cdot\nabla(\nabla^2\psi^{(1)}) + \omega^{(1)}\frac{\partial}{\partial p}\nabla^2\psi^{(1)} - \nabla^2\psi^{(1)}\frac{\partial\omega^{(1)}}{\partial p} - \left(\frac{\partial\omega^{(1)}}{\partial y}\frac{\partial u_\psi^{(1)}}{\partial p} - \frac{\partial\omega^{(1)}}{\partial x}\frac{\partial v_\psi^{(1)}}{\partial p}\right)\right]' + \left[\tilde{v}_\chi^{(1)}\frac{\partial}{\partial y}\nabla^2\psi^{(1)} + v_\chi^{(1)}\frac{\partial}{\partial y}\left(\frac{\partial^2\tilde{\psi}^{(1)}}{\partial y^2}\right) + \tilde{\omega}^{(1)}\frac{\partial}{\partial p}\nabla^2\psi^{(1)} + \omega^{(1)}\frac{\partial}{\partial p}\left(\frac{\partial^2\tilde{\psi}^{(1)}}{\partial y^2}\right) - \frac{\partial^2\tilde{\psi}^{(1)}}{\partial y^2}\frac{\partial\omega^{(1)}}{\partial p} - \nabla^2\psi^{(1)}\frac{\partial\tilde{\omega}^{(1)}}{\partial p} - \frac{\partial\omega^{(1)}}{\partial y}\frac{\partial\tilde{u}^{(1)}}{\partial p} - \frac{\partial\tilde{\omega}^{(1)}}{\partial y}\frac{\partial u_\psi^{(1)}}{\partial p} + \frac{\partial\omega^{(1)}}{\partial x}\frac{\partial\tilde{v}^{(1)}}{\partial p}\right]\Bigg\}_{1,3},$$

$$C = \frac{4f}{p_2}\left(\frac{\partial\tilde{\psi}_T^{(1)}}{\partial y}\frac{\partial}{\partial x}\nabla^2\psi_2^{(1)} + \frac{\partial^2\psi_2^{(1)}}{\partial x\,\partial y}\frac{\partial^2\tilde{\psi}_T^{(1)}}{\partial y^2}\right) - \frac{2f}{p_2}\left(\beta\frac{\partial\psi_T^{(2)}}{\partial x} + 2\tilde{u}_T^{(0)}\frac{\partial}{\partial x}\nabla^2\psi_2^{(2)}\right).$$

9. Appendix C

Solution for the mixing ratio ε_3

Using the same notation employed in S-T (1972, 1975, 1982), the solutions of (6d), (7d), and (8c) for the components of $\varepsilon_3(x, y, t)$ represented by the expansion (1) can be expressed in the following forms, respectively:

$$\varepsilon_3^{(1)}(x, y, t) = (E_r\cos kX - E_i\sin kX)\sin ly\cdot e^{\sigma t} \qquad \text{(C1)}$$

$$\tilde{\varepsilon}_3^{(1)}(y, t) = (G_r\cos 2ly - G_i\sin 2ly)\,e^{2\sigma t}, \qquad \text{(C2)}$$

$$\varepsilon_3^{(2)} = \sum_m\sum_n\sum_p\{[Y_r(m, n, p)\cos mly + \Pi_r(m, n, p)\sin mly]\cos nkX + [Y_i(m, n, p)\cos mly + \Pi_i(m, n, p)\sin mly]\sin nkX\}\,e^{p\sigma t} \qquad \text{(C3)}$$

To save space, the coefficients in (C1), (C2) and (C3) can be written in terms of a generalized notation, whereby paired relations of the form

$$Z_r = -A + B_r + C_i + D\cdot a,$$

$$Z_i = +A - B_i + C_r + D\cdot b,$$

are condensed to the single relation

$$Z_{r,l} = \mp A \pm B_{r,l} + C_{l,r} + D(a, b),$$

and where the following definitions are introduced,

$$U \equiv \tilde{u}_3^{(0)} - c_r,$$

$$V^2 \equiv U^2 + c_l^2,$$

$$W^2 \equiv U^2 + 9c_l^2,$$

$$\tilde{\varepsilon}_y^{(0)} \equiv (\partial \tilde{\varepsilon}^{(0)}/\partial y)_3,$$

$$\Psi_3 \equiv \Psi_2 - \Psi_T,$$

$$\Lambda \equiv \frac{fl^2 |\Psi_2|^2}{2\tilde{u}_T^{(0)}(2Sl^2 p_2^2 + f^2)}.$$

As noted, all other quantities are as defined in S-T (1972, 1975, 1982). Thus, the coefficients in (C1), (C2) and (C3) can be written in the following forms,

$$E_{r,l} = V^{-2}\left[-U\left(\tilde{\varepsilon}_y^{(0)} \Psi_{3r,l} \pm \frac{\tilde{\varepsilon}_3^{(0)}}{kp_2} \Omega_{l,r}\right) \pm c_l \left(\tilde{\varepsilon}_y^{(0)} \Psi_{3l,r} \mp \frac{\tilde{\varepsilon}_3^{(0)}}{kp_2} \Omega_{r,l}\right)\right],$$

$$G_r = \Lambda \tilde{\varepsilon}_y^{(0)},$$

$$G_l = -\left[2l\Lambda\tilde{\varepsilon}^{(0)} - \frac{l}{4c_l}(E_r \Psi_{3l} - E_l \Psi_{3r})\right].$$

The only coefficients appearing in the expansion (C3) for $\varepsilon_3^{(2)}$ are of dimensionality (1, 1, 1), (0, 2, 2), (2, 2, 2), (1, 1, 3), and (3, 1, 3), that is,

$$\mathrm{Y}_{r,l}(1, 1, 1) = \pm E_{r,l}^{(a)} \pm E_{r,l}^{(c1)},$$

$$\Pi_{r,l}(1, 1, 1) = \pm E_{r,l}^{(c2)},$$

$$\mathrm{Y}_{r,l}(0, 2, 2) = \pm E_{r,l}^{(b)} \pm E_{r,l}^{(f3)},$$

$$\Pi_{r,l}(0, 2, 2) = 0,$$

$$\mathrm{Y}_{r,l}(2, 2, 2) = \pm E_{r,l}^{(f1)} \mp \frac{\mu^2}{k^2} E_{r,l}^{(b)},$$

$$\Pi_{r,l}(2, 2, 2) = \pm E_{r,l}^{(f2)},$$

$$\mathrm{Y}_{r,l}(1, 1, 3) = \mp E_{r,l}^{(c1)} \pm E_{r,l}^{(d2)} \pm E_{r,l}^{(g2)},$$

$$\Pi_{r,l}(1, 1, 3) = \mp E_{r,l}^{(c2)} \pm E_{r,l}^{(d4)} \pm E_{r,l}^{(g4)},$$

$$\mathrm{Y}_{r,l}(3, 1, 3) = \pm E_{r,l}^{(c1)} \pm E_{r,l}^{(d1)} \pm E_{r,l}^{(g1)},$$

$$\Pi_{r,l}(3, 1, 3) = \pm E_{r,l}^{(c2)} \pm E_{r,l}^{(d3)} \pm E_{r,l}^{(g3)},$$

where

$$E_{r,l}^{(a)} = \frac{l\tilde{\varepsilon}_y^{(0)}}{kp_2 \mu^2 V^2}(c_l \Omega_{r,l} \pm U\Omega_{l,r}),$$

$$E_{r,l}^{(b)} = \frac{-k}{4p_2 \mu^2 V^2}[c_l(\Omega_r E_{r,l} - \Omega_l E_{l,r}) \pm U(\Omega_r E_{l,r} - \Omega_l E_{r,l})],$$

$$E_{r,l}^{(c1)} = \pm \Lambda l \tilde{\varepsilon}_y^{(0)} W^{-2}(3c_l \Psi_{3l,r} \mp U\Psi_{3r,l}),$$

$$E_{r,l}^{(c2)} = 2\Lambda W^{-2}[-3c_l(4^{-1} f E_{l,r} + l^2 \Psi_{3l,r} \tilde{\varepsilon}_3^{(0)}) + U(4^{-1} f E_{r,l} + l^2 \Psi_{3r,l} \tilde{\varepsilon}_3^{(0)})] \mp \frac{l^2}{4c_l W^2}[(E_r \Psi_{3l} - E_l \Psi_{3r})(3c_l \Psi_{3l,r} \mp U\Psi_{3r,l})],$$

$$E_{r,l}^{(d1)} = \left[-2\Lambda\tilde{\varepsilon}_3^{(0)} + \frac{1}{4c_l}(E_r \Psi_{3l} - E_l \Psi_{3r})\right]\frac{l}{p_2} \times \left(\frac{2l^2 + \mu^2}{2\mu^2}\right)\frac{(3c_l \Omega_{r,l} \pm U\Omega_{l,r})}{kW^2},$$

$$E_{r,l}^{(d2)} = \left(\frac{2l^2 - \mu^2}{2l^2 + \mu^2}\right) E_{r,l}^{(d1)},$$

$$E_{r,l}^{(d3)} = -\frac{\Lambda\tilde{\varepsilon}_y^{(0)}}{kp_2 W^2}\left(\frac{2l^2 + \mu^2}{2\mu^2}\right)(3c_l \Omega_{r,l} \pm U\Omega_{l,r}),$$

$$E_{r,l}^{(d4)} = \left(\frac{2l^2 - \mu^2}{2l^2 + \mu^2}\right) E_{r,l}^{(d3)},$$

$$E_{r,l}^{(e1)} = -V^{-2}\{-c_l[-(\mathscr{B}_3, -\mathscr{A}_3)\tilde{\varepsilon}_y^{(0)} - (kp_2)^{-1}\tilde{\varepsilon}_3^{(0)} \times (S_a^*(1, 1, 1), Q_a^*(1, 1, 1))] + U[(\mathscr{A}_3, -\mathscr{B}_3)\tilde{\varepsilon}_y^{(0)} - (kp_2)^{-1}\tilde{\varepsilon}_3^{(0)}(Q_a^*(1, 1, 1), S_a^*(1, 1, 1))]\},$$

$$E_{r,l}^{(e2)} = -V^{-2}[c_l l(kp_2 \mu^2)^{-1}\tilde{\varepsilon}_y^{(0)} \times (S_a^*(1, 1, 1), -Q_a^*(1, 1, 1)) - Ul(kp_2 \mu^2)^{-1}\tilde{\varepsilon}_y^{(0)} \times (Q_a^*(1, 1, 1), S_a^*(1, 1, 1))],$$

$$E_{r,l}^{(f1)} = -V^{-2}\{\mp c_l[k^2(-\mathscr{D}_3, \mathscr{C}_3)\tilde{\varepsilon}_y^{(0)} - (2kp_2)^{-1}\tilde{\varepsilon}_3^{(0)} \times (S_a^*(2, 2, 2), Q_a^*(2, 2, 2))] + U[k^2(\mathscr{C}_3, -\mathscr{D}_3)\tilde{\varepsilon}_y^{(0)} - (2kp_2)^{-1}\tilde{\varepsilon}_3^{(0)} \times (Q_a^*(2, 2, 2), S_a^*(2, 2, 2))]\},$$

$$E_{r,l}^{(f2)} = -V^{-2}[\pm c_l l(4kp_2 \mu^2)^{-1}\tilde{\varepsilon}_y^{(0)} - \times (S_a^*(2, 2, 2), Q_a^*(2, 2, 2)) - Ul(4kp_2 \mu^2)^{-1}\tilde{\varepsilon}_y^{(0)} \times (Q_a^*(2, 2, 2), S_a^*(2, 2, 2))],$$

$$E_{r,i}^{(\Gamma)} = -V^{-2}\{\mp c_i[\mu^2(\mathscr{F}_3, -\mathscr{E}_3)\,\tilde{\varepsilon}_y^{(0)} + (2kp_2)^{-1}\,\tilde{\varepsilon}_3^{(0)} \times (S_a^*(0,2,2), Q_a^*(0,2,2))] + U[\mu^2(-\mathscr{E}_3, \mathscr{F}_3) \times \tilde{\varepsilon}_y^{(0)} + (2kp_2)^{-1}\,\tilde{\varepsilon}_3^{(0)}\,(Q_a^*(0,2,2), S_a^*(0,2,2))]\}.$$

$$E_{r,i}^{(s,n)} = -W^{-2}\{\mp 3c_i[\alpha_{r,i}(1,n)\,\tilde{\varepsilon}_y^{(0)} + (kp_2)^{-1} \times (\delta(n)\,\tilde{\varepsilon}_y^{(0)}\,\alpha_{r,i}(2,n) - \tilde{\varepsilon}_3^{(0)}\,\alpha_{r,i}(3,n))] + U[\tilde{\varepsilon}_y^{(0)}\,\alpha_{r,i}(4,n) + (kp_2)^{-1}\,(\delta(n)\,\tilde{\varepsilon}_y^{(0)}\,\alpha_{r,i}(5,n) - \tilde{\varepsilon}_3^{(0)}\,\alpha_{r,i}(6,n))]\},(n = 1, 2, 3, 4).$$

In the above expression for $E_{r,i}^{(s,n)}$, the quantities $\delta(n)$ and $\alpha_{r,i}$ (1–6, n) are defined as follows, with the subscripts (r, i) deleted:

$$\delta(n) = \begin{cases} 3l/(k^2 + 9l^2), & n = 1, 3 \\ l/(k^2 + l^2) & n = 2, 4, \end{cases}$$

$\alpha(1, 1) = (-\mathscr{H}_3, \mathscr{K}_3)$,

$\alpha(2, 1) = [(R_a^*(3, 1, 3) + R_g(3, 1, 3)), (P_a^*(3, 1, 3) + P_g(3, 1, 3))]$,

$\alpha(3, 1) = [S_a^*(3, 1, 3), Q_a^*(3, 1, 3)]$,

$\alpha(4, 1) = (\mathscr{K}_3, -\mathscr{H}_3)$,

$\alpha(5, 1) = [(P_a^*(3, 1, 3) + P_g(3, 1, 3), (R_a^*(3, 1, 3) + R_g(3, 1, 3))]$,

$\alpha(6, 1) = [Q_a^*(3, 1, 3), S_a^*(3, 1, 3)]$,

$\alpha(1, 2) = (-\mathscr{I}_3, \mathscr{L}_3)$,

$\alpha(2, 2) = [(R_a^*(1, 1, 3) + R_g(1, 1, 3)), (P_a^*(1, 1, 3) + P_g(1, 1, 3))]$.

$\alpha(3, 2) = [S_a^*(1, 1, 3), Q_a^*(1, 1, 3)]$,

$\alpha(4, 2) = (\mathscr{L}_3, -\mathscr{I}_3)$,

$\alpha(5, 2) = [(P_a^*(1, 1, 3) + P_g(1, 1, 3)), (R_a^*(1, 1, 3) + R_g(1, 1, 3))]$,

$\alpha(6, 2) = [Q_a^*(1, 1, 3), S_a^*(1, 1, 3)]$,

$\alpha(1, 3) = (-\mathscr{J}_3, \mathscr{G}_3)$,

$\alpha(2, 3) = -\alpha(3, 1)$,

$\alpha(3, 3) = \alpha(2, 1)$,

$\alpha(4, 3) = (\mathscr{G}_3, -\mathscr{J}_3)$,

$\alpha(5, 3) = -\alpha(6, 1)$,

$\alpha(6, 3) = \alpha(5, 1)$,

$\alpha(1, 4) = (-\mathscr{F}_3, \mathscr{K}_3)$,

$\alpha(2, 4) = -\alpha(3, 2)$,

$\alpha(3, 4) = \alpha(2, 2)$,

$\alpha(4, 4) = (\mathscr{K}_3, -\mathscr{F}_3)$,

$\alpha(5, 4) = -\alpha(6, 2)$,

$\alpha(6, 4) = \alpha(5, 2)$.

The quantities P_a^*, Q_a^*, R_a^*, and S_a^* are equal to the quantities P_a, Q_a, R_a, and S_a, respectively, given in Table 2 of S-T (1975), minus the non-linear (quadratic) terms).

REFERENCES

Anderson, R. K. and Veltishchev, N. F. 1973. The use of satellite pictures in weather analysis and forecasting, *Tech. Note No. 124*, World Meteor. Org., Geneva, 275 pp.

Carlson, T. N. 1980. Airflow through mid-latitude cyclones and the comma cloud pattern. *Mon. Wea. Rev. 108*, 1498–1509.

Lewis, W. 1957. Forecasting 700 mb dewpoint depression by a 3-dimensional trajectory technique. *Mon. Wea. Rev. 85*, 297–301.

Moen, L. 1974. A spectral model for investigation of amplifying baroclinic waves. *Tellus 26*, 424–443.

Paegle, J. N. and MacDonald, A. E. 1974. Short numerical integrations of a three-level spectral quasi-geostrophic model. *Mon. Wea. Rev. 102*, 772–783.

Phillips, N. 1954. Energy transformations and meridional circulations associated with simple baroclinic waves in a two-level, quasi-geostrophic model. *Tellus 6*, 273–286.

Saltzman, B. and Tang, C.-M. 1972. Analytical study of the evolution of an amplifying baroclinic wave. *J. Atmos. Sci. 29*, 427–444.

Saltzman, B. and Tang, C.-M. 1975. Analytical study of the evolution of an amplifying baroclinic wave: Part II. Vertical motions and transport properties. *J. Atmos. Sci. 32*, 243–259.

Saltzman, B. and Tang, C.-M. 1982. A review of some analytical studies of finite-amplitude baroclinic waves, including a new algorithm for the saturation effects of static stability and baroclinicity variations. *J. Meteorol. Soc. Japan 60*, 1–14.

Smagorinsky, J. 1960. On the dynamical prediction of large-scale condensation by numerical methods. *Geophys. Monogr. 5*, Am. Geophys. Union, 71–78.

Vallis, G. K. 1982. A statistical-dynamical climate model with a simple hydrology cycle. *Tellus 34*, 211–227.

PAPERS IN METEOROLOGICAL RESEARCH, VOL. 8, NO. 1, JUNE 1985
PUBLISHED BY THE METEOROLOGICAL SOCIETY OF THE REPUBLIC OF CHINA

Comma Cloud Development in a Two-Layer Baroclinic Model with Vertical Water Vapor Flux at Mid-Level

Chung-Muh Tang

Universities Space Research Association
The American City Building, Suite 311
Columbia, MD 21044
U.S.A.

and

Barry Saltzman

Department of Geology and Geophysics
Yale University
New Haven, CT 06511
U.S.A.

ABSTRACT

As an extension of our previous study (Saltzman and Tang, 1985) in which water vapor and cloud are confined to the lower half of the atmosphere in a growing baroclinic wave, we now allow for the vertical flux of moisture across the middle (e.g., 500 mb) level to and from the upper level. The results show that there is a tendency for the upper-level maximum mixing ratio to shift to the east relative to the lower-level maximum mixing ratio. This is consistent with the eastward tilt with height of the common form cloud in the "cold-conveyor" cross-section and the poleward tilt of the cloud in the "warm-conveyor" cross-section as observed by Carlson (1980).

1. Introduction

Saltzman and Tang (1985) (hereafter referred to as ST–85) considered the effect of finite-amplitude baroclinic waves on passive, low-level, atmospheric constituents. In particular, if water vapor is considered to be such a passive constituent it was shown that the implied relative humidity and cloud distribution would tend to evolve into the comma form commonly observed on satellite images of mid-latitude cyclone wave. The wind, temperature, relative humidity, vertical motion, and comma cloud fields exhibited in the cross-sections seem to agree with the salient features (e.g., "cold conveyor", "dry tongue", and "warm conveyor") deduced from observations by Carlson (1980). Since the moisture field in the model was confined to the lower layer

only, the schematic cloud boundaries above the middle level was speculative (cf. ST–85, Figs. 10 and 12). The purpose of this note is to show that this feature is reflected in the upper-level mixing ratio field in the model when the upper-level moisture field is taken into account.

2. The Model

We consider a two-level model as in ST–85, but now in addition to the lower-level mixing ratio field, we consider variations in the upper-level mixing ratio field. The definitions of the symbols are listed in Appendix A, ST–85. The continuity equation for an atmospheric constituent is given by

$$\frac{\partial \epsilon}{\partial t} + V \cdot \nabla \epsilon + \frac{\partial}{\partial p}(\epsilon\omega) - \epsilon \frac{\partial \omega}{\partial p} = S \quad (1)$$

Applying this equation at levels 1 and 3, we obtain

$$\frac{\partial \epsilon_1}{\partial t} + V_1 \cdot \nabla \epsilon_1 + \frac{\omega_2}{p_2}(\epsilon_2 - \epsilon_1) = S_1 \quad (2a)$$

$$\frac{\partial \epsilon_3}{\partial t} + V_3 \cdot \nabla \epsilon_3 + \frac{\omega_2}{p_2}(\epsilon_3 - \epsilon_2) = S_3 \quad (2b)$$

Next, we assume that the mixing ratio at the middle level is given by

$$\epsilon_2 = (\epsilon_3 - \epsilon_1)/2 \quad (3)$$

which would be the case, for example, if ϵ has a parabolic profile given by

$$\epsilon = \frac{K}{p_2} p^2 \quad (4)$$

where K is a function of x, y, t, only. Substitution of (3) in (2a, b) leads to

$$\frac{\partial \epsilon_1}{\partial t} + V_1 \cdot \nabla \epsilon_1 + \frac{1}{2}(\epsilon_3 - 3\epsilon_1)\frac{\omega_2}{p_2} = S_1 \quad (5a)$$

$$\frac{\partial \epsilon_3}{\partial t} + V_3 \cdot \nabla \epsilon_3 + \frac{1}{2}(\epsilon_3 + \epsilon_1)\frac{\omega_2}{p_2} = S_3 \quad (5b)$$

Next, as in ST–85, we (i) assume $S_{1,3}$ to be zero (or, alternately, that ϵ represents *total* water content, vapor plus cloud), (ii) expand each of the dependent variables $\xi = (\psi, x, \omega, \epsilon)$ into a zonal mean part $\xi(y,t)$ and an eddy part ξ', i.e.,

$$\xi = \bar{\xi} + \xi',$$

and (iii) resolve each of these parts into an initial, basic zonal field denoted by the superscript (0), a primary, quasi-geostrophic field denoted by the superscript (1) (Phillips, 1954), and a second-order, non-quasigeostrophic field denoted by the superscript (2); i.e.,

$$\bar{\xi} = \bar{\xi}^{(0)} + \bar{\xi}^{(1)} + \bar{\xi}^{(2)}$$

$$\xi' = \xi^{(1)} + \xi^{(2)}.$$

The systems of equations are as follows:

(I) Equations for the primary wave $[\psi^{(1)}, \omega^{(1)}, x^{(1)}, \epsilon^{(1)}]$:

$$\frac{\partial}{\partial t}\nabla^2 \psi^{(1)}_{1,3} + (\bar{u}^{(0)}\frac{\partial}{\partial x}\nabla^2 \psi^{(1)})_{1,3} + \beta \frac{\partial \psi^{(1)}_{1,3}}{\partial x} \mp \frac{f}{p_2}\omega_2^{(1)} = 0 \quad (6a)$$

$$\frac{\tilde{S}}{f}\nabla^2\omega_2^{(1)} - \frac{2f}{p_2^2}\omega_2^{(1)} + \frac{2\beta}{p_2}\frac{\partial\psi_I^{(1)}}{\partial x} + \frac{4}{p_2}\bar{u}_T^{(0)}\frac{\partial}{\partial x}\nabla^2\psi_2^{(1)} = 0 \quad , \tag{6b}$$

$$\nabla^2 x_{1,3}^{(1)} = \mp\frac{\omega_2^{(1)}}{p_2} \tag{6c}$$

$$\frac{\partial\epsilon_1^{(1)}}{\partial t} + \bar{u}_1^{(0)}\frac{\partial\epsilon_1^{(1)}}{\partial x} = -\frac{\partial\psi_1^{(1)}}{\partial x}\frac{\partial\bar{\epsilon}_1^{(0)}}{\partial y} - \frac{1}{2p_2}(\bar{\epsilon}_3^{(0)} - 3\bar{\epsilon}_1^{(0)})\cdot\omega_2^{(1)}, \tag{6d}$$

$$\frac{\partial\epsilon_3^{(1)}}{\partial t} + \bar{u}_3^{(0)}\frac{\partial\epsilon_3^{(1)}}{\partial} = -\frac{\partial\psi_3^{(1)}}{\partial x}\frac{\partial\bar{\epsilon}_3^{(0)}}{\partial y} - \frac{1}{2p_2}(\bar{\epsilon}_3^{(0)} + \bar{\epsilon}_1^{(0)})\omega_2^{(1)} \tag{6e}$$

(II) Equations for the forced zonal state $(\bar{\psi}^{(1)}, \bar{\omega}^{(1)}, \bar{\chi}^{(1)}, \bar{\epsilon}^{(1)}]$:

$$\frac{\tilde{S}}{f}\frac{\partial^2\bar{\omega}_2^{(1)}}{\partial y^2} - \frac{2f}{p_2}\bar{\omega}_2^{(1)} = A(\psi^{(1)}), \tag{7a}$$

$$\frac{\partial}{\partial t}\left(\frac{\partial^2\bar{\psi}^{(1)}}{\partial y^2}\right)_{1,3} = -[V_\psi^{(1)}\cdot\nabla(\nabla^2\psi^{(1)})]_{1,3} \pm \frac{f}{p_2}\bar{\omega}_2^{(1)}, \tag{7b}$$

$$\frac{\partial^2 X_{1,3}^{(1)}}{\partial y^2} = \mp\frac{\bar{\omega}_2^{(1)}}{p_2} \tag{7c}$$

$$\frac{\partial\bar{\epsilon}_1^{(1)}}{\partial t} = -\frac{\partial}{\partial y}\overline{(v_\psi^{(1)}\epsilon^{(1)})}_1 - (\bar{v}_\chi^{(1)}\frac{\partial\bar{\epsilon}^{(0)}}{\partial y})_1 - \frac{1}{2p_2}(\bar{\epsilon}_3^{(0)} - 3\bar{\epsilon}_1^{(0)})\omega_2^{(1)}, \tag{7d}$$

$$\frac{\partial\bar{\epsilon}_3^{(1)}}{\partial t} = -\frac{\partial}{\partial y}\overline{(v_\psi^{(1)}\epsilon^{(1)})}_3 - (\bar{v}_\chi^{(1)}\frac{\partial\bar{\epsilon}^{(0)}}{\partial y})_3 - \frac{1}{2p_2}(\bar{\epsilon}_3^{(0)} + \bar{\epsilon}_1^{(0)})\omega_2^{(1)} \tag{7e}$$

(III) Equations for the secondary wave fields $[\psi^{(2)}, \omega^{(2)}, \epsilon^{(2)}]$:

$$\frac{\partial}{\partial t}\nabla^2\psi_{1,3}^{(2)} + (\bar{u}^{(0)}\frac{\partial}{\partial x}\nabla\psi^{(2)})_{1,3} + \beta\frac{\partial\psi_{1,3}^{(2)}}{\partial x} \mp \frac{f}{p_2}\omega_2^{(2)} = B(\psi^{(1)}, \omega^{(1)}, \chi^{(1)}; \bar{\psi}^{(1)}, \bar{\omega}^{(1)}, \bar{\chi}^{(1)}), \tag{8a}$$

$$\frac{\tilde{S}}{f}\nabla^2\omega_2^{(2)} - \frac{2f^2}{p_2^2}\omega_2^{(2)} = C(\psi^{(1)}, \psi^{(2)}, \bar{\psi}^{(1)}), \tag{8b}$$

$$\frac{\partial}{\partial t}\epsilon_1^{(2)} + (\bar{u}^{(0)}\frac{\partial\epsilon^{(2)}}{\partial x})_1 = -[v_\chi^{(1)}\frac{\partial\bar{\epsilon}^{(0)}}{\partial y} + (u_\chi^{(1)}\frac{\partial\epsilon^{(1)}}{\partial x})' + (v_\chi^{(1)}\frac{\partial\epsilon^{(1)}}{\partial y})' + \bar{u}_\psi^{(1)}\frac{\partial\epsilon^{(1)}}{\partial x}) + v_\psi^{(1)}\frac{\partial\epsilon^{(1)}}{\partial y} + v_\chi^{(1)}\frac{\partial\bar{\epsilon}^{(1)}}{\partial y}$$

$$+ v_{\psi}^{(2)}\frac{\partial\bar{\epsilon}^{(0)}}{\partial y} + v_{\chi}^{(2)}\frac{\partial\bar{\epsilon}^{(0)}}{\partial y}\Big]_1$$

$$-\frac{1}{2p_2}\{[(\epsilon_3^{(1)}-3\epsilon_1^{(1)})\omega_2^{(1)}]+[(\bar{\epsilon}_3^{(1)}-3\bar{\epsilon}_1^{(1)})\omega_2^{(1)}]+[(\bar{\epsilon}_3^{(0)}-3\bar{\epsilon}_1^{(0)})\omega_2^{(1)}]\}, \quad (8c)$$

$$\frac{\partial}{\partial t}\epsilon_3^{(2)}+(\bar{u}^{(0)}\frac{\partial\epsilon^{(2)}}{\partial x})_3$$

$$= -[v_{\chi}^{(1)}\frac{\partial\bar{\epsilon}^{(0)}}{\partial y} + (u_{\chi}^{(1)}\frac{\partial\epsilon^{(1)}}{\partial x})' + (v_{\chi}^{(1)}\frac{\partial\epsilon^{(1)}}{\partial x})'$$

$$+ \bar{u}_{\psi}^{(1)}\frac{\partial\epsilon^{(1)}}{\partial x} + v_{\psi}^{(1)}\frac{\partial\epsilon^{(1)}}{\partial y} + v_{\chi}^{(1)}\frac{\partial\bar{\epsilon}^{(1)}}{\partial y}$$

$$+ v_{\psi}^{(2)}\frac{\partial\bar{\epsilon}^{(0)}}{\partial y} + v_{\chi}^{(2)}\frac{\partial\bar{\epsilon}^{(0)}}{\partial y}\Big]_3$$

$$-\frac{1}{2p_2}\{[(\epsilon_3^{(1)}+\epsilon_1^{(1)})\omega_2^{(1)}]'$$

$$+[(\bar{\epsilon}_3^{(1)}+\bar{\epsilon}_1^{(1)})\omega_2^{(1)}]+[(\bar{\epsilon}_3^{(0)}+\bar{\epsilon}_1^{(0)})\omega_2^{(1)}]\} \quad (8d)$$

As in ST–85, where the double signs appear the upper sign refers to level 1 (250 mb) and the lower sign refers to level 3 (750 mb); $\hat{S}$ is the horizontally uniform value of static stability, and A, B, and C are the non-homogeneous forcing functions due to lower order fields given in Appendix B in ST–85. Again, we approximate C (=F_g + F_a, Saltzman and Tang 1975) by including only the linear terms in F_g. We also neglect ω_2 (2). The solutions for ϵ_1 and ϵ_3 can be obtained by using the formulas for the streamfunction, temperature, vertical motion, and velocity potential in Saltzman and Tang (1972, 1975), plus the basic mixing ratio and its meridional gradient. The derivations are straightforward, but rather lengthy, and we shall not present them here.

3. Results

Before we present the new solution, we show in Fig. 1 a corrected version of Fig. 5 of ST–85 portraying the evolution of the low-level water vapor mixing ratio field ϵ_3. Notice that the main error is in the region of sinking motion where a weaker minimum appears, corresponding to only a small area of negative values. Since the western cloud boundary is mainly determined by the eastern boundary of the sinking region, the comma-type cloud distribution remains virtually the same.

The parameters in the present model are the same as those in ST–85, except that we consider only the case $\bar{\epsilon}_1^{(0)}(D/2)=(2/9)\times10^{-3}$, $\bar{\epsilon}_3^{(0)}(D/2)=2\times10^{-3}$ and $\partial\bar{\epsilon}_1^{(0)}/\partial y = -(1/3)\times10^{-10}\,m^{-1}$, $\partial\bar{\epsilon}_3^{(0)}/\partial y=-3\times10^{-10}\,m^{-1}$. Note that these prescribed values satisfy (4).

In Fig. 2 we show the mixing ratio at level 1 (250 mb) and at level 3 (750 mb) at t=4.8, 5.2 and 5.6 days. The upper-level maximum tends to be shifted eastward relative to the lower-level maximum as would be expected given the increasing westerly wind speed with height. The lower-level field is similar to Fig. 1 but now $\epsilon 3$ is everywhere positive and its maximum is smaller than that in Fig. 1. However, negative values appear at the upper level. As noted by Lorenz (1984) this feature arises from

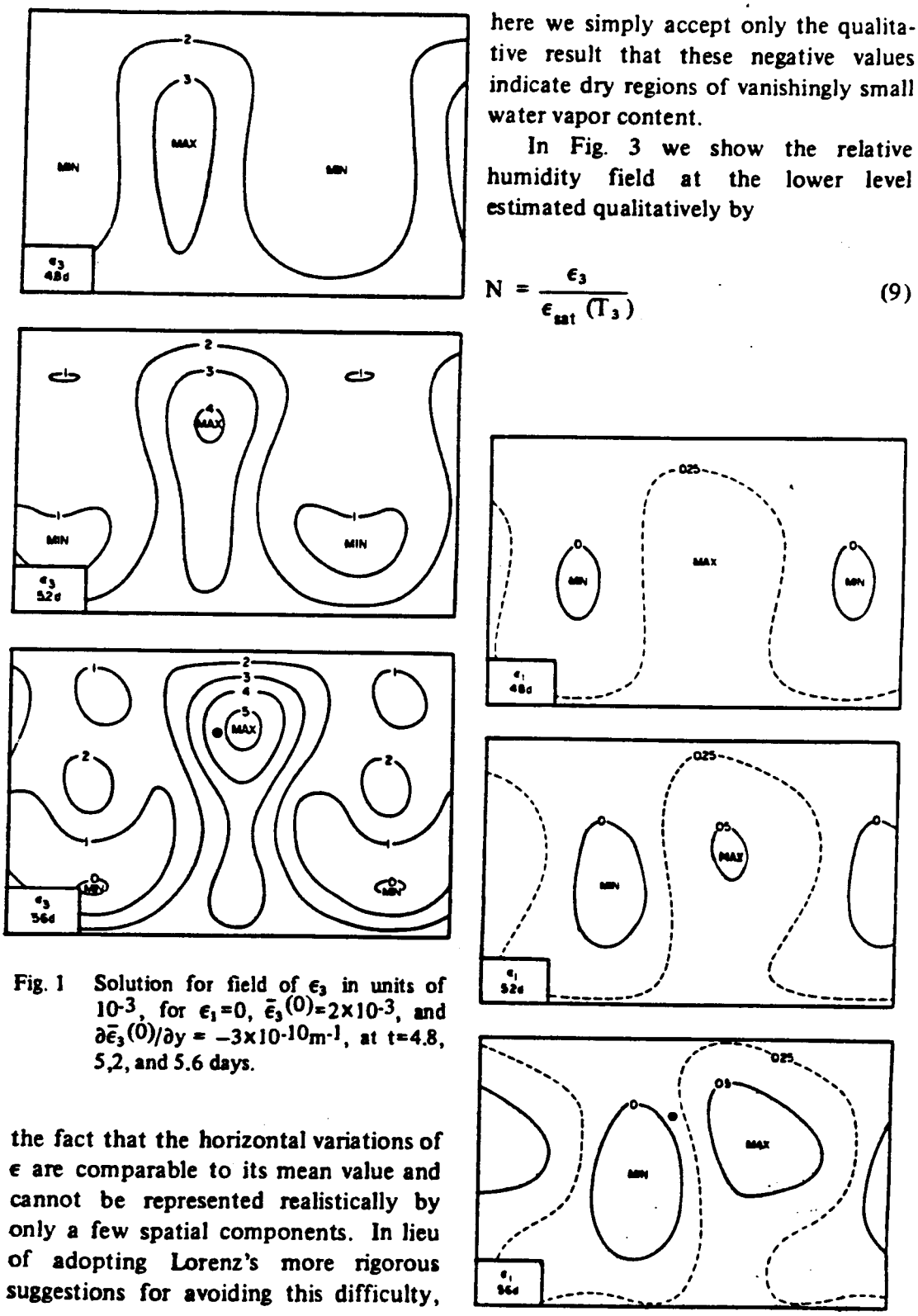

Fig. 1 Solution for field of ϵ_3 in units of 10^{-3}, for $\epsilon_1=0$, $\bar{\epsilon}_3(0)=2\times10^{-3}$, and $\partial\bar{\epsilon}_3(0)/\partial y = -3\times10^{-10}m^{-1}$, at t=4.8, 5.2, and 5.6 days.

the fact that the horizontal variations of ϵ are comparable to its mean value and cannot be represented realistically by only a few spatial components. In lieu of adopting Lorenz's more rigorous suggestions for avoiding this difficulty, here we simply accept only the qualitative result that these negative values indicate dry regions of vanishingly small water vapor content.

In Fig. 3 we show the relative humidity field at the lower level estimated qualitatively by

$$N = \frac{\epsilon_3}{\epsilon_{sat}(T_3)} \tag{9}$$

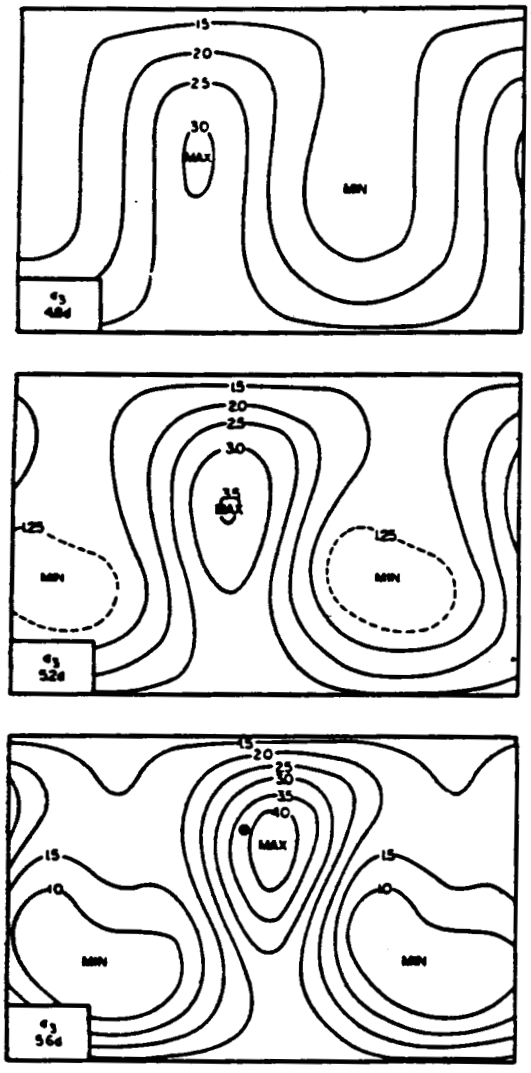

Fig. 2 Solution for the fields of ϵ_1 (left) and ϵ_3 (right) in units of 10^{-3}, for $\bar{\epsilon}_1(0) = (2/9)\times10^{-3}$, $\bar{\epsilon}_3(0) = 2\times10^{-3}$, and $\partial\bar{\epsilon}_1(0)/\partial y = -(1/3)\times10^{-10}\,m^{-1}$, and $\partial\bar{\epsilon}_3(0)/\partial y = -3\times10^{-10}\,m^{-1}$, at t=4.8, 5.2, and 5.6 days.

We note that unrealistic supersaturation still occurs. In Fig. 4 we show the cloud coverage obtained by applying the condition used previously, i.e., $r > 0.50$ and $\omega < 0$. As before the comma or scallop shape cloud distribution is seen to develop as time progresses.

4. Conclusion

It appears that the qualitative cloud sketch in the cross-sections shown in Figs. 10 and 12 of ST–85 is supported

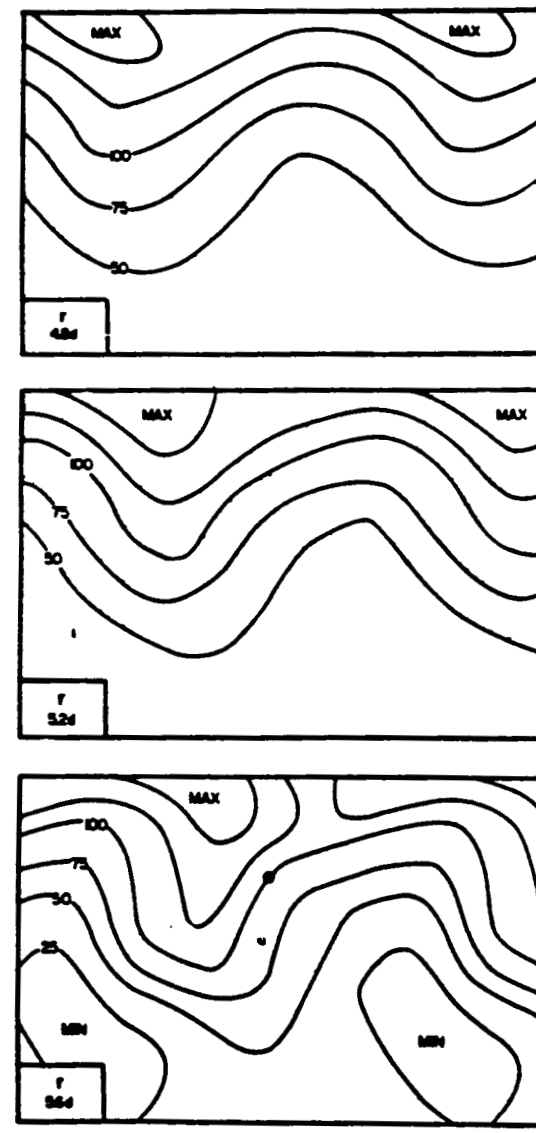

Fig. 3 Field of relative humidity at the lower level, r, in units of %, corresponding to ϵ_3 fields shown in Fig. 2, for t=4.8, 5.2 and 5.6 days.

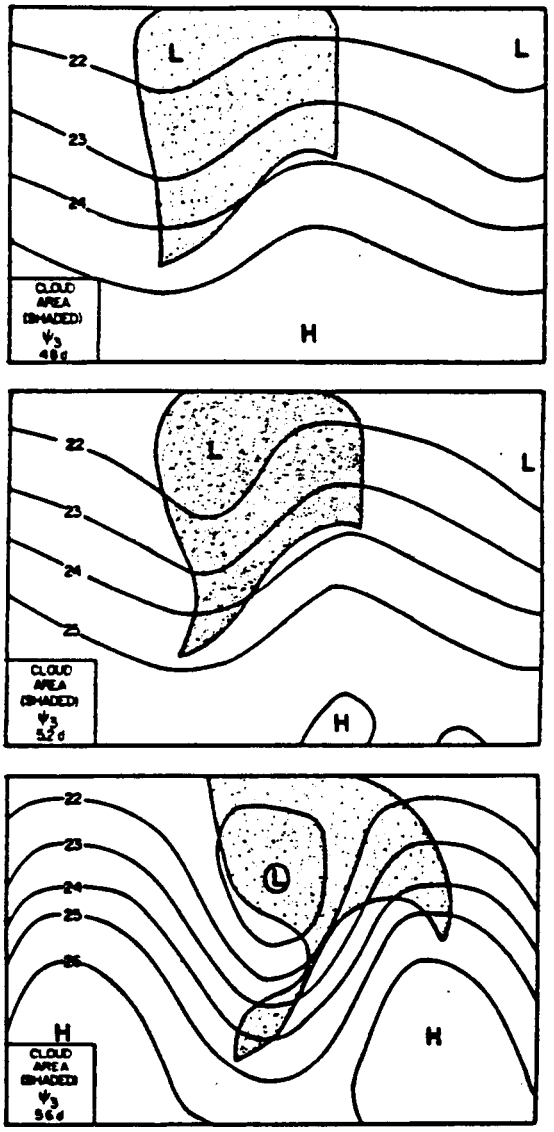

Fig. 4 Cloud areas deduced from the condition ($r > 0.50$, $\omega < 0$) applied to Fig. 3, for t=4.8, 5.2 and 5.6 days.

by the present calculation of the moisture fields in the upper and lower levels. Note,, in particular, that the eastward tilt of the cloud in Fig. 10 of ST–85 is consistent with the eastward tilt of the maximum mixing ratio in Fig. 2 of the present paper. The other deficiencies mentioned in ST–85 still remain however.

ACKNOWLEDGEMENTS

This study was supported by the National Aeronautics and Space Administration under contract NAS8–34903 at Yale University and NAS8–36474 at the Universities Space Research Association.

REFERENCES

Carlson, T.N., 1980: Airflow through mid-latitude cyclones and the comma cloud pattern. *Mon. Wea. Rev., 108*, 1498–1509.

Lorenz, E.N., 1984: Formulation of a low-order model of a moist general circulation. *J. Atmos. Sci., 41*, 1933–1945.

Phillips, N., 1954: Energy transformations and meridional circulations associated with simple baroclinic waves in a two-level, quasi-geostrophic model. *Tellus, 6*, 273–286.

Saltzman, B. and Tang, C.-M., 1972. Analytical study of the evolution of an amplifying baroclinic wave. *J. Atmos. Sci., 29*, 427–444.

———., 1975. Analytical study of the evolution of an amplifying broclinic wave. Part II. Vertical motions and transport properties. *J. Atmos. Sic., 32*, 243–259.

———., 1985: The effect of finite-amplitude baroclinic waves on passive, low-level, atmospheric constituents, with applications to comma cloud evolution. *Tellus, 37A*, 41–55.

逗點雲在垂直水汽通量穿越中層的二層斜壓模式之發展

Chung-Muh Tang

Universities Space Research Association
The American City Building, Suite 311
Columbia, MD 21044
USA

Barry Saltzman

Department of Geology and Geophysics
Yale University
New Haven, CT 06511
USA

本文係上一篇報告（Saltzman and Tang 1985）的延伸，前文中水汽與雲限制在成長斜壓波的下半層，現在水汽的垂直通量能穿越 500 mb ，出入上半層，結果顯示；上半層最高混合比往往偏向于低層最高混合比的東面。這和 Carlson （1980）所觀察到的，冷鋒逆切面中，圖高度往東傾斜的逗點狀雲以及熱鋒逆切面中往極點傾斜的雲一致。

Reprinted from MONTHLY WEATHER REVIEW, Vol. 112, No. 7, July 1984
American Meteorological Society
Printed in U. S. A.

Estimates of the Generation of Available Potential Energy by Infrared Radiation

ANTHONY R. HANSEN[1] AND RICHARD L. NAGLE

Department of Geology and Geophysics, Yale University, New Haven, CT 06511

(Manuscript received 23 December 1983, in final form 20 April 1984)

ABSTRACT

Data from the National Meteorological Center and net outgoing infrared radiation (IR) data measured by NOAA satellites for January 1977 are used to compute estimates of the spectral and spatial contributions to the net generation of available potential energy in the Northern Hemisphere due to infrared radiation. Although these estimates are necessarily crude, the results obtained indicate that IR causes destruction of both zonal and eddy available potential energy. The contributions from midlatitudes to the zonal and eddy generation are $G_Z \approx -5.0$ W m^{-2} and $G_E \approx -0.6$ W m^{-2}, respectively. The eddy generation is due almost entirely to stationary wavenumbers 1 and 2. Comparison with earlier studies and computation of Newtonian cooling coefficients are discussed.

1. Introduction and background

Diabatic heating in the atmosphere is composed of four principal contributions. These are: 1) absorption of solar radiation; 2) emission and absorption of longwave (infrared) radiation; 3) heating due to the release of latent heat of condensation; and 4) transfer of sensible heat from the surface of the earth to the atmosphere. The characteristics of atmospheric diabatic heating are of crucial importance because it is the nonuniform distribution of diabatic heating that is the driving force behind the general circulation. A measure of this effect in the atmospheric energy cycle is given by the generation of available potential energy (APE), which is determined by the spatial correlation of the diabatic heating with the atmospheric temperature field (Lorenz, 1955). The rate of APE generation is one measure of the intensity of the general circulation (Wiin-Nielsen, 1968).

Diabatic heating and APE generation are difficult quantities to measure and are conventionally estimated as budget residuals. Two approaches have been used traditionally to compute the diabatic heating. First, the heating is computed as a residual in a heat budget (Wiin-Nielsen and Brown, 1962; Brown, 1964; Geller and Avery, 1978) or potential vorticity budget (Lawniczak, 1969). In principle, the residual methods can give the spatial and temporal distributions of the heating field. However, they are limited by data quality and the need to compute vertical velocities in the heat budget calculation. The second approach is to use detailed radiation models to compute the time mean and (often) zonal mean radiational heating fields (Katayama, 1967; Newell *et al.*, 1974; Freeman and Liou, 1979). Latent heat release and surface sensible heat flux terms must be estimated independently. Unfortunately, this approach must necessarily deal with the time mean heating because the radiation models require assumptions about the mean temperature, cloudiness (amount and level) and atmospheric composition (water vapor, aerosols, etc.). Therefore, these studies by their very nature cannot deal with the transient part of the diabatic heating and APE generation. Newell *et al.* (1974) were further constrained to the time averaged, zonal mean APE generation, although Katayama (1967) made estimates of the standing eddy APE generation.

In this report, we use an alternative approach to estimate the contribution of infrared cooling to the APE generation. We use NOAA satellite measurements of outgoing infrared radiation (Gruber and Winston, 1978) combined with NMC height field data to determine temperature, both for January 1977, to estimate the spectral and geographic contributions to this component of the generation. Suomi and Shen (1963) were the first to use this approach to estimate IR-induced APE generation on selected dates and for selected areas during 1959 and 1960. They found the generation due to IR to be comparable in magnitude with other estimates of the total APE generation and to exhibit significant temporal variability.

2. Data and approach

The total rate of APE generation G can be expressed as the sum of various spatial and temporal contributions:

$$G = G_Z + G_E = G_{ZS} + G_{ZT} + G_{ES} + G_{ET},$$

[1] Present affiliation: Meteorology Research Center, Control Data Corporation, Minneapolis, MN 55440.

where subscripts Z refer to zonally averaged quantities

$$( )_Z = \frac{1}{2\pi}\int_0^{2\pi} ( )d\lambda$$

and E to eddy quantities $( )_E = ( ) - ( )_Z$, and the subscripts S and T refer to the stationary (time mean) mode

$$( )_S = \frac{1}{t_2 - t_1}\int_{t_1}^{t_2} ( )dt$$

and transient mode $( )_T = ( ) - ( )_S$, respectively. Using Lorenz' (1955) approximate form, these contributions can be written as

$$G_{ZS} = [\gamma q'_{ZS} T'_{ZS}], \quad (1)$$

$$G_{ZT} = [\gamma (q'_{ZT} T'_{ZT})_S], \quad (2)$$

$$G_{ES} = [\gamma (q_{ES} T_{ES})_Z], \quad (3)$$

$$G_{ET} = [\gamma (q_{ET} T_{ET})_{ZS}], \quad (4)$$

where the brackets denote an average over the mass of the atmosphere normalized per unit area, q is the diabatic heating rate per unit mass, T the temperature, $\gamma = R^2/(p^2 c_p \bar{\sigma})$,
and

$$\bar{\sigma} = -\frac{\alpha}{\theta}\frac{\partial \theta}{\partial p}$$

is a measure of the static stability. A value of $\bar{\sigma}$ for the 850–300 mb layer was adapted from Tomatsu (1979). Departures of the zonal mean heating and temperature from their hemispheric mean values are denoted by q'_Z and T'_Z, respectively. (We will ignore departures of the hemispheric means from the global means.) Dutton and Johnson (1967) and Newell *et al.* (1974) discuss the validity of these approximate forms of G_{ZS} and G_{ZT}. In addition, the eddy components of the generation can be broken down into zonal harmonic spectra

$$G_E = \sum_m G_m = \sum_m [\gamma (q_m T^*_m + q^*_m T_m)],$$

where the subscript m denotes the contribution for wavenumber m, and an asterisk denotes a complex conjugate of the coefficients q_m or T_m. Thus, relative cooling of relatively warm air or relative heating of relatively cold air will result in destruction of APE and vice versa.

The infrared radiation data that we use are those measured by the scanning radiometers aboard NOAA operational polar-orbiting satellites. Descriptions of the instruments and data reduction procedures are given by Gruber and Winston (1978). The satellite's equator-crossings occur at 0900 and 2100 LST daily. We average the twice-daily observations to get daily average values at each grid point of a 2.5° latitude–longitude array. The NOAA satellite observes IR in the atmospheric "window region" (10.5–12.5 μm wavelengths). In the analysis procedure used by NOAA, estimates are made of the total outgoing IR flux from these window region radiance measurements by using a nonlinear regression model derived from radiation calculations for 99 different atmospheres covering a wide variety of temperature and moisture conditions as well as clear and cloudy skies (Gruber and Winston, 1978).

Let us briefly discuss the sources of the net outgoing IR. The surface of the earth or of a cloud radiates essentially as a blackbody. A portion of this radiation is transmitted by the atmosphere to space and the remainder is absorbed by atmospheric gases, primarily water vapor, carbon dioxide and ozone, or by clouds. These constituents then reradiate IR at an intensity appropriate to their temperature and emissivity. For a long-term global mean, most of the IR leaving the top of the atmosphere comes from the atmosphere itself. However, the distribution of the total outgoing IR is particularly dependent upon the distribution of cloudiness and water vapor in the atmosphere (Weinstein and Suomi, 1961; Paltridge and Platt, 1976; Freeman and Liou, 1979; Ohring and Gruber, 1983).

Our interest is in estimating the tropospheric IR cooling rate from the satellite measurements. Earlier studies (e.g., Kuhn and Suomi, 1960; Sabatini and Suomi, 1962) indicate that satellite measurements of outgoing IR give a good estimate of the net IR flux divergence from the troposphere compared to direct radiometersonde measurements. However, some unknown contribution to the satellite-derived IR flux will be provided by emission from the earth's surface. For a long-term, global mean this fraction will be roughly 20% of the total (Paltridge and Platt, 1976). In cloud-free conditions it will be closer to 50% (or greater in regions of low water vapor content, i.e., near the pole), while in regions of overcast it will be near zero. In winter, average daytime cloudiness typically exceeds 75% over midlatitude oceans and 50% over midlatitude continents (except in desert regions) (Clapp, 1964), suggesting a generally smaller contribution from the surface to the satellite IR observations. However, the vertical distribution of the cloudiness is crucial in determining its effect on the tropospheric cooling rate for a given temperature and moisture profile (Cox, 1969). Unfortunately, the available satellite observations cannot determine the vertical structure of the cooling rate. As an approximation, we shall assume that a linear relationship exists between measured outgoing IR and the resultant tropospheric cooling rate due to this radiation.

Following Suomi and Shen (1963), we will assume that the satellite-observed IR is representative of the vertical mean value for the troposphere (1000–100 mb layer) and will ignore correlations between q and T

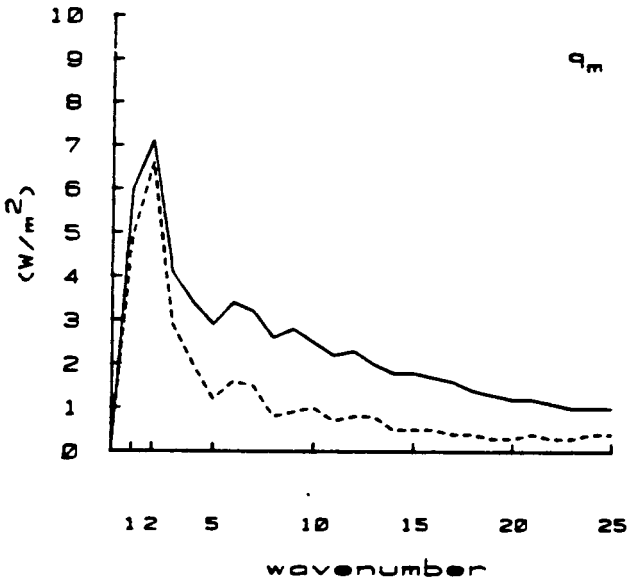

FIG. 1. The amplitude of $[|q_m|]$, for the total IR (solid line) and time-mean contribution ($[|q_{m_t}|]$, dotted line) for January 1977 as the function of the zonal wavenumber m. In this case, q_m is averaged over the zone from 30 to 80°N.

due to variations about their vertical average. This is a crude but acceptable first approximation. Freeman and Liou's (1979) model, for example, indicates that variations in q_{zs} about its vertical mean are not excessively large for January conditions, particularly in extratropical latitudes. By making this assumption, we will overestimate the tropospheric cooling rate by ignoring the contribution to the satellite-observed IR flux given by radiation from the earth's surface transmitted by the atmosphere and by radiation from layers above the troposphere. The former contribution could account for up to 50% of the total observed irradiance in certain locations and the latter effect is probably small.

Tropospheric mean temperatures are computed hydrostatically from the NMC operational analyses of the 1000 and 100 mb geopotential heights. These data are available twice daily at 0000 and 1200 GMT and were averaged to give daily mean temperatures. Certain inaccuracies may be introduced because the satellite data and temperature data are not synoptic, leading to misinterpretation of the transient part of G. However, for slowly evolving, large spatial scales, this problem should not be serious.

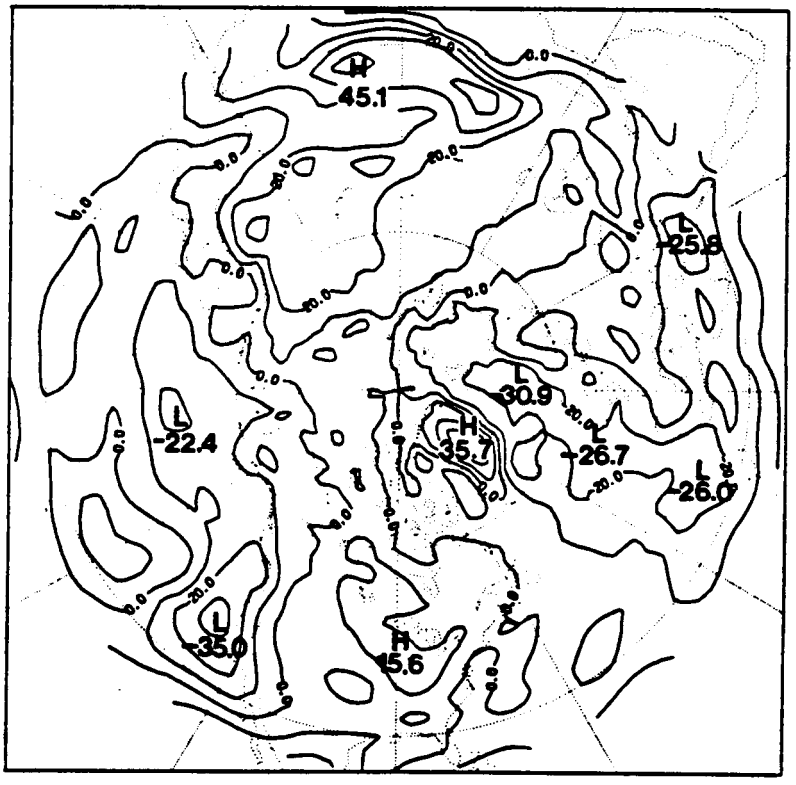

FIG. 2. The geographic distribution of q_{ES} in the zone from 25 to 80°N. The field plotted is the IR *heating rate* (W m^{-2}), so negative values indicate strong cooling and positive values indicate relative warming. Contour interval is 10 W m^{-2}. Contributions to q_{ES} from wavenumbers higher than 25 have been removed.

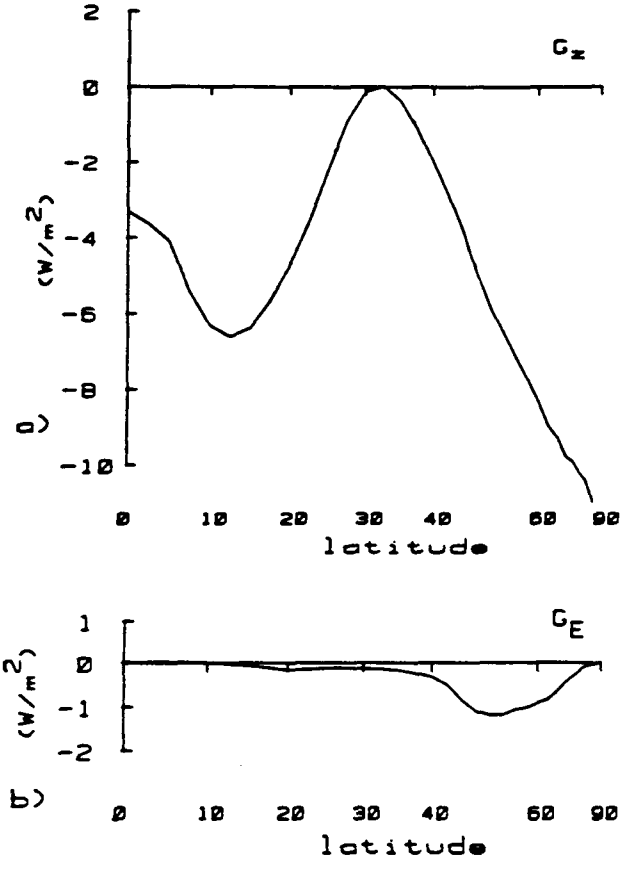

FIG. 3. The integrands of G_Z (a) and G_E (b) as functions of latitude.

Although our admittedly crude assumptions may introduce certain systematic errors into our calculation, if at least the phase of the net cooling rate is correct, we can proceed with our estimate of the APE generation. However, we must keep in mind that our estimates of G will at best achieve the correct sign and the correct order of magnitude.

TABLE 1. Average values during January 1977 for the contributions to the IR-produced generation of available potential energy (W m^{-2}) in the zones noted. For comparison, Katayama's (1967) values from a radiation model calculation are included.

Zone	G_Z	G_{ZS}	G_E	G_{ES}
30–80°N	−4.98	−4.96	−0.61	−0.61
0–90°N	−4.74	−4.73	−0.33	−0.31
Katayama (1967) IR (0–90°N)	—	−3.443	—	−0.242
Katayama (1967) SR* (0–90°N)	—	2.914	—	−0.005

* Solar radiation.

3. Results

We will present results for January 1977 only. Calculations for January 1978 showed qualitatively similar features. First, consider the amplitude spectrum of the eddy infrared cooling rate $[|q_m|]_s$ (Fig. 1). Notice that maximum values are obtained at planetary-scale wavenumbers, suggesting the important sensitivity of q_m to the large-scale temperature field. Examination of the geographic distribution of q_{ES} (Fig. 2) shows that certain geographic features leave a strong signature in the radiation field. Features such as the Tibetan

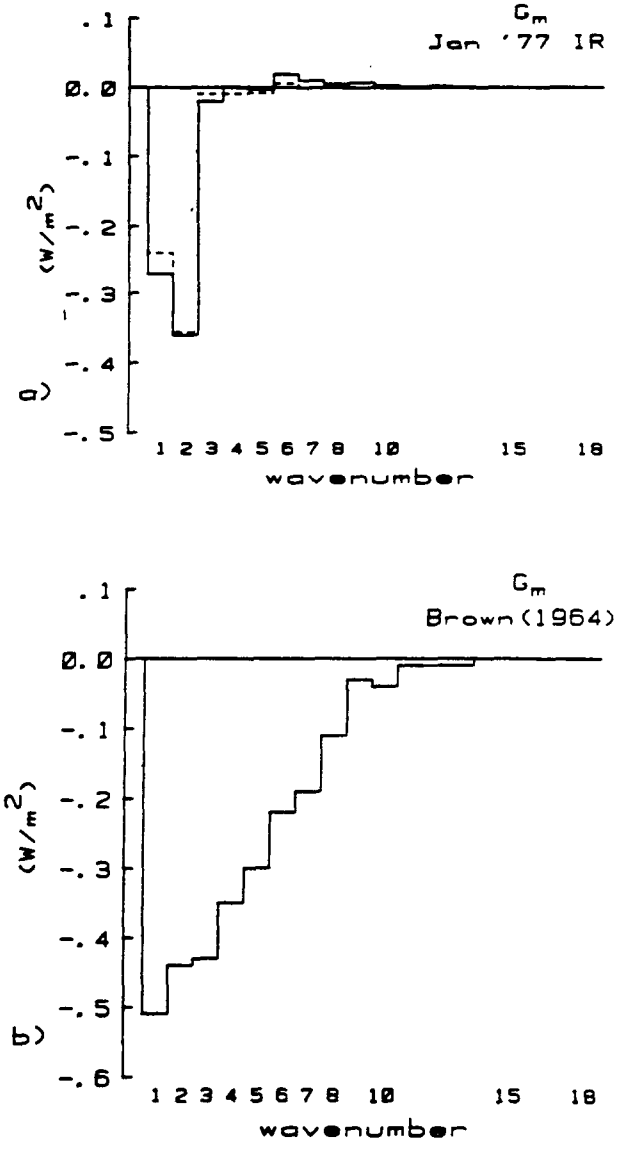

FIG. 4. The spectrum of G_E for (a) our results for the IR contribution in January 1977 where the solid line is the total G_m and the dashed line is G_{mz}, and (b) Brown's (1964) estimates of the total G_m averaged for three Januaries (1959, 1962, 1963.) Our values are averaged for 30–80°N and Brown's values are for 20–87.5°N.

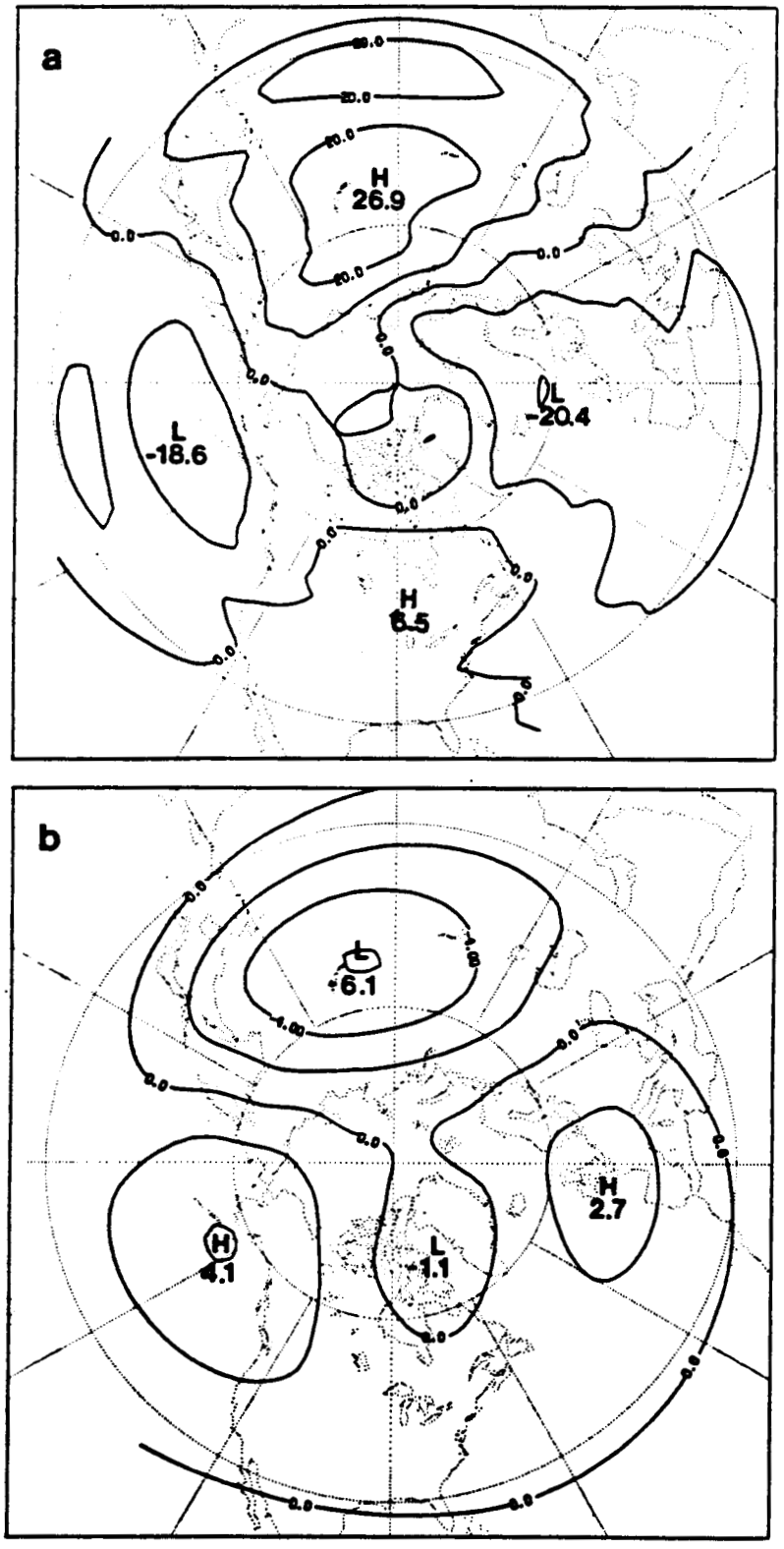

FIG. 5. The geographic distribution of the ultralong-wave fields (zonal wavenumbers 1–2) of (a) $\sum_{m=1}^{2} q_{mu}$ (W m^{-2}), (b) $\sum_{m=1}^{2} T_{mu}$ (°C) and (c) the integrand of $\sum_{m=1}^{2} G_{mu}$ (W m^{-2}) for January 1977. Contour intervals are 10 W m^{-2}, 2°C and 1 W m^{-2}, respectively.

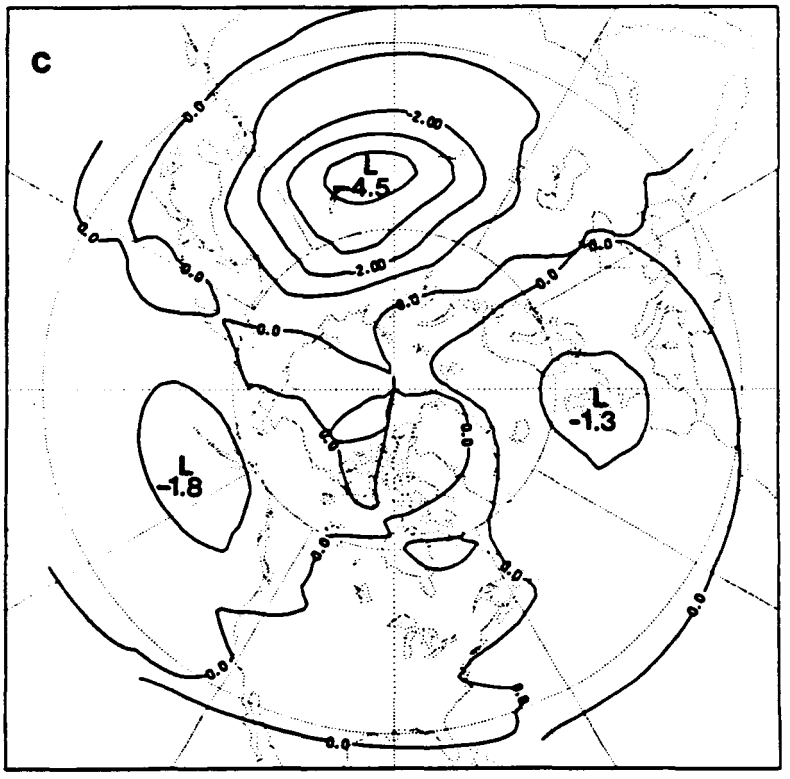

FIG. 5. (*Continued*)

plateau and Greenland are clearly evident. Most of these features are represented by wavenumbers higher than 3, however. At the planetary scale, the IR distribution mirrors the temperature field, as we will show shortly. The monthly mean field of q_{ES} for January 1977 does show certain large departures from the mean for the eight Januaries from 1975 through 1982 (not shown). In particular, the strong cooling off the California coast in January 1977 has an amplitude nearly twice the eight-January mean value.

In Fig. 3 the integrands of G_Z and G_E are presented as functions of latitude. The monthly mean values are contributed almost entirely by the stationary mode (See Table 1). The relative maximum in the G_Z integrand (Fig. 3a) near the equator is due to persistent high cloudiness near the ITCZ and the resultant reduction in radiation from the troposphere (during summer, preliminary estimates indicate that this effect can result in a positive contribution to G_Z in the tropics due to IR). A minimum in the integrand of G_Z occurs at ~12.5°N due to relatively cloud-free conditions and large IR cooling rates in this zone (Gruber and Winston, 1978). From a zero value near 30°N, the G_Z integrand decreases monotonically toward polar regions. Contributions to G_E (Fig. 3b) are only important between 35 and 75°N, reaching values of approximately -1 W m^{-2} between 45 and 60°N. Katayama (1967) estimated G_{ZS} and G_{ES} for the Northern Hemisphere based upon mean heating rates from a detailed radiation model. His results are quite similar to ours (Table 1), suggesting that the approximations we have made are acceptable. In addition, Katayama's results for G_{ES} due to absorption of solar radiation indicate that this contribution is extremely small (<0.01 W m^{-2}). Thus, the infrared contribution to G_{ES} may be equivalent to the total radiational contribution.

The spectrum of G_E (Fig. 4a) reveals that the total G_E is contributed almost entirely by the standing component of wavenumbers 1 and 2. This contribution by the ultralong waves is competitive with the total G_m at wavenumbers 1 and 2 computed by Brown (1964; January values reproduced in Fig. 4b). The small positive values of G_m at intermediate wavenumbers may be the result of a cumulative effect due to positive APE generation in the developing stage of cyclones (Vincent *et al.*, 1977), but it is too small to be of importance to the mean energetics. We should add, of course, that the spectrum of G_E is not linearly related to the spectrum of the APE (not shown).

The spectral energetics for the winter of 1976–77 have been presented by Chen (1982). Comparison with his calculations of the zonal to eddy APE conversion $C(A_Z, A_E)$, the eddy APE to eddy kinetic energy conversion $C(A_E, K_E)$, and wave–wave interactions for the ultralong waves shows that the IR-induced APE destruction is a significant term in the APE budget of

the standing ultralong waves, accounting for 70–80% of the required balancing of the APE budget residual at these length scales.

Because the standing ultralong waves make the major contribution to the IR-induced G_E, it is of interest to examine the geographic distribution of the ultralong-wave IR heating and temperature fields, as well as their correlation (Fig. 5). Notice the tendency for the IR heating and temperature fields to be out of phase, leading to large negative contributions to G_{ES} over interior Asia with lesser contributions over the northeast Pacific and over western Europe and the eastern Atlantic (Fig. 5c).

The destruction of eddy APE in midlatitudes measured by Brown (1964) may be largely due to air mass modification over the Gulf Stream and Kuroshio. This process would presumably take place at primarily intermediate scales. If Brown's and our results are representative and comparable, we could infer that a significant amount of the total destruction of eddy APE at wavenumbers 1 and 2 is due to radiational processes, while radiational processes are energetically unimportant at intermediate scales.

Although the transient mode makes no contribution to the total monthly mean G_Z and G_E, this does not mean that it is zero on any given day. The time series for G_Z and G_E averaged over 30–80°N (Figs. 6a and b) show significant departures from the monthly mean that appear systematic rather than random. The departures of G_Z and G_E from their monthly mean values are nearly always directly out of phase with the temporal variations of A_Z and A_E (not shown), a not altogether surprising result which is consistent with the strong dependence of the cooling rate on temperature.

One source of systematic error in our calculation is probably the lack of vertical resolution in our computations. For instance, we have compared the APE calculated from the 1000–100 mb thickness with that calculated from the NMC analyses of observed temperatures at the ten mandatory levels in the troposphere. Although the APE calculated in the present study is fairly accurate for wavenumbers 1, 2 and 3, it is consistently underestimated by a factor of 3 or more for wavenumbers 4 and higher. A phase reversal of the intermediate-scale temperature waves between the lower and upper troposphere most likely explains this discrepancy. This implies that G_m for these wavenumbers is also underestimated. Although the intermediate scale G_m would then assume larger positive values, it would still be small compared to other APE budget terms.

Finally, we can use our results to compute a Newtonian cooling coefficient α in a manner analogous to that used by Saltzman (1973). This coefficient, which is a time constant for the destruction of eddy temperature variance due to longwave radiation, can be defined as

$$\alpha = \frac{(q_E T_E)_{zs}}{[C_p(T_E^2)_{zs}]}.$$

We get $\alpha \approx 3 \times 10^{-7}\ s^{-1}$ ($\alpha^{-1} \approx 38$ days).

As already mentioned, Katayama (1967) indicates that the contribution of solar radiation to G_{ES} is negligible and so its contribution to the total G_E is probably small also. Our α may therefore be representative of the total radiational damping coefficient and would apply only to the ultralong waves, since the radiational contribution to G_E for smaller scales is negligible. Wiin-Nielsen *et al.* (1967) obtained a somewhat larger value for α ($4 \times 10^{-7}\ s^{-1}$) based on Brown's (1964) total diabatic heating. Saltzman (1973) obtained a much larger value, $\alpha = 2 \times 10^{-6}\ s^{-1}$, appropriate to the total diabatic heating at 850 mb. This seems plausible due to the large influence of boundary-layer effects at that level.

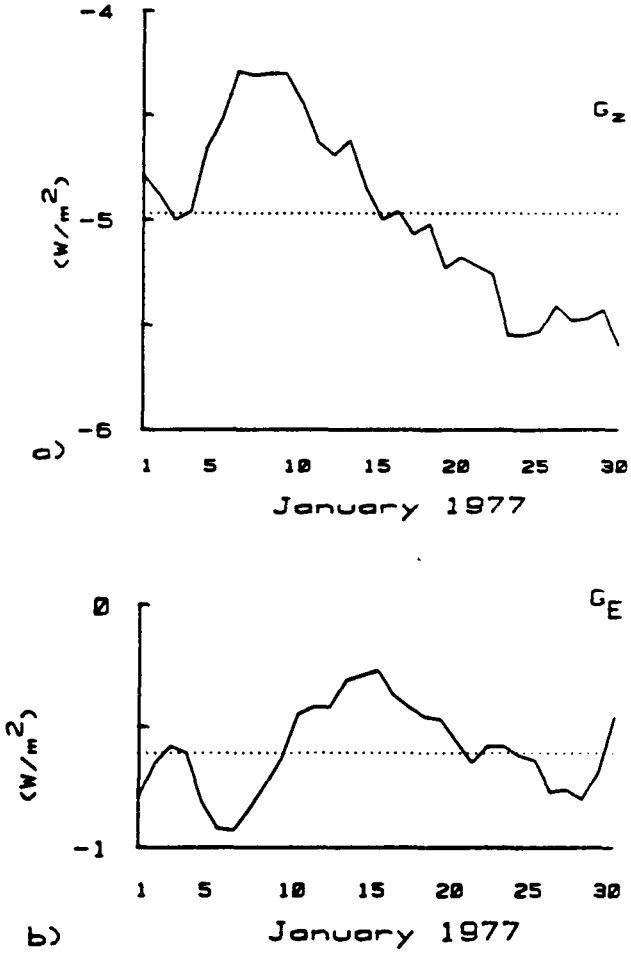

FIG. 6. The time series of the IR-produced G_Z (a) and G_E (b). The values shown are the contributions to G_Z and G_E for the zone 30–80°N. The dotted line indicates the value of G_{ZS} and G_{ES} in (a) and (b), respectively.

4. Conclusions

The infrared cooling contribution to G_Z and G_E in winter based on satellite observations of the infrared cooling rate is negative. Further, the satellite-based estimates compare well with available radiation-model-based estimates despite the assumptions about the source and vertical uniformity of the observed cooling rate. The contribution of G_Z in winter is negative at all Northern Hemisphere latitudes while contributions to G_E are only significant in the 35–70°N zone and are due almost entirely to standing wavenumbers 1 and 2. A Newtonian cooling coefficient of $\sim 3 \times 10^{-7}$ s^{-1} applicable to the ultralong waves was calculated, corresponding to a radiative damping time scale of ~38 days. A similar value was obtained for January in both 1977 and 1978.

Based upon a comparison of our results with those of Wiin-Nielsen and Brown (1962) and Brown (1964), it appears that the contribution to the destruction of eddy APE in midlatitudes during winter by radiational processes is significant for the ultralong waves, while destruction of eddy APE by heat flux from the earth's surface may be predominant at higher wavenumbers ($m \geq 3$). The role of latent heat release in midlatitude G_E is still an open question (Hayashi and Golder, 1981).

Acknowledgments. We would like to thank Professor Barry Saltzman and Professor Ronald Smith for useful discussions. This study was supported by the National Aeronautics and Space Administration under Grant NAS 8-34903 at Yale University.

REFERENCES

Brown, J. A., 1964: A diagnostic study of tropospheric diabatic heating and the generation of available potential energy. *Tellus*, **16**, 371–388.

Chen, T.-C., 1982: A further study of spectral energetics in the winter atmosphere. *Mon. Wea. Rev.*, **110**, 947–961.

Clapp, P. F., 1964: Global cloud cover for seasons using Tiros nephanalysis. *Mon. Wea. Rev.*, **92**, 495–507.

Cox, S. K., 1969: Radiation models of midlatitude synoptic features. *Mon. Wea. Rev.*, **97**, 637–651.

Dutton, J. A., and D. R. Johnson, 1967: The theory of available potential energy and a variational approach to atmospheric energetics. *Advances in Geophysics*, Vol. 12, Academic Press, 333–436.

Freeman, K. P., and K.-N. Liou, 1979: Climatic effects of cirrus clouds. *Advances in Geophysics*, Vol. 21, Academic Press, 231–287.

Geller, M. A., and S. K. Avery, 1978: Northern Hemisphere distributions of diabatic heating in the troposphere derived from general circulation data. *Mon. Wea. Rev.*, **106**, 629–636.

Gruber, A., and J. S. Winston, 1978: Earth-atmosphere radiative heating based on NOAA scanning radiometer measurements. *Bull. Amer. Meteor. Soc.*, **59**, 1570–1573.

Hayashi, Y., and I. Golder, 1981: The effects of condensational heating on mid-latitude transient waves in their mature stage: Control experiments with a GFDL general circulation model. *J. Atmos. Sci.*, **38**, 2532–2539.

Katayama, A., 1967: On the radiation budget of the troposphere over the Northern Hemisphere (III)—Zonal cross-sections and energy consideration. *J. Meteor. Soc. Japan*, **45**, 26–38.

Kuhn, P. M., and V. E. Suomi, 1960: Infrared radiometer soundings on a synoptic scale. *J. Geophys. Res.*, **65**, 3669–3677.

Lawniczak, G. E., Jr., 1969: On a multi-layer analysis of atmospheric diabatic processes and the generation of available potential energy. Ph.D. dissertation, University of Michigan, Ann Arbor, 111 pp.

Lorenz, E. N., 1955: Available potential energy and the maintenance of the general circulation. *Tellus*, **7**, 157–167.

Newell, R. E., J. W. Kidson, D. G. Vincent and G. J. Boer, 1974: *The General Circulation of the Tropical Atmosphere and Interactions with Extra-Tropical Latitudes, Vol. 2.* The MIT Press, 371 pp.

Ohring, G., and A. Gruber, 1983: Satellite radiation observations and climate theory. *Advances in Geophysics*, Vol. 25, Academic Press, 237–304.

Paltridge, G. W., and C. M. R. Platt, 1976: *Radiative Processes in Meteorology and Climatology.* Elsevier, 318 pp.

Sabatini, R. R., and V. E. Suomi, 1962: On the possibility of atmospheric infra-red cooling estimates from satellite observations. *J. Atmos. Sci.*, **19**, 349–350.

Saltzman, B., 1973: Parameterization of hemispheric heating and temperature variance fields in the lower troposphere. *Pure Appl. Geophys.*, **105**, 890–899.

Suomi, V. E., and W. C. Shen, 1963: Horizontal variation of infrared cooling and the generation of eddy available potential energy. *J. Atmos. Sci.*, **20**, 62–65.

Tomatsu, K., 1979: Spectral energetics of the troposphere and lower stratosphere. *Advances in Geophysics*, Vol. 21, Academic Press, 289–405.

Vincent, D. G., G. B. Pant and H. J. Edmon, Jr., 1977: Generation of available potential energy of an extratropical cyclone system. *Mon. Wea. Rev.*, **105**, 1252–1265.

Weinstein, M., and V. E. Suomi, 1961: Analysis of satellite infrared radiation measurement on a synoptic scale. *Mon. Wea. Rev.*, **89**, 419–428.

Wiin-Nielsen, A., 1968: On the intensity of the general circulation of the atmosphere. *Rev. Geophys.*, **6**, 559–579.

——, and J. A. Brown, 1962: On diagnostic computations of atmospheric heat sources and sinks and the generation of available potential energy. *Proc. Int. Symp. on Numerical Weather Prediction*, Tokyo, Meteor. Soc. Japan, 593–613.

——, A. Vernekar and C. H. Yang, 1967: On the development of baroclinic waves influenced by friction and heating. *Pure Appl. Geophys.*, **68**, 131–161.

Tellus (1984), *36A*, 52–63

A comparison of the spectral energy and enstrophy budgets of blocking versus nonblocking periods

By ANTHONY R. HANSEN, *Department of Geology and Geophysics, Yale University, P.O. Box 6666, New Haven, Connecticut 06511, U.S.A.* and ALFONSO SUTERA, *Center for the Environment and Man, Inc., Hartford, Connecticut 06230, U.S.A.*

(Manuscript received October 18, 1982; in final form March 7, 1983)

ABSTRACT

The time mean spectral energy and enstrophy budgets for blocking versus nonblocking periods from the winters of 1978–79 and 1976–77 are calculated. The major differences in the 1978–79 cases were in the nonlinear interaction terms. A pronounced upscale cascade of kinetic energy *and* enstrophy from intermediate to planetary-scale wavenumbers during blocking was found. During December 1976, the energy and enstrophy budgets of a case of Atlantic blocking were very similar to the cases in 1978–79, but quite different from the persistent, greatly amplified, planetary-wave pattern that followed in January and February 1977 (as identified by Charney et al., 1981). Planetary-scale baroclinic processes were greatly increased during the 1977 event along with reduced intermediate-scale baroclinic activity and the absence of the upscale enstrophy cascade noted in the other blocking cases.

The predictability time (Lilly, 1970) based on the enstrophy flux function showed an increased predictability for the January–February 1977 event but no significant differences between the other blocking cases compared to the nonblocking sample. However, the reversal of the low wavenumber enstrophy cascade during blocking does suggest that blocking may be more persistent (due to reduced dissipation of the large-scale circulation) and therefore more predictable.

1. Introduction

The term "blocking" has been used to describe a variety of circulation features with characteristic time scales larger than the synoptic time scale. The importance of blocking events in causing extremes in local surface weather and the expectation that the existence of these persistent features would allow greater forecasting skill in numerical weather prediction models has stimulated a great deal of interest in them in recent years.

Diagnostic calculations have usually identified blocking with large-scale baroclinic processes (e.g., Paulin, 1970; Murakami and Tomatsu, 1965). Recently, Hansen and Chen (1982) were able to identify the initiation of two cases of blocking with enhanced baroclinic energy conversions. In one case, intense baroclinic cyclone waves forced the development of a blocking high through nonlinear interactions. In the other case, large-scale baroclinic processes accompanied the block's development.

In the present study, we will attempt to identify any systematic differences in the time mean spectral energy and enstrophy budgets of blocking events compared to nonblocking periods using data from two recent winters (1976–77 and 1978–79). Recently, Bengtsson (1981) has shown from numerical simulations that during a blocking event the atmosphere is in general more predictable than during nonblocking periods.

We are interested to see whether any diagnostic evidence exists for the greater predictability of blocking found by Bengtsson. Although our sample

sizes are fairly small, several interesting features related to differences in the nonlinear interaction terms appear.

2. Procedures

2.1. *Data*

The data used in the study are the output of the twice daily operational analysis of the National Meteorological Center (NMC) from the winters (DJF) of 1976–77 and 1978–79. Data for the horizontal wind (u, v), geopotential height (z) and temperature (T) on a 2.5° × 2.5° grid at the ten mandatory levels in the troposphere (1000, 850, 700, 500, 400, 300, 250, 200, 150 and 100 mb) were used. Vertical velocities calculated from the quasi-geostrophic ω equation (assuming $\omega = 0$ at 1000 and 100 mb) were used in the energetics calculation (Chen *et al.*, 1981). Fourier coefficients of u, v, z, T and ω were computed for every 2.5° of latitude at the 10 levels with the wavenumber expansion of these variables truncated after zonal wavenumber 18.

During 1976–77, NMC employed the analysis scheme of Flattery (1971) in which only the rotational component of the wind is retained in u and v. In 1978–79, a multivariate, optimum interpolation analysis scheme was employed (Bergman, 1979). In this case a small divergent component of the horizontal wind is retained. However, the kinetic energy content of this divergent wind is quite small (Chen and Tribbia, 1981) and we do not feel that it will adversely affect the evaluation of the vorticity advection terms in the enstrophy budget calculation (see below).

2.2 *Analysis*

In the interest of brevity, the spectral energetics and spectral enstrophy equations will be presented in symbolic form only. The formulation of the spectral energetics equations can be found in Saltzman (1957, 1970) and the formulation of the spectral enstrophy equations can be found in Chen and Tribbia (1980). Note that derivation of the enstrophy equations requires that we assume the wind field to be nondivergent. The 1978–79 NMC wind field is not nondivergent, as mentioned earlier, but we feel the advection of vorticity by the divergent component of the wind will be small compared to advection by the rotational component and, therefore, the inclusion of a small divergent component in the horizontal wind will not affect our calculation.

The rates of change of wavenumber m kinetic energy (K_m), available potential energy (A_m) and enstrophy (E_m) are given by:

$$\frac{\delta}{\delta t} K_m = C(K_z, K_m) + C(A_m, K_m) + C_k(m|n, l) + B(K_m)$$

$$\frac{\delta}{\delta t} A_m = C(A_z, A_m) - C(A_m, K_m) + C_A(m|n, l) + G(A_m) + B(A_m)$$

and

$$\frac{\delta}{\delta t} E_m = C(E_z, E_m) + C_E(m|n, l) + \beta_m + G(E_m) + B(E_m).$$

Here, a z subscript denotes a zonal mean quantity

$$[()_z = \frac{1}{2\pi}\int_0^{2\pi} () \, d\lambda \quad \text{where } \lambda = \text{longitude}],$$

and an m subscript denotes a departure from this mean for wavenumber m. The notation $C(A, B)$ represents a conversion of energy (or enstrophy) from reservoir A to reservoir B. $C_X(m|n, l)$ denotes the rate of increase of the quantity X (where $X = K$, A or E) at wavenumber m due to nonlinear triad interactions with all possible combinations of wavenumbers n and l. β_m represents the so-called β-effect ($-\mathbf{v}\cdot\nabla f$) in the enstrophy budget. We were unable to calculate the generation terms ($G(A_m)$ and $G(E_m)$) with available data. $B(X)$ denotes boundary flux terms due to fluxes of X across both vertical and horizontal boundaries.

We integrated the budget equations over the region from 30° N to 80° N and from 1000 mb to 100 mb. When not integrated over the entire mass of atmosphere, the budget equations include certain horizontal and vertical flux terms (Saltzman, 1970; Chen and Tribbia, 1980). With our data, we were unable to calculate the vertical flux terms, although the vertical fluxes could in principle, be competitive with the other terms. The horizontal flux terms are frequently small (except the flux of geopotential energy) and differences in them between blocking and nonblocking situations were

usually not significant. Therefore, we will not discuss them.

2.3. *Selection of blocking days*

Traditionally, blocking has been identified subjectively according to certain kinematic properties of the flow as set down by Rex (1950). Recently, blocking events have been identified as persistent departures from the climatological mean height field (Dole, 1978; Charney et al., 1981). Our primary goal is to study persistent, large-scale blocking events compared to predominantly zonal circulations and to eliminate short duration (synoptic time scale), low amplitude, small-scale features from our sample of blocking observations. Therefore, we restrict ourselves to cases of stationary or slowly propagating ridges where the departure of the 500 mb height from the zonal mean, averaged over every 2.5° of latitude from 55°–80° N, exceeded 250 m for seven days or more. Blocking events so selected were compared with the twice-daily NMC 500 mb charts. The correspondence between the dates of blocking events identified subjectively from the charts and those determined from persistent height departures was quite good. Discrepancies of one or two observations (12–24 hours) at most occurred at the beginning and ending of the individual blocking events. Frequently, the two selections were identical. Therefore the blocking days identified from the height departures were used to form the sample of blocking and nonblocking days. Any observation not falling in a blocking period was included in the nonblocking sample. We should note that changing one or two observations at the beginning or ending of a given blocking event from the blocking sample to the nonblocking sample (or vice versa) did not significantly affect the mean energy and enstrophy budgets.

In addition, a case of very large negative height departures occurred during January and February 1977. This particular event has been discussed in a number of contexts by numerous other authors. Its existence is correlated with a simultaneous, very cold sea surface temperature anomaly in the North Pacific Ocean (Miyakoda and Rosati, 1982). Charney et al. (1981) provide the dates of the two periods during January and February 1977 of the largest negative height departures from the climatological mean. We will use their dates for the persistent low height anomalies in our diagnostic calculation. In fact, these low anomalies persisted throughout most of January and February 1977 (Chen and Shukla, 1983). Because of the existence of large amplitude features of one type or another throughout the 1976–77 winter, no nonblocking days from this winter were included in our nonblocking sample. A summary of the blocking and nonblocking days for the two winters is given in Table 1.

Our selection procedure is admittedly arbitrary but it does identify periods of large persistent height departures. The comparison of these periods with synoptic charts indicates that these periods satisfy (for the most part) the conventional, subjective definition of blocking. However, the inherent subjectivity in identifying what does or does not constitute blocking continues to be a problem in diagnostic studies of the phenomenon.

Table 1. *Tabulation of blocking and nonblocking days from the 1978–79 and 1976–77 winters determined from persistent height departures (see text). Dates for the negative height anomalies in January–February 1977 were determined by Charney et al. (1981) as extreme departures from the climatological mean height*

1978–79	
Blocking days (90 observations)	Nonblocking days (85 observations)
1. 0000 GMT 1 Dec.–1200 GMT 7 Dec.: Atlantic	0000 GMT 8 Dec.–1200 GMT 19 Dec.
2. 0000 GMT 20 Dec.–1200 GMT 27 Dec.: Atlantic	0000 GMT 28 Dec.–1200 GMT 28 Dec.
3. 1200 GMT 29 Dec.–0000 GMT 10 Jan.: Pacific	1200 GMT 10 Jan.–1200 GMT 13 Jan.
4. 0000 GMT 14 Jan.–1200 GMT 26 Jan.: Atlantic	0000 GMT 27 Jan.–1200 GMT 15 Feb.
5. 0000 GMT 16 Feb.–0000 GMT 22 Feb.: Atlantic	1200 GMT 22 Feb.–1200 GMT 28 Feb.
1976–77	
Blocking days (36 observations)	Charney et al. (1981) negative anomalies (76 observations)
1. 1200 GMT 11 Dec.–0000 GMT 29 Dec.: Atlantic	1. 30 December–17 January
	2. 2 February–22 February

3. Results

3.1. *1978–79 winter*

From December 1978 through February 1979, we identified five major blocking events, four over the Atlantic–European region and one over the North Pacific (Table 1). In general, the mean energy and enstrophy budgets of the Atlantic cases were similar to the Pacific case even though the initiation of the Pacific case was different from the late December 1978 case (Hansen and Chen, 1982). Whether or not the energetics of the Pacific case are typical of other Pacific blocking cases is unknown, although all the Atlantic events showed similar characteristics and were similar to the December 1976 case (see below). First, consider the average kinetic energy (K), enstrophy (E) and available potential energy (A) spectra (Fig. 1) of all five cases compared to the nonblocking days. In the mean, the kinetic energy in the longest waves

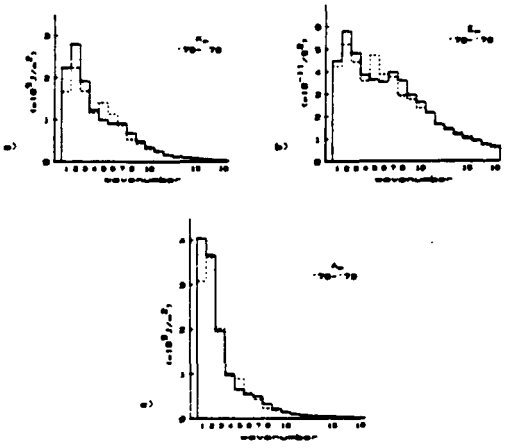

Fig. 1. Wavenumber spectra of (a) the kinetic energy, K_m; (b) the enstrophy, E_m; and (c) the available potential energy, A_m, for the 1978–79 winter. The solid line represents the mean spectra for all blocking days and the dashed line represents the nonblocking days.

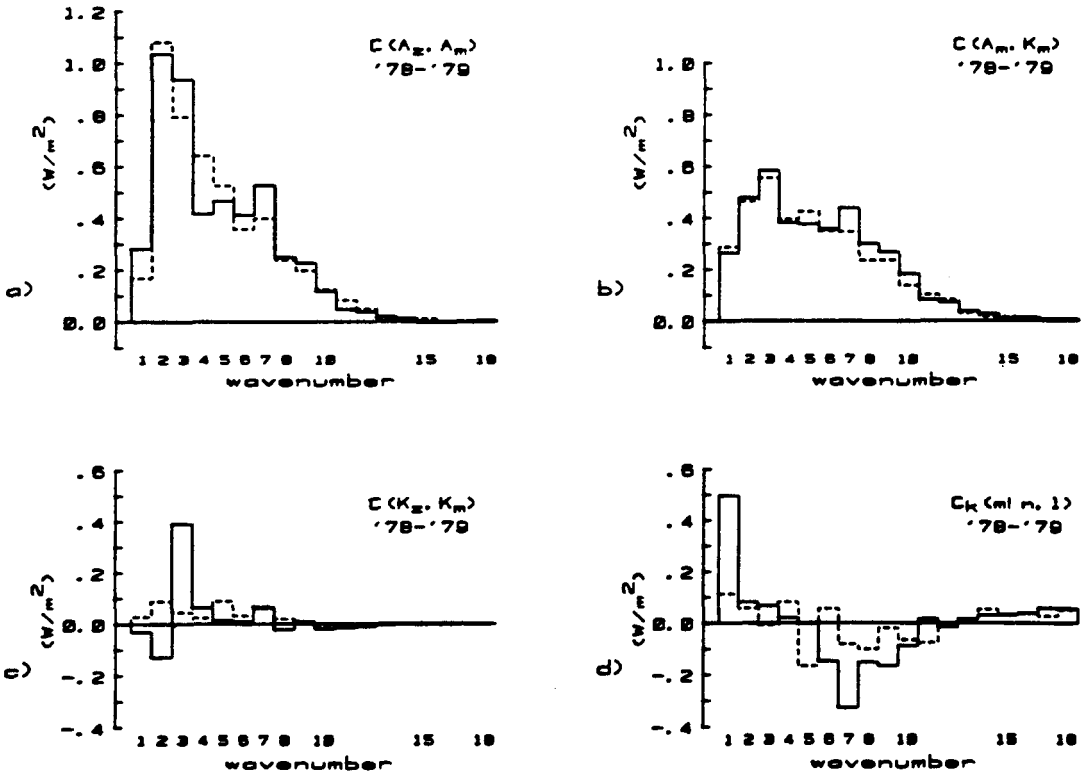

Fig. 2. 1978–79 energy budget terms: (a) $C(A_z, A_m)$; (b) $C(A_m, K_m)$; (c) $C(K_z, K_m)$; and (d) $C_k(m|n, l)$. As in Fig. 1, the solid line signifies the spectra for all blocking days and the dashed line denotes all nonblocking days. The notation is explained in the text.

(wavenumbers 1–3) is greater during blocking compared to the nonblocking sample, while the K content of the intermediate-scale wavenumbers is slightly lower during blocking. The enstrophy spectrum is qualitatively similar to the K spectrum at low wavenumbers but the total enstrophy in wavenumbers 5 through 10 is nearly the same for blocking and nonblocking. The A spectrum shows only an increase in available potential energy at wavenumber 1 for blocking and no other systematic differences.

The energy conversions $C(A_z, A_m)$ and $C(A_m, K_m)$ (Fig. 2a, b) are quite similar for the blocking and nonblocking samples. $C(A_z, A_m)$ shows slight increases at wavenumbers 1 and 3 during blocking with largely offsetting differences in wavenumbers 4 through 7. The increased conversion at wavenumbers 1 and 3 is totally absent when the four Atlantic cases are considered alone (not shown). The $C(A_m, K_m)$ spectrum is remarkably similar in the blocking and nonblocking situations although there are slightly larger conversions in wavenumbers 7 through 10 during blocking. $C(K_z, K_m)$ (Fig. 2c) indicates a large gain in wavenumber 3 kinetic energy due to mean flow interaction that is largely offset by reduced values at wavenumbers 1 and 2 when comparing blocking and nonblocking episodes.

The largest systematic differences between blocking and nonblocking appears in the nonlinear interaction term, $C_k(m|n, l)$ (Fig. 2d). The transfer of kinetic energy from intermediate-scale wavenumbers to the largest-scale wavenumbers takes

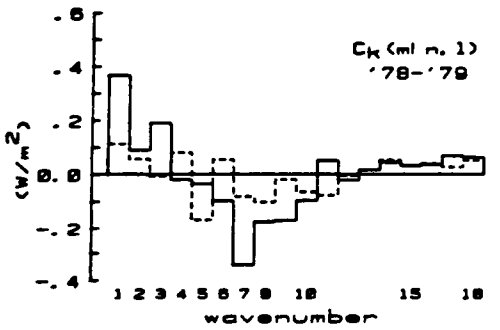

Fig. 3. $C_k(m|n, l)$ for the four Atlantic cases from 1978–79 (solid line) compared to all nonblocking days (dashed line).

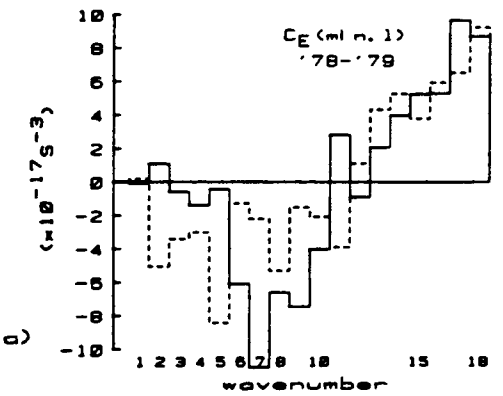

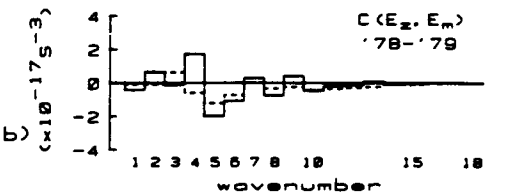

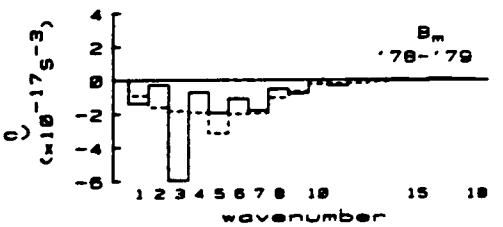

Fig. 4. The 1978–79 enstrophy budget terms: (a) $C_E(m|n, l)$; (b) $C(E_z, E_m)$; and (c) β_m, the rate of change of E_m due to the β effect. As in Fig. 1, the solid line represents all blocking days in the 1978–79 winter and the nonblocking results are represented by the dashed line.

place at a much greater rate during blocking periods compared to nonblocking, mostly into wavenumber 1. For the Atlantic cases alone (Fig. 3), both wavenumbers 1 and 3 benefit from the much increased kinetic energy export from wavenumbers 6 through 9 during blocking. $C_A(m|n, l)$ (not shown) is similar for the two samples and the most important boundary flux term was the horizontal flux of geopotential energy (not shown) which contributed more kinetic energy to wavenumber 1 during blocking with an offsetting loss at wavenumber 3.

The dominant term in the enstrophy budget (Fig. 4) is the nonlinear exchange term, $C_E(m|n, l)$. A very remarkable difference between blocking and nonblocking situations appears. Normally, enstrophy is cascaded from the longest waves into the shortest wavelengths (Steinberg et al., 1971). This characteristic also appears in our nonblocking sample (Fig. 4a, dashed line). However, during blocking, the net enstrophy cascade out of the longest waves (wavenumbers 1–5) disappears and a net gain of enstrophy appears at wavenumber 2. Meanwhile, the intermediate wavelengths (wavenumbers 6–10) are exporting a significantly larger amount of enstrophy than during nonblocked periods. For the Atlantic cases alone (not shown) there is an increase in enstrophy due to nonlinear interactions at both wavenumbers 2 and 3 during blocking. Thus during blocking the enstrophy cascade at low wavenumbers is *reversed*, as enstrophy is injected into the largest-scale waves by transient cyclone-scale waves. The only other difference in the enstrophy budgets is a greater loss of wavenumber 3 enstrophy due to the β effect during blocking.

The differences in the nonlinear interaction terms are easily seen by comparing the kinetic energy and enstrophy flux functions for our two samples. Following Steinberg et al. (1971), these functions can be defined as

$$\frac{\delta F_k}{\delta m} = -C_k(m|n, l)$$

and

$$\frac{\delta F_E}{\delta m} = -C_E(m|n, l)$$

assuming $F_K(0) = F_E(0) = 0$. Regions of the appropriate flux function with negative slopes represent wavenumber bands gaining K or E through nonlinear interactions. Regions with positive slopes are losing energy or enstrophy. The absence of an enstrophy flux out of the lowest wavenumbers during blocking and the change in the sign of the enstrophy flux function near wavenumber 2 is evident in Fig. 5a. The much larger flux of kinetic energy into the long waves during blocking can clearly be seen in Fig. 5b. The flux functions for the Atlantic cases alone are essentially the same as those shown in Fig. 5.

3.2. *1976–77 winter*

A comparison between the energy and enstrophy budgets of the December 1976 case of Atlantic blocking and the persistent, large amplitude low anomalies during January and Feb-

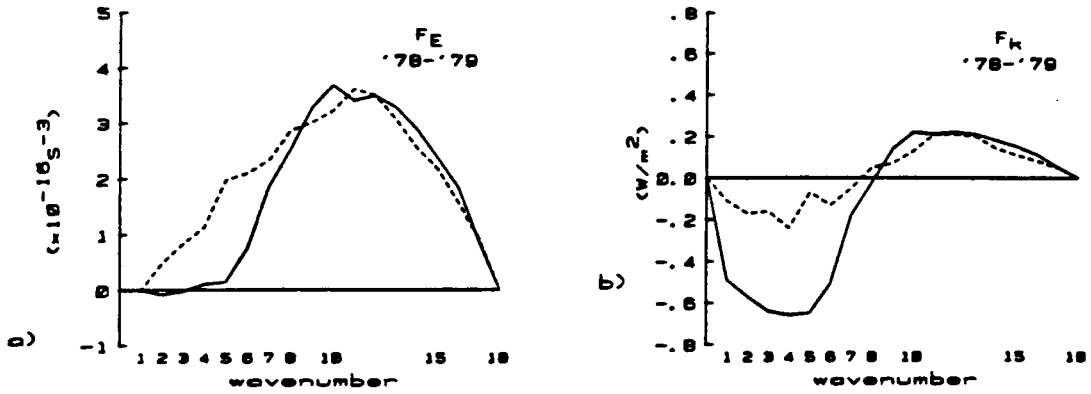

Fig. 5. The nonlinear flux functions and (a) enstrophy, F_E, and (b) kinetic energy, F_k, for blocking (solid line) and nonblocking (dashed line) for the 1978–79 winter.

ruary 1977 are given in Figs. 6–8. In general, the December 1976 event showed relatively weak large-scale (low wavenumber) baroclinic processes compared to January–February 1977 (Fig. 7a, b) (or the 1978–79 nonblocking sample), but it does exhibit the same enhanced upscale kinetic energy flux as the 1978–79 blocking cases (Fig. 7d), and a very striking reversal of the low wavenumber enstrophy cascade (Fig. 8a) at wavenumber 2. The similarity in the behavior of Rex-type blocking in two different winters lends support to the significance of this result.

However, comparing the December 1976 event to the January and February 1977 events indicates remarkable changes in the circulation between December 1976 and the following two months. There was a remarkable increase in $C(A_z, A_m)$ and $C(A_m, K_m)$ at wavenumbers 2 and 3 during January–February 1977 (Fig. 7a, b). This characteristic was also noted by Chen and Shukla (1983) but is even more striking when compared to the December 1976 statistics. There is also a larger net gain at low wavenumbers in K_m due to $C(K_z, K_m)$ in January–February 1977 (Fig. 7c). The impression given by these results is that planetary-scale baroclinic and barotropic processes were of dominant importance in the January–February 1977 case as opposed to the case for Rex-type blocking. The nonlinear, wave–wave interactions during January–February 1977 were dominated by large energy gains for wavenumbers 1, 3 and 4 and a large loss from wavenumber 2. The kinetic energy transfer out of the intermediate-scale waves was relatively small.

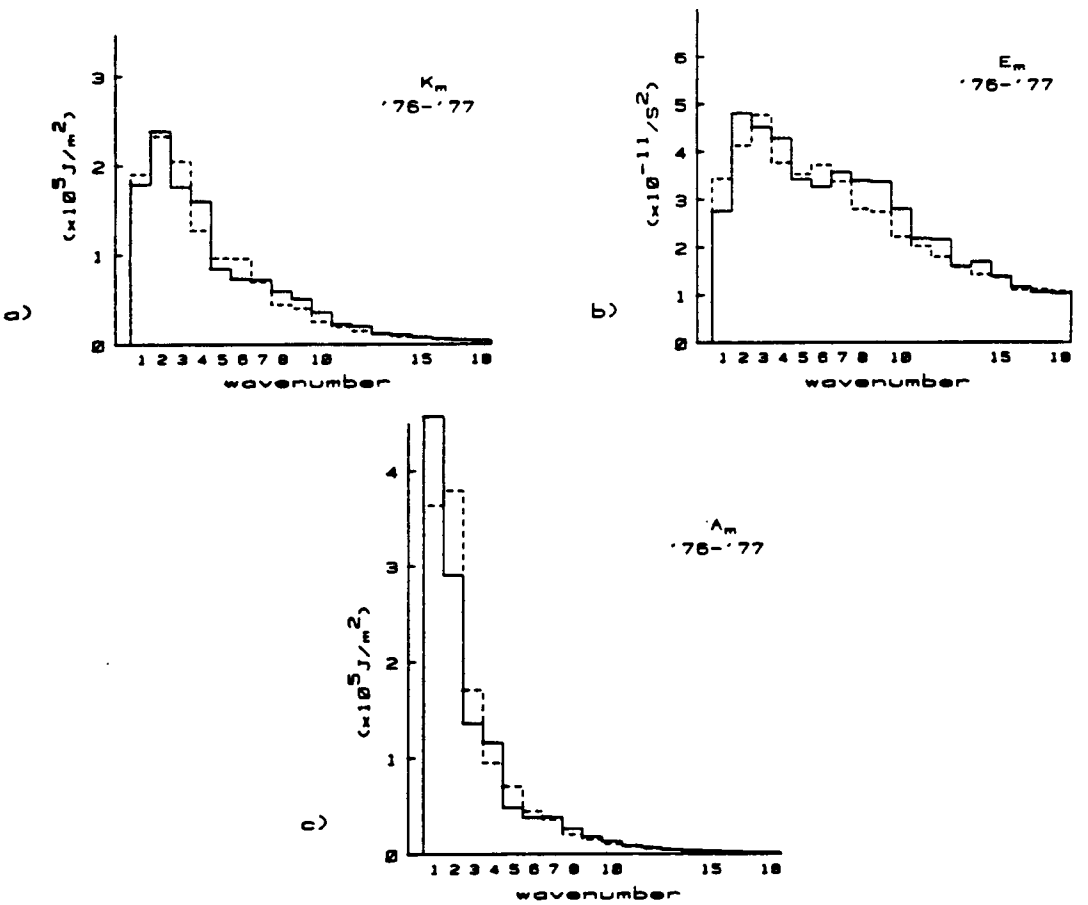

Fig. 6. Wavenumber spectra of (a) K_m; (b) E_m; and (c) A_m for the 1976–77 winter. Here the solid line signifies the December 1976 Atlantic blocking case and the dashed line represents the periods of large negative height anomalies in January and February 1977.

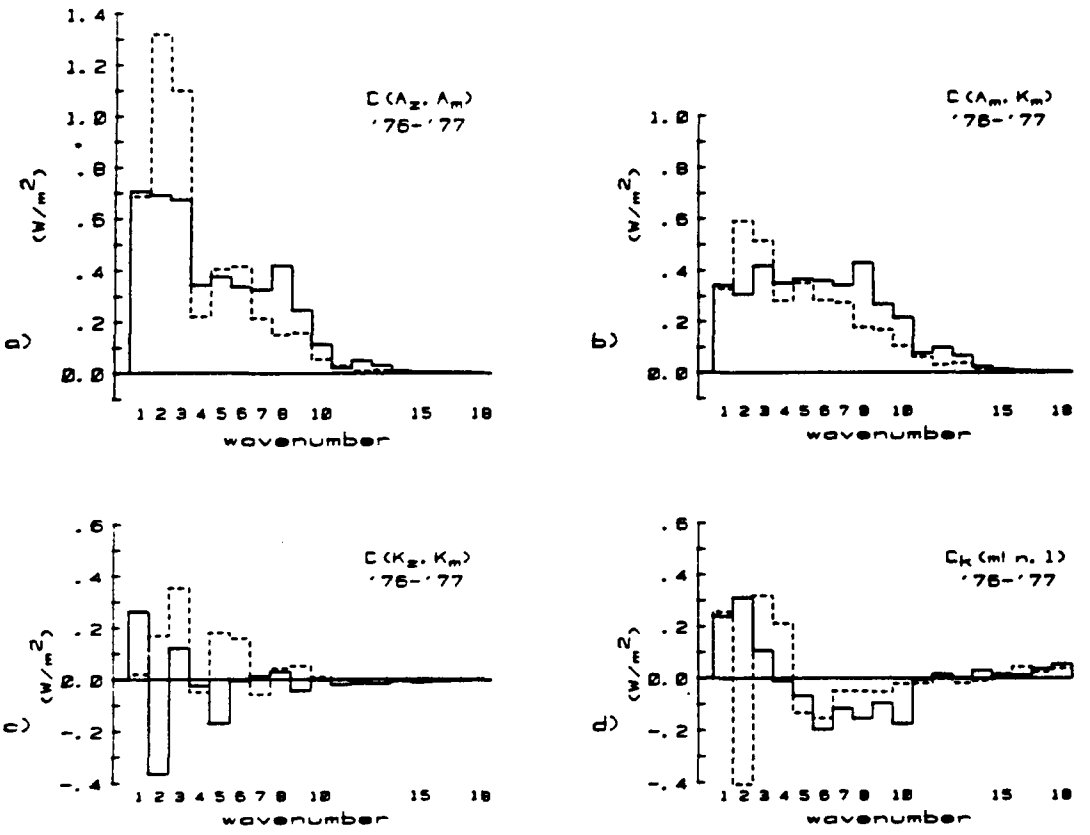

Fig. 7. (a) $C(A_z, A_m)$; (b) $C(A_m, K_m)$; (c) $C(K_z, K_m)$; and (d) $C_k(m|n, l)$ for the 1976–77 winter. As in Fig. 6, the solid line represents the December 1976 blocking case and the January–February 1977 negative anomalies energetics are represented by the dashed line.

This is consistent with the reduced intermediate-scale baroclinic activity [$C(A_z, A_m)$ and $C(A_m, K_m)$ at wavenumbers 7–10 and 6–10, respectively (Fig. 7a, b)] during January–February 1977.

The nonlinear enstrophy exchange, $C_E(m|n, l)$ (Fig. 8a), for the December 1976 case is similar to the 1978–79 cases as noted above (e.g., reversal of cascade at low wavenumbers and increased export of enstrophy from intermediate-scale wavenumbers), but the January–February 1977 enstrophy exchange is more like the 1978–79 nonblocking sample. These qualitative features carry over to the enstrophy and energy flux functions (Fig. 9). Notice the very striking reversal in the enstrophy flux function at low wavenumbers for the December 1976 case (Fig. 9a). Also notice the much lower value of the enstrophy flux function for the January–February 1977 case in a nearly constant range from roughly wavenumbers 8 to 15. The enstrophy flux function in the same range for the December 1976 blocking case is virtually identical to the 1978–79 blocking and nonblocking samples.

3.3. *Predictability question*

The rate of error growth in numerical weather prediction models due to small-scale inaccuracies in the initialization can be related to the rate of down-scale enstrophy cascade in a constant enstrophy flux inertial subrange of a two-dimensional turbulent fluid (Leith and Kraichman, 1972). The characteristic time of this process can be called the predictability time and is inversely proportional to the cube root of the constant rate of enstrophy transfer to higher wavenumbers in a constant

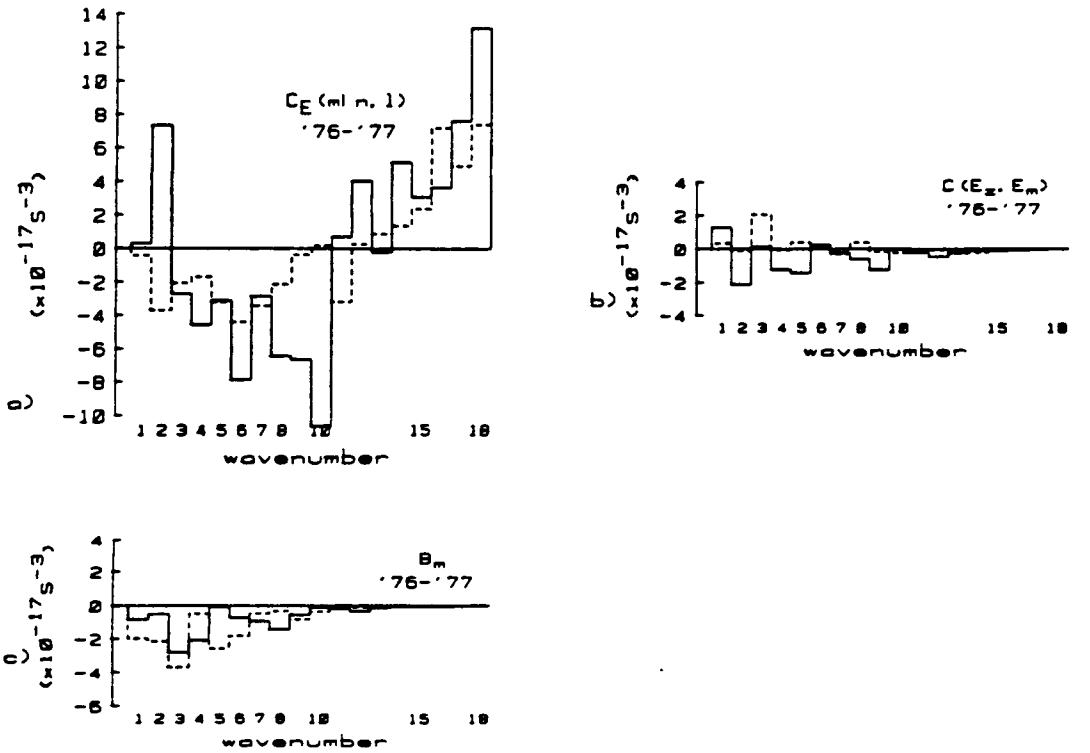

Fig. 8. The 1976–77 enstrophy budget terms: (a) $C_E(m|n, l)$; (b) $C(E_z, E_m)$; and (c) β_m for the December 1976 blocking case (solid line) and the January–February 1977 negative anomaly cases (dashed line).

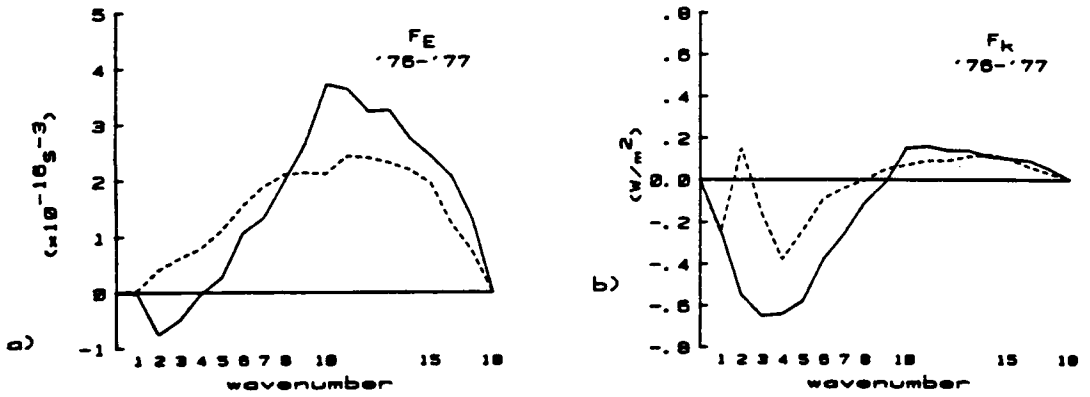

Fig. 9. The nonlinear flux functions for (a) enstrophy and (b) kinetic energy for the December 1976 blocking case (solid line) and the January–February 1977 negative anomalies (dashed line).

enstrophy flux inertial subrange (Lilly, 1970; Leith and Kraichnan, 1972). Although efforts to find observational evidence of a two-dimensional turbulent subrange in the atmosphere have been inconclusive (Chen and Wiin-Nielsen, 1978; Lambert, 1981), the fact that the atmosphere at the larger scales behaves predominantly like a two-dimensional fluid in which the kinetic energy spectrum obeys a -3 power law (Chen and Tribbia, 1981; Julian et al., 1970; Wiin-Nielsen,

1967) suggests that a qualitative estimate of the predictability time for blocking compared to nonblocking situations based on the enstrophy flux function may be made. The estimate can only be done in a qualitative way because the numerical value of the enstrophy flux function, F_E, in the constant range is dependent upon the truncation used (Steinberg et al., 1971). The reason for this sensitivity is readily apparent from inspection of the enstrophy spectra (Fig. 1b or Fig. 6b). A finite amount of enstrophy is lost when the wavenumber expansion of the wind field is truncated at wavenumber 18. This will cause aliasing problems in the nonlinear enstrophy interaction in our truncated data set that will cause changes in the shape of the enstrophy flux function at high wavenumbers. Unfortunately, the accuracy of our data at wavenumbers higher than 18 is poor so this problem cannot be alleviated. However, we will assume the values of the flux function that we have are qualitatively correct for comparison purposes.

As noted earlier, the enstrophy flux function in the constant range is nearly identical in both blocking and nonblocking situations [Figs. 5a and 9a] suggesting no greater predictability for blocking. However, the January–February 1977 event, which was characterized by enhanced large-scale baroclinic processes, exhibited a roughly 1/3 smaller enstrophy flux rate (Fig. 9a, dashed line). This result allows us to speculate that the persistent low anomalies in 1977 were inherently more predictable than either the nonblocking or Rex-blocking cases.

An explanation of the greater predictability of the Rex-type blocking found by Bengtsson (1981) might be found in the reversal of low wavenumber enstrophy cascade (especially near wavenumber 2), and the absence of an enstrophy cascade out of the lowest 5 wavenumbers during blocking (Figs. 5a and 8a) as opposed to the normal case (Fig. 5a (dashed line) and Steinberg et al., 1971). This may indicate that the destruction of large-scale vorticity by down-scale cascade and eventual dissipation is greatly reduced or eliminated during blocking events. As a result, blocking patterns may be more persistent and therefore more predictable.

We should re-emphasize that the source of the enstrophy being cascaded into the low wavenumbers is the intermediate-scale wavenumbers. The fact that the predictability time for blocking is the same as for nonblocking may indicate that blocking is no more predictable in the traditional sense than the cyclones that successively regenerate it.

4. Concluding remarks

To summarize, the most noteworthy differences between the spectral energy and enstrophy budgets of blocking versus nonblocking periods are in the nonlinear interaction terms. Apparently, when the ultralong waves have a large amplitude, such as during Rex-type blocking, they are able to more efficiently gain kinetic energy from the cyclone scale waves through wave–wave interactions. In addition, through a reversal of the low wavenumber enstrophy cascade, the ultralong waves are also able to gain enstrophy from the intermediate-scale waves during blocking, whereas the ultralong waves lose enstrophy through wave–wave interactions in nonblocked circumstances. The absence of enhanced large-scale baroclinic processes during the 1978–79 and December 1976 Rex-type blocking events does not augur well for the applicability to these cases of the various baroclinic blocking theories proposed recently.

The fact that the energy and enstrophy budgets for Rex-type blocking were similar in the two winters studied suggests that our findings are typical. However, our results for changes in the nonlinear interaction terms should be tested with a larger data set. This calculation is currently in progress.

The January–February 1977 negative height anomaly case presents a different class of phenomenon in which low wavenumber baroclinic energy conversions maintain the large amplitude features of the circulation and in which a significantly lower enstrophy flux function suggests greater predictability. This is in direct contrast to the Rex-type blocking cases which show no greater predictability in the traditional sense compared to nonblocking. However, the reversal of the low wavenumber enstrophy cascade does suggest a reduction in the dissipation of the low wavenumber enstrophy (assuming the atmosphere behaves like a two-dimensional turbulent fluid) and therefore greater persistence (and predictability) of the blocking pattern. In addition, the enstrophy cascade reversal may be an indication of intermittent behavior (Batchelor, 1960) in the large-scale flow

requiring no particular low wavenumber instability. (This aspect will be discussed further in a forthcoming paper.) If so, a description of blocking in terms of vortex dynamics (Batchelor, 1960; Onsager, 1949) may be useful. This possibility is being studied further.

From our results it appears that cyclone-scale waves play an important role in maintaining quasistationary blocking patterns by injecting enstrophy and kinetic energy into the large-scale flow. Bengtsson (1981) has also noted the apparent importance of transient smaller-scale waves in one case of blocking during January, 1979. Saltzman (1959) first suggested that nonlinear kinetic energy transfer from transient cyclone-scale eddies acts to maintain the quasistationary centers of action. Holopainen and Oort (1981) have suggested that in extratropical latitudes transient eddies act to maintain the enstrophy of the standing waves although more recent work disputes the earlier result (Holopainen et al., 1982). The role of transient eddies in maintaining quasistationary features of the circulation deserves further study. Also, it would appear that theoretical models of blocking should incorporate the effects of transient eddies.

5. Acknowledgements

We would like to thank Professor B. Saltzman, Dr. G. D. Robinson, and Professor M. Ghil for their comments and suggestions. This study was supported by the National Aeronautics and Space Administration under grant NAS8—34903 at Yale University and by the National Science Foundation under grant ATM81—06034 at the Center for the Environment and Man, Inc. Computations were performed at the National Center for Atmospheric Research which is supported by the National Science Foundation.

REFERENCES

Batchelor, G. K. (1960). *The theory of homogeneous turbulence*. Cambridge: Cambridge University Press.

Bengtsson, L. 1981. Numerical prediction of atmospheric blocking—A case study. *Tellus 33*, 19–42.

Bergman, K. 1979. Multivariate analysis of temperature and winds using optimum interpolation. *Mon. Wea. Rev. 107*, 1423–1444.

Charney, J. G., Shukla, J. and Mo, K. C. 1981. Comparison of a barotropic blocking theory with observation. *J. Atmos. Sci. 38*, 762–779.

Chen, T.-C. and Wiin-Nielsen, A. 1978. On nonlinear cascades of atmospheric energy and enstrophy in a two-dimensional spectral index. *Tellus 30*, 313–322.

Chen, T.-C. and Tribbia, J. J. 1980. On nonlinear cascades of enstrophy over the tropics at 200 mb during two northern hemisphere summers. *Mon. Wea. Rev. 108*, 913–921.

Chen, T.-C., Hansen, A. R. and Tribbia, J. J. 1981. A note on the release of available potential energy. *J. Meteorol. Soc. Japan 59*, 355–359.

Chen, T.-C. and Tribbia, J. J. 1981. Kinetic energy spectra of divergent wind in the atmosphere. *Tellus 33*, 102–104.

Chen, T.-C. and Shukla, J. 1983. Diagnostic analysis and spectral energetics of a blocking event in the GLAS climate model simulation. *Mon. Wea. Rev. 111*, 3–22.

Dole, R. M. 1978. The objective representation of blocking patterns. In *The general circulation: Theory, modeling and observations*. Notes from a Colloquium, Summer, 1978. NCAR/CQ-6 + 1978-ASP, 406–426.

Flattery, T. W. 1971. Spectral models for global analysis and forecasting. *Proceedings of the Sixth A.M.S. Technical Exchange Conference*, U.S. Naval Academy, 21–24 September, 1970. Air Weather Service Tech. Rep. 242.

Hansen, A. R. and Chen, T.-C. 1982. A spectral energetics analysis of atmospheric blocking. *Mon. Wea. Rev. 110*, 1146–1165.

Holopainen, E. O. and Oort, A. H. 1981. On the role of large-scale transient eddies in the maintenance of the vorticity and enstrophy of the time-mean atmospheric flow. *J. Atmos. Sci. 38*, 270–280.

Holopainen, E. O., Rontu, L. and Lau, N.-C. 1982. The effect of large-scale transient eddies on the time-mean flow in the atmosphere. *J. Atmos. Sci. 39*, 1972–1984.

Julian, P. R., Washington, W. M., Hembree, L. and Ridley, C. 1970. On the spectral distribution of large-scale atmospheric energy. *J. Atmos. Sci. 27*, 376–387.

Lambert, S. J. 1981. A diagnostic study of global energy and enstrophy fluxes and spectra. *Tellus 33*, 411–414.

Leith, C. E. and Kraichnan, R. H. 1972. Predictability of turbulent flows. *J. Atmos. Sci. 29*, 1041–1058.

Lilly, D. K. 1970. Lectures in sub-synoptic scales of motions and two-dimensional turbulence. In *Dynamic meteorology* (ed. P. Morel). Dordrecht/Holland: D. Reidel Publ. Comp., 353–418.

Miyakoda, K. and Rosati, A. 1982. The variation of sea surface temperature in 1976 and 1977. 1: The data analysis. *J. Geophys. Res. 87*, 5667–5680.

Reprinted from JOURNAL OF THE ATMOSPHERIC SCIENCES, Vol. 43, No. 5, 1 March 1986
American Meteorological Society

Circulation Regime-Dependent Nonlinear Interactions during Northern Hemisphere Winter

PHILIP S. BROWN, JR. , ANTHONY R. HANSEN AND JOSEPH P. PANDOLFO

Circulation Regime-Dependent Nonlinear Interactions during Northern Hemisphere Winter

PHILIP S. BROWN, JR.*, ANTHONY R. HANSEN** AND JOSEPH P. PANDOLFO*

*The Center for the Environment and Man, Inc., West Hartford, CT 06117
**Meteorology Research Center, Control Data Corporation, Minneapolis, MN 55440

(Manuscript received 29 April 1985, in final form 27 September 1985)

ABSTRACT

Average statistics for periods of large positive 500 mb height anomalies are compared to statistics for all other situations using NMC data for the 15 Januaries from 1963 to 1977. The 500 mb heights and geostrophic streamfunctions are represented as surface spherical harmonics, and energy and enstrophy spectra along with nonlinear wave–wave interaction statistics are computed.

Differences in 500 mb geopotential height variance, kinetic energy and enstrophy spectra occur between large positive anomaly events and other days in the two-dimensional spectral index band from roughly $n = 6$ to $n = 9$, where n is the degree of the associated Legendre function. The same index band experiences a reversal of both the usual kinetic energy and enstrophy cascades during large positive anomaly events. That is, the $6 \leq n \leq 9$ band gains energy and enstrophy from wave–wave interactions during the anomaly events and loses energy and enstrophy by the same process at other times. The source of this energy and enstrophy is higher index (smaller two-dimensional scale) waves. The indication is that the Atlantic cases are more subject to this cascade reversal than are Pacific events.

Our results suggest that the smaller scale, transient eddies may play a regime-dependent role in interactions with atmospheric circulation modes on the scale of the persistent anomalies. When interacting with larger-scale features, the role of smaller-scale transients may not always be dissipative.

1. Introduction

Studies of the interaction between transient eddies and the climatological-mean stationary flow indicate that although the enstrophy budget of stationary waves in midlatitudes appears to be maintained in part by the transient eddies (Holopainen and Oort, 1981), the effect of transient eddy heat transports overwhelms the vorticity transports in a potential vorticity budget, giving an overall dissipative role to the transients when interacting with the time mean flow (Youngblut and Sasamori, 1980; Holopainen et al., 1982). Further study has revealed that the long period transients (periods of 10 to 90 days) make a stronger contribution to this dissipative effect than do synoptic-scale (2.5 to 6 day period) transients (Lau and Holopainen, 1984). Van den Dool (1983), on the other hand, infers a potentially large role for high frequency transients in forcing monthly mean *anomalies*.

Theoretical studies have indicated that the large-scale wave pattern can act to modulate synoptic-scale baroclinic activity (Fredrickson, 1979) and that synoptic-scale transients can play an important role in maintaining equilibrium states, or "weather regimes", in certain models (Reinhold and Pierrehumbert, 1982; Kallen, 1981, 1982). In the present study, we will use observational data to examine whether the interaction between different scales of motion in a spherical harmonic framework is dependent upon the circulation regime characterizing the large-scale pattern. We use the large positive height anomaly events identified by Charney et al. (1981) to stratify the data in the 15 Januaries from 1963 to 1977. Statistically significant differences in the energy and enstrophy spectra as well as in the nonlinear wave–wave interactions are found.

Baer (1972) suggested that the degree of the Legendre function in a spherical harmonic representation of the data is the appropriate index to use when studying atmospheric spectra. Observational studies of nonlinear exchanges using this two-dimensional index have been made by Chen and Wiin-Nielsen (1978), Lambert (1981), and Boer and Shepherd (1983). Mean cascading during winter as calculated by Chen and Wiin-Nielsen, for example, shows that for $n = 1$ to 7 and $n = 19$ to 31, kinetic energy is gained through nonlinear interaction, with this energy being supplied by the modes with $n = 8$ to 18. In the enstrophy budget, modes with $n = 1$ to 7 gain a very small amount of enstrophy while a large loss of enstrophy from the range $n = 8$ to 18 is balanced by gains of higher index modes. The physical explanation of the occurrence of these wave–wave interactions in the atmosphere is that the dissipation of kinetic energy and enstrophy takes place in different wavenumber bands from where these quantities are generated. In the present study, a dataset spanning a longer time period than those considered in earlier

studies is used and attention is focused on interactions near the low wavenumber end of the spectrum.

First, we illustrate the differences in the height variance, kinetic energy, and enstrophy spectra of the large positive anomaly events (LPAs) compared to more normal circulations. The changes occur primarily in the spectral index band from $n = 6$ to 9. Guided by these results, we explore systematic differences in the nonlinear cascading. We find an apparently regime-dependent role of the smaller scale transient eddies when interacting with the spectral band that distinguishes the LPAs.

2. Data

The basic data used in this study are 500 mb geopotential heights from the NMC final analyses. For each January day in the years 1963–77, daily values of the geostrophic stream function are computed. By using January data only, we hope to avoid any complications due to the seasonal cycle. We present results for the 500 mb surface only because these results may be considered representative of the vertical average in the energy and enstrophy budgets. (Qualitatively similar results were obtained using 300 mb data.)

To perform the required spherical harmonic analyses, data are required over the entire sphere. The NMC grid, however, extends only from 90°N to about 15°N. Data must be extrapolated to fill the region from 15°N to the equator about which a symmetry assumption can be made to account for the Southern Hemisphere. In order to generate the required data, Ellsaesser's (1966) technique has been adopted. To construct values in the north equatorial region, data lying within the NMC octagon are used to extrapolate southward along the meridians using a linear function of $\sin(2\phi)$ as an extrapolation profile (ϕ = latitude). Even symmetry of the geopotential height about the equator is then assumed.

The fictitious data, of course, affect the spectral coefficients. Nevertheless, we would not expect the introduction of such data to keep us from our main objective of identifying essential differences between spectra for different periods as long as the manufactured data are based on reasonable, though crude, physical assumptions. Comparison of our results obtained in this way to those of Boer and Shepherd (1983) in which global data were used reveals quite similar results. Therefore, we do not expect the treatment of the tropics in the present study to dramatically affect the results.

In order to define periods of large positive anomaly events, we have adopted the criterion of Charney et al. (1981). In their work, time–longitude cross sections of departures of 500 mb heights from their climatological mean values at 50°N were examined for the 15 winter seasons that include the January months selected for this study. A period was designated as a large positive anomaly event if at any point on the 50°N latitude circle a positive anomaly of 200 gpm or more persists for 7 days or more. Some subjectivity was introduced in determining the beginning and end of each event (Charney et al., 1981). Table 1 lists the periods considered to be LPAs. The letter A, P or B in this table indicates whether the largest amplitude ridge occurred over the Atlantic or Europe (A), the Pacific Basin (P), or whether comparable amplitude ridges occurred over both oceans (B). Events listed of less than 7 day duration spanned the beginning or ending of the month in question. Note that the existence of a large positive height anomaly doesn't necessarily imply that a greater height variance overall will exist at any particular location or for any particular wavenumber (e.g., see the discussion in Charney et al., 1981).

Of the 465 days included in our analysis, there were 154 LPA days and 311 "normal" days according to the criterion used. A comparison of the characteristics of blocking and nonblocking days determined from purely subjective review of individual twice-daily weather charts for the 15 months in question yielded generally similar results to those from the objectively chosen LPA cases. However, our purpose is to compare diagnostic statistics from time periods characterized by persistent circulation anomalies to statistics from time periods in which such features were lacking. The relationship of LPAs to blocking is outside the scope of the present study.

3. Analysis

We compute a streamfunction ψ from the geostrophic balance equation:

$$f\nabla^2\psi + \nabla f\cdot\nabla\psi = g\nabla^2 z \qquad (1)$$

where f is the Coriolis parameter, g the acceleration of gravity, and z the height of the constant pressure surface. For the nondivergent component of the flow, the kinetic energy (K) and enstrophy (E) can then be written as

TABLE 1. January days (1963–77) on which LPA events took place.

1	8–21 January 1963 (P)
2	22–29 January 1963 (B)
3	30–31 January 1963 (P)
4	1–6 January 1965 (P)
5	1 January 1966 (P)
6	5–14 January 1967 (A)
7	1–5 January 1968 (B)
8	6–31 January 1968 (A)
9	1–2 January 1969 (B)
10	3–14 January 1969 (P)
11	11–25 January 1970 (A)
12	7–13 January 1971 (B)
13	15–31 January 1971 (P)
14	3–9 January 1973 (A)
15	1–10 January 1974 (P)
16	27–31 January 1975 (P)
17	6–12 January 1977 (A)

$$K = \frac{1}{4\pi}\int_{-1}^{1}\int_{0}^{2\pi}\frac{1}{2}\nabla\psi\cdot\nabla\psi d\lambda d\mu$$

$$= \frac{1}{4\pi}\int_{-1}^{1}\int_{0}^{2\pi} -\frac{1}{2}\psi\zeta d\lambda d\mu \quad (2)$$

$$E = \frac{1}{4\pi}\int_{-1}^{1}\int_{0}^{2\pi} -\frac{1}{2}\zeta^2 d\lambda d\mu \quad (3)$$

where $\mu = \sin\phi$ and ϕ is latitude. Other notation is conventional.

On a sphere, any real-valued function such as ψ can be written formally as a series of surface spherical harmonics in the form

$$\psi(\lambda, \mu) = \sum_{m=0}^{\infty}\sum_{n=m}^{\infty}(A_n^m \cos m\lambda + B_n^m \sin m\lambda)P_n^m(\mu) \quad (4)$$

where $P_n^m(\mu)$ is the associated Legendre function. The series is uniformly convergent (hence term-by-term differentiable) provided that it has continuous second derivatives over the whole sphere (Hobson, 1931, p. 602). Using the orthogonality properties of the Legendre functions, the coefficients A_n^m and B_n^m can be obtained from

$$\begin{Bmatrix} A_n^m \\ B_n^m \end{Bmatrix} = \frac{\delta_m}{2\pi}\int_{-1}^{1}\int_{0}^{2\pi}\psi(\lambda, \mu)\begin{Bmatrix}\cos m\lambda \\ \sin m\lambda\end{Bmatrix}P_n^m(\mu)d\lambda d\mu \quad (5)$$

where $\delta_m = 1$ for $m = 0$, and $\delta_m = 2$ for $m \neq 0$.

Series differentiability is an important consideration since we are to examine spectra obtained by application of various differential operators to series representations of the streamfunction. In particular, since $\zeta = \nabla^2\psi$, differentiability of (4) allows us to express the vorticity as

$$\zeta(\lambda, \mu) = \sum_{m=0}^{\infty}\sum_{n=m}^{\infty} -\frac{n(n+1)}{a^2}(A_n^m \cos m\lambda + B_n^m \sin m\lambda)P_n^m(\mu) \quad (6)$$

where a is the earth's radius.

The kinetic energy and enstrophy can then be written in series form as

$$K = \sum_{n=0}^{\infty}K_n = \sum_{n=0}^{\infty}\sum_{m=0}^{n}\frac{n(n+1)}{2a^2}\delta_m[(A_n^m)^2 + (B_n^m)^2] \quad (7)$$

$$E = \sum_{n=0}^{\infty}E_n = \sum_{n=0}^{\infty}\sum_{m=0}^{n}\frac{n^2(n+1)^2}{2a^4}\delta_m[(A_n^m)^2 + (B_n^m)^2]. \quad (8)$$

Equations governing the complete spectral energy and enstrophy budgets of the atmosphere can be obtained by differentiating (2) and (3) with respect to time and substituting from the vorticity equation. The appropriate vorticity equation for the atmosphere includes generation and dissipation terms as well as terms representing the advection of relative and planetary vorticity. It isn't possible to reliably estimate the former two terms with the available data so we will focus attention on the barotropic terms we can compute. Therefore, we won't present complete budget statistics but will emphasize a particular aspect of the problem, namely barotropic, nonlinear effects. The nondivergent, adiabatic, frictionless form of the vorticity equation may be written as

$$\frac{\partial\zeta}{\partial t} = -J(\psi, \zeta) - \frac{2\Omega}{a^2}\frac{\partial\psi}{\partial\lambda}, \quad (9)$$

where J denotes the Jacobian

$$J(\psi, \zeta) = \frac{1}{a^2}\left(\frac{\partial\psi}{\partial\mu}\frac{\partial\zeta}{\partial\lambda} - \frac{\partial\psi}{\partial\lambda}\frac{\partial\zeta}{\partial\mu}\right). \quad (10)$$

We can obtain simplified spectral forms of the kinetic energy and enstrophy budget equations by differentiating (2) and (3) with respect to time and using (4), (6) and (9). In particular, the derivatives of K and E can be represented as functions of n as:

$$\frac{dK_n}{dt} = I_n = \sum_{m=0}^{n} I_n^m = \sum_{m=0}^{n}\frac{1}{2}\delta_m(A_n^m q_n^m + B_n^m r_n^m). \quad (11)$$

$$\frac{dE_n}{dt} = J_n = \sum_{m=0}^{n} J_n^m = \sum_{m=0}^{n}\frac{1}{2}\frac{n(n+1)}{a^2}\delta_m(A_n^m q_n^m + B_n^m r_n^m). \quad (12)$$

Here, q_n^m and r_n^m are the amplitudes of the cosine and sine components of the harmonic expansion of $J(\psi, \zeta)$. That is,

$$\begin{Bmatrix} q_n^m \\ r_n^m \end{Bmatrix} = \frac{1}{4\pi}\int_{-1}^{1}\int_{0}^{2\pi}J(\psi, \zeta)\begin{Bmatrix}\cos m\lambda \\ \sin m\lambda\end{Bmatrix}P_n^m(\mu)d\lambda d\mu; \quad (13)$$

I_n^m and J_n^m measure the rate of gain (loss) of kinetic energy and enstrophy respectively in component (n, m) that results from a corresponding rate of loss (gain) in the remainder of the spectrum. The change in total kinetic energy or enstrophy due to wave–wave interactions is zero. Computational considerations related to calculating these spectra and nonlinear transfers are discussed in the Appendix.

As noted earlier, for a less approximate form of the vorticity equation, (11) and (12) would also contain generation and dissipation terms. When averaging over a large ensemble of days, the tendency term in the energy or enstrophy budget will effectively be zero so the effects of the wave–wave interactions must be balanced by the effects of generation and dissipation for a given value of n.

In truncating (4) or (6), we wish to retain all terms that correspond to waves resolvable by the original data.

If it is assumed that four grid points are required to resolve a wave adequately, the limit of resolution of our data is near zonal wavenumber $m = 18$. With comparable data reliability in both latitude and longitude, the limit of resolution in latitude as measured by the one-dimensional index $n - m$ (the number of zeroes of $P_n^m(\mu)$ between the poles) is also 18. However, for the sake of easy comparison with earlier studies, we have employed triangular truncation at $n = m = 30$ in order to retain information on higher order analysis modes that are present (e.g., Chen and Wiin-Nielsen, 1978). The effect of differing truncations on the nonlinear interaction statistics is also discussed in the Appendix. The results converge for increasing truncation even though the values of I_n^m or J_n^m are, in general, a function of the truncation (see Appendix). The values of I_n or J_n appear to be insensitive to the truncation for $n \leq 14$.

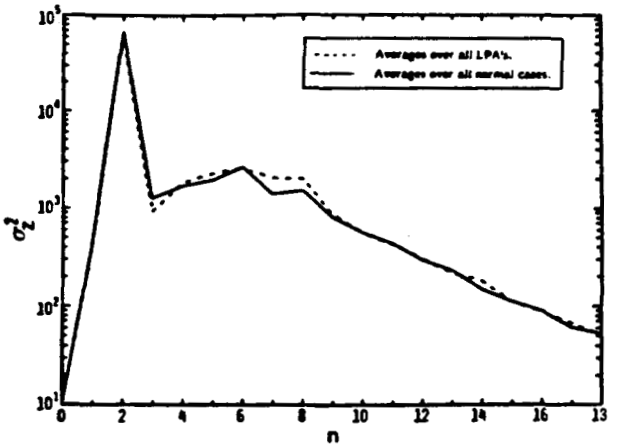

FIG. 1. Geopotential height variance σ_z^2 versus n for the 500 mb level.

4. Results

a. Spectra

Austin (1980) has shown that blocking situations are characterized by large amplitudes and normal phases for the zonal harmonic wavenumbers $m = 1$, 2, and 3. Pacific blocks in the mean exhibit greater amplitude for $m = 2$ and 3 while Atlantic blocks normally exhibit greater amplitude in wavenumbers 1 and 2.

To illustrate the characteristic signature of LPAs in the two-dimensional index n, let us first consider the spectrum of geopotential height variance,

$$\sigma_z^2 = \sum_{n=0}^{\infty} \left(\sum_{m=0}^{n} Z_n^m \right); \tag{14}$$

Z_n^m, the amplitude of spherical harmonic (n, m) for the 500 mb geopotential height, follows straightforwardly from the expansion of z in a series similar to (4). Figure 1 shows that the largest difference in σ_z^2 between LPAs and the balance of the data occurs at $n = 7, 8$ where LPAs have a greater variance. The LPAs also have slightly greater variance at $n = 5$ and slightly less at $n = 3$.

Examination of K and E spectra brings out an index band where differences between LPAs and the remainder of the sample are more systematic. The LPAs have greater kinetic energy in roughly the range $6 \leq n \leq 9$ (Fig. 2). The average increase in $\sum_{n=6}^{9} K_n$ is 30 percent for the LPAs compared to all other days. The statistical significance of this increase was tested with a two-sided t-test (Panofsky and Brier, 1958) assuming 5 days between independent samples of the 500 mb height. The differences in the K_n spectra are significant with greater than 99 percent confidence at $n = 7$, 95 percent at $n = 8$, and 90 percent at $n = 6$. The differences in K_n for the Atlantic cases alone are greatest at $n = 6, 7$ while the Pacific cases show particularly prominent differences at $n = 7, 8$ with smaller differences at $n = 6$ and 9 (not shown). Differences in the enstrophy spectrum (Fig. 3) closely follow those in K_n since $E_n = [n(n + 1)/a^2]K_n$. The stationary contribution to the K_n and E_n spectra was computed from the 15 January mean streamfunctions and is also displayed in Figs. 2 and 3. Note that the climatological mean stationary waves make significant contributions to the total K_n, for example, only for $n \leq 6$. For $n \geq 10$, the spectrum is dominated by transient waves (see also Boer and Shepherd, 1983).

Larger values of K_n or E_n imply greater dissipation since the dissipation is most likely related to the intensity of the wind in some way. Therefore, we might ask what mechanisms balance this dissipation and allow the noted increases in K_n and whether smaller scale waves act in a dissipative role.

b. Nonlinear exchange

We must keep in mind the inherent artificiality of describing atmospheric fluctuations in terms of the chosen (or any other) basis functions. The results for individual wavenumbers are often difficult to interpret. Therefore, it is traditional to form ensembles of wavenumbers with which to synthesize desired components of the flow (Saltzman and Fleisher, 1960; Wiin-Nielsen et al., 1963; Blackmon, 1976; Hansen and Chen, 1982). By analogy with the basic properties of Fourier transforms, these ensembles of wavenumbers allow specific features of the circulation to be synthesized (e.g.,, Hansen and Chen, 1982).

Blackmon (1976) has shown that geopotential height fluctuations with periods of 10–90 days are most important in the wavenumber regime, $7 \leq n \leq 12$. Lesser contributions to fluctuations of this period are made in the $1 \leq n \leq 6$ range. This is consistent with our finding that the major difference in the kinetic energy

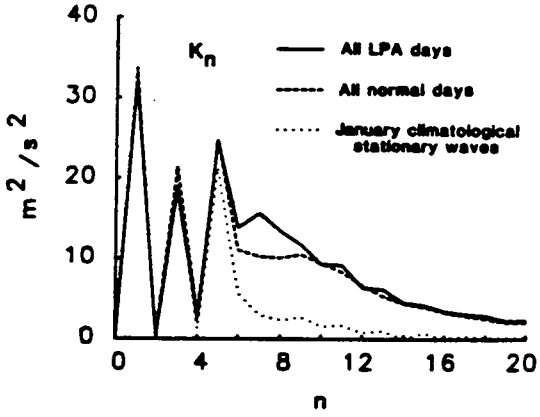

FIG. 2. Kinetic energy K_n versus n for the 500 mb level for LPA events (solid line); non-LPA events (dashed line) and for the 15 January climatological mean stationary waves (dotted line).

spectra between LPAs and the balance of our data occur in the range $6 \leq n \leq 9$.

The selection of the wavenumber ensembles we shall use presently was based on the differences in the spectra and was motivated as follows. First of all, harmonics with $1 \leq n \leq 5$ are grouped together because these modes represent the gross, mean features of the circulation and are very steady in time (Blackmon, 1976; Boer and Shepherd, 1983). In the present dataset, the content of K_n and E_n for $1 \leq n \leq 5$ is due almost entirely to the climatological mean waves (Fig. 2). In addition, there is virtually no difference in the mean K_n spectra, for example, between LPAs and the other situations for these modes (Fig. 2).

A second ensemble is formed from the harmonics with $6 \leq n \leq 9$. This grouping is due to the mean increase in the K and E content of this ensemble during LPA events. Note that this ensemble contains zonal wavenumbers from $m = 0$ through $m = 9$ and includes 18 different spherical harmonics. Thus, depending on the relative amplitudes and phases of the components in specific realizations, relatively localized features can be described. A third ensemble corresponding to smaller two-dimensional scale waves is formed from waves with $n \geq 10$. These ensembles provide a convenient way to visualize the results, but they are by no means unique. For example, based on differences in the cascading alone, ensembles for $1 \leq n \leq 3$ and $4 \leq n \leq 10$ could be justified.

The formation of wavenumber ensembles in the two-dimensional index is not directly analogous to the procedure in the one-dimensional index used, for example, by Hansen and Chen (1982). Each of our three chosen ensembles for the index n contains zonal harmonic wavenumbers of planetary scale (e.g., Blackmon, 1976). However, these waves have different latitudinal scales and therefore different two dimensional indices.

The results of the calculation of I_n and J_n are presented in Tables 2 and 3, respectively.

The gain in energy for the $1 \leq n \leq 5$ ensemble is reduced during LPA events. This change is entirely due to the change at $n = 3$ which is partially offset by the changes at $n = 4$ and 5. Differences in the enstrophy cascade for this ensemble are small. However, we can see that in the range of $6 \leq n \leq 9$, when all the positive anomaly cases are taken together, there is a reversal in the sign of the kinetic energy *and* enstrophy cascade compared to the balance of the sample. That is, during the positive anomaly events, waves with $6 \leq n \leq 9$ gain both kinetic energy and enstrophy from the other waves due to wave–wave interactions, whereas at other times, this ensemble loses a comparable amount of K_n and E_n due to the same mechanism. The source of this energy and enstrophy is the higher n waves, especially those for which $10 \leq n \leq 14$, a region of the spectrum dominated by transient eddies (e.g., Fig. 2 of Boer and Shepherd, 1983). The difference in the kinetic energy cascade between LPA and non-LPA days, ΔI_n, is illustrated in Fig. 4. The implication is that smaller two-dimensional scale transients are making positive contributions to both the energy and enstrophy budgets of the LPA pattern during these events. This is a somewhat remarkable result considering the global-scale treatment of the data used here. These results represent average interactions over the entire Northern Hemisphere.

When the LPA events are subdivided into Atlantic and Pacific cases, the reversal of the cascades for the $6 \leq n \leq 9$ regime is much more pronounced for the Atlantic cases. For the Pacific cases, the enstrophy cascade also reverses but the kinetic energy added to this band due to wave–wave interactions is small.

Using the same procedures used with the energy spectra, tests of the statistical significance of the differences in I_n indicate greater than 99 percent confidence in the differences at $n = 3$, $n = 8$ and $n = 13$. At $n = 3$, the difference is due to a much smaller rate of gain of K_3 due to nonlinear interactions for LPA events.

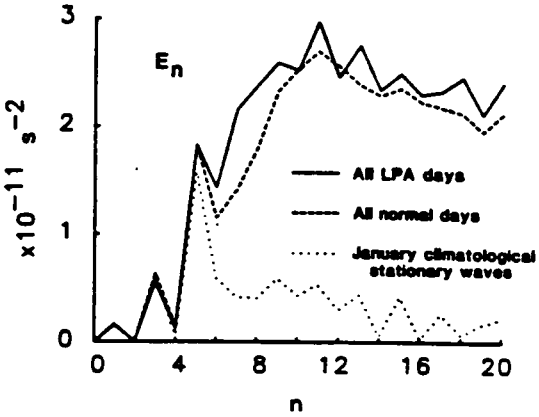

FIG. 3. Enstrophy E_n versus n for the 500 mb level for LPA events (solid line); non-LPA events (dashed line) and for the 15 January climatological mean stationary waves (dotted line).

TABLE 2. Time mean of I_n, the nonlinear kinetic energy exchange, for the various data samples. In this and subsequent tables, numbers to the right of the braces indicate sums over each wavenumber group. Units are 10^{-7} m^2 s^{-3}.

n	All non-LPA days		All LPA days		Atlantic LPA days		Pacific LPA days	
1	0		0		0		0	
2	−5		−2		−4		−1	
3	363	+550	213	+504	244	+473	201	+552
4	38		69		63		79	
5	154		224		170		273	
6	−12		31		91		−113	
7	−163	−143	−164	+126	−66	+282	−198	−29
8	70		224		221		261	
9	−38		35		36		21	
10	−71		−57		−99		8	
11	−120		−180		−220		−158	
12	−60		−93		−138		−56	
13	−34		−169		−182		−142	
14	−39		−92		−90		−97	
15	−77		−78		−93		−109	
16	−54		−35		−49		−26	
17	−64		−62		−53		−72	
18	−25		−38		−24		−45	
19	−8		0		4		9	
20	−17	−407	−36	−630	−40	−755	−35	−523
21	−9		11		17		12	
22	27		27		12		54	
23	15		−2		30		−38	
24	11		35		27		54	
25	22		38		35		32	
26	14		9		14		−10	
27	15		9		8		1	
28	22		35		31		35	
29	26		17		13		15	
30	19		31		42		36	

The difference at $n = 8$ represents a large increase in the rate of gain of K_8 due to nonlinear interactions and the difference at $n = 13$ represents a very large increase in the export of kinetic energy from $n = 13$ during LPA events. These statistically significant changes are consistent with the observed differences in the respective wavenumber ensembles in which these values of n occur (Table 2). These changes can easily be interpreted to indicate that on average during LPA events a greater amount of K_n (or E_n) is exported from the transient, high-index scales of motion (specifically $n = 13$) to the $n = 8$ region of the spectrum with less cascade toward very large scales, especially $n = 3$.

The large, significant changes in I_n at $n = 3$ and $n = 13$ are not accompanied by significant changes in K_n at these index values (although K_3 declines as one might expect if I_n is an important term in its budget), suggesting that nonlinear effects are compensated in some way. However, at $n = 8$ the significant increase in K_n is accompanied by a significant increase in the nonlinear contribution toward its maintenance. The increase in K_n at $n = 7$, on the other hand, requires an alternative, most likely baroclinic, energy source.

Our results by no means afford an explanation of the existence of the LPAs, but they do indicate the potential importance of cyclone-scale and small-scale transients in the maintenance of the LPA patterns, at least in a statistical sense. Saltzman (1959) first suggested that wave–wave interactions could act to maintain the quasi-permanent centers of action. More recently, Holopainen and Oort (1981) revived this idea and showed that transient eddies act to maintain the local energy and enstrophy balance of midlatitude, time-mean, standing waves as noted earlier. In the present context, wave–wave interactions act to diminish the K_n and E_n for modes in the $6 \leqslant n \leqslant 9$ bands during "normal" circulations. When the LPA subset (roughly ⅓ of the total sample) is examined, the noted reversal of this tendency appears.

We can also construct results for interactions in the one-dimensional index m, the zonal wavenumber, but these are not directly comparable to conventional studies of cascading in this one-dimensional index because the present results include interactions amongst all wavenumbers including the zonal mean wind components, $m = 0$. Conventional studies treat this wave–mean flow interaction separately (Saltzman, 1970). Nonetheless, if we compute the difference between

$$I_m = \sum_n I_n^m \quad \text{or} \quad J_m = \sum_n J_n^m \qquad (15)$$

TABLE 3. Time mean of J_n, the nonlinear enstrophy exchange, for the various data samples, as in Table 2. Units are 10^{-18} s^{-3}.

n	All non-LPA days		All LPA days		Atlantic LPA days		Pacific LPA days	
1	0		0		0		0	
2	0		0		0		0	
3	11	24	6	26	7	23	6	30
4	2		3		3		4	
5	11		17		13		20	
6	−1		3		9		−12	
7	−23		−23		−9		−27	
8	12	−20	40	28	39	47	46	12
9	−8		8		8		5	
10	−19		−15		−27		2	
11	−39		−58		−71		−52	
12	−23		−36		−53		−21	
13	−15		−76		−82		−64	
14	−20		−47		−46		−50	
15	−45		−46		−55		−65	
16	−36		−24		−33		−18	
17	−48		−47		−40		−54	
18	−21		−32		−20		−38	
19	−8		0		3		9	
20	−18	−4	−37	−54	−42	−70	−37	−42
21	−10		13		19		14	
22	34		33		16		68	
23	20		−3		40		−51	
24	16		51		39		80	
25	35		61		57		52	
26	24		16		24		−1	
27	27		17		15		1	
28	44		69		63		71	
29	55		35		27		31	
30	43		72		96		81	

for the LPA events and the remainder of the dataset, differences similar to those found by Hansen and Sutera (1984) appear for the Atlantic cases (Table 4). In the mean for these cases, zonal wavenumbers 1–4 gain a large positive increment in K_m and E_m due to barotropic processes while the zonal mean flow ($m = 0$) receives less E and substantially less K during the Atlantic LPA events. For the Pacific cases, the zonal mean flow experiences even greater deficits from barotropic processes, but the enhanced upscale transfer from intermediate to large-scale waves does not appear.

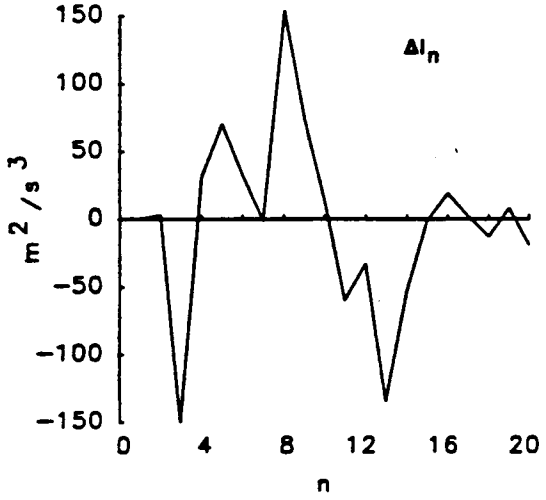

FIG. 4. The difference between the kinetic energy cascade for LPA events and all other times, ΔI_n, as a function of n. Results are only plotted for $n \leq 20$. For higher values of n, the differences are small (See Table 2). See text for interpretation of this figure.

In addition, results for a meridional index, $n - m$, can be constructed. We have arbitrarily grouped these waves in ensembles for $n - m = 1$ to 5, $n - m = 7$ to 15, and $n - m = 17$ to 29 for comparisons (Table 4 and Table 5). Note that the major differences between LPAs and the mean for other days in the sample occur at the low wavenumber end of the spectrum at $n - m = 5$. Modes with $n - m = 5$ roughly double their gain in kinetic energy, and their enstrophy cascade reverses. Similar characteristics appear when the LPA events are subdivided into Atlantic and Pacific cases (Table 5). Notice that the general characteristics of the nonlinear cascading in the meridional index are very similar to studies of cascading in the more conventional zonal index, m (Steinberg et al., 1971). In general, the differences in the one-dimensional indices at $1 \leq m \leq 4$ and $n - m = 5$ are consistent with the two-dimensional changes for $6 \leq n \leq 9$. The cascade of energy

TABLE 4. Differences, ΔI_j and ΔJ_j, in the nonlinear exchange of energy and enstrophy between the noted LPA events and the normal statistics for spectral index j. The results are listed for the various wave ensembles. Units for ΔI_j are 10^{-7} m^2 s^{-3} and for ΔJ_j are 10^{-18} s^{-3}.

	All LPA cases	Atlantic LPA cases	Pacific LPA cases	All LPA cases	Atlantic LPA cases	Pacific LPA cases
n		ΔI_n			ΔJ_n	
1–5	−46	−77	2	2	−1	6
6–9	269	425	114	48	67	32
10–30	−223	−348	−116	−50	−66	−38
m		ΔI_m			ΔJ_m	
0	−140	−74	−175	−24	−10	−35
1–4	46	158	−3	19	61	2
5–12	69	−120	160	−35	−99	2
13–30	25	36	18	40	48	31
$n-m$		ΔI_{nm}			ΔJ_{nm}	
1–5	325	237	318	79	31	91
7–15	−372	−297	−351	−136	−108	−122
17–29	47	60	33	57	−77	31

into the portion of the spectrum representing LPAs comes from eddies of smaller zonal and meridional scale.

5. Conclusion

Locally defined height anomalies leave statistically significant signals in hemispheric-scale circulation statistics. The major average differences in the kinetic energy and enstrophy spectra between the large, positive, persistent 500 mb height anomalies identified by Charney et al. (1981) and more normal circulations occur in the two-dimensional spectral index band $6 \leqslant n \leqslant 9$. The LPA events achieve both greater K_n and E_n on average in this region of the spectrum. Differences elsewhere are negligible. Statistically significant differences in the nonlinear cascading occur at $n = 3$, where less K and E are gained; at $n = 8$, where a tripling in the amount of K and E gained occurs; and at $n = 13$, where a very large increase in the amount of K and E lost occurs. Only the change in cascading at $n = 8$ is accompanied by a statistically significant change in K_n or E_n. These results imply that during LPA events, smaller two-dimensional scale transients add K and E to the wavenumbers characterizing the LPAs whereas during more zonal circulations wave–wave interactions act to dissipate this ensemble. Examination of differences in the cascading in 1 dimensional indices indicates that the transport of energy and enstrophy to the LPAs comes from eddies of both smaller zonal and

TABLE 5. Time mean of $I_{nm} = \sum_{n-m=\text{constant}} I_n^m$ and $J_{nm} = \sum_{n-m=\text{constant}} J_n^m$, the nonlinear exchanges of K and E in the meridional index, $n - m$. Wavenumber group sums are given to the right of braces. Units for I_{nm} are 10^{-7} m^2 s^{-3} and for J_{nm} are 10^{-18} s^{-3}.

	I_{nm}				J_{nm}			
$n-m$	Non-LPA days		LPA days		Non-LPA days		LPA days	
1	−68		−107		−16		−23	
3	116	340	143	665	−43	−75	−42	4
5	292		629		−16		69	
7	−194		−353		−37		−81	
9	−27		−125		−8		−43	
11	−108	−428	−182	−800	−40	−108	−70	−244
13	−57		−116		−18		−58	
15	−42		−24		−5		8	
17	−3		10		14		27	
19	17		25		38		45	
21	30		58		47		94	
23	23	58	40	135	39	183	67	240
25	18		1		38		1	
27	−1		−5		−3		−7	
29	4		6		10		13	

meridional extent. This suggests that the transients may play a regime dependent role in the dynamics of persistent circulation anomalies. The relative importance of these barotropic processes is an important question for further study. The study should be extended to determine the role of transient eddy heat transports in the dynamics of the anomalies. These results certainly do not imply that turbulent interactions alone are responsible for the existence of the anomalies. However, they do imply that the transients cannot be ignored or treated strictly as dissipative agents.

Acknowledgments. The authors names are listed in alphabetical order. This work was supported by the Division of Atmospheric Sciences of the National Science Foundation and under Grant ATM-8403372 at Control Data Corporation and under Grant ATM-8106034 at the Center for The Environment and Man, Inc. (CEM). One of us (ARH) was also supported by NASA under Grant NAS8-34903 while at Yale University. Computer support was provided by the National Center for Atmospheric Research (NCAR) which is sponsored by the National Science Foundation. The authors are grateful to Dr. Alfonso Sutera of CEM for numerous stimulating discussions, to Dr. Grant W. Branstator of NCAR for providing computer programs used for the harmonic analyses, to Prof. Michael Ghil of the Courant Institute for a helpful discussion in the planning stages of this project, and to Dr. G. D. Robinson of CEM for his guidance.

APPENDIX

Estimate of Truncation Error

In order to examine the energetics of LPAs and of normal flow, it is necessary to rely upon results that depend on derivatives of the basic variables in spite of inherent problems in evaluating such derivatives. The presence of higher order derivatives in the Jacobian form of (10), along with the nonlinearity of the expression, cause particular computational problems in evaluating the q_n^m, r_n^m (Eq. 13) that determine the wave–wave interaction coefficients. These derivatives may be calculated by finite differences or by term-by-term differentiation of series expansions. Finite differences introduce considerable truncation error, and so we have chosen the latter method of calculation. The termwise differentiation approach is not without problems either, due to the fact that the higher wavenumber, less reliable (i.e., more poorly resolved) components are amplified substantially in the differentiation process. Construction of the expansion for $\zeta(=\nabla^2\psi)$, for example, entails multiplication of ψ-coefficients by the factor $n(n+1)$ by virtue of the relation

$$\nabla^2\begin{Bmatrix}\cos m\lambda\\ \sin m\lambda\end{Bmatrix}P_n^m(\mu) = \frac{-1}{a^2}\,n(n+1)\begin{Bmatrix}\cos m\lambda\\ \sin m\lambda\end{Bmatrix}P_n^m(\mu). \tag{A-1}$$

It follows further that in the series for $\partial\zeta/\partial\mu$, the ψ-coefficients (A_n^m, B_n^m) are multiplied by factors that are $O(n^3)$. Derived expansions of this type are used to evaluate each of the for derivatives comprising the Jacobian.

When the expansions for the derivatives are used to form the product terms found in (10), interactions occur between waves of different index. In particular, high wavenumber harmonics interact to form lower-wavenumber harmonics in the resultant expansion for J. Due to this situation, the calculated components of J are found to vary even at the lower wavenumbers as

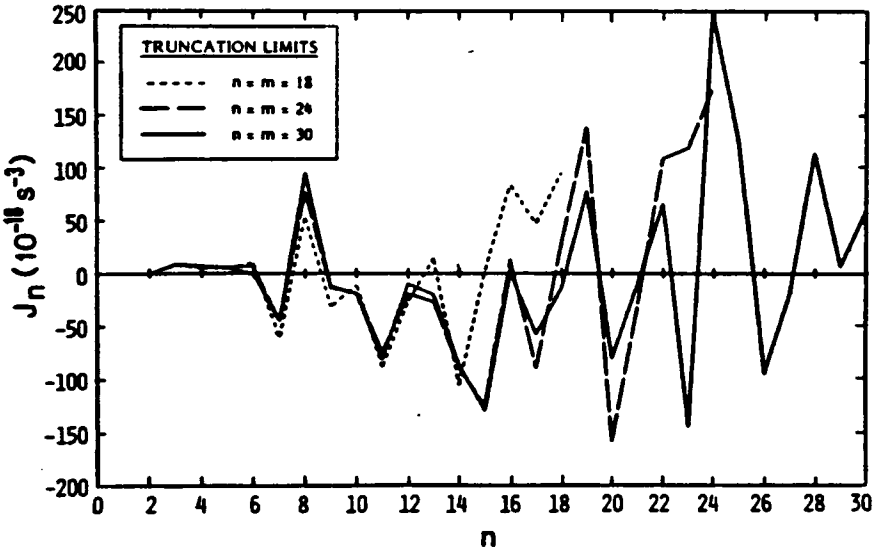

FIG. 5. J_n for the 24 LPA days in January 1963 for three different truncations.

the truncation limit is changed. Increasing the truncation limit of the individual series does not guarantee convergence of the results, however, since raising the limit serves to append components that are more poorly resolved and at the same time weighted more heavily. The high-wavenumber error in the differentiated series is distributed to the lower-wavenumber components as a result of the multiplications. Figure 5 shows the behavior of J_n versus n at 500 mb where the spectral coefficients have been averaged over the 24 LPA days of January 1963. The computations have been performed using triangular truncation with limits 18, 24 and 30. As the truncation is increased, the results for the 3 different truncations converge quite well for roughly $n \leq 14$. Comparing the truncations at $n = 24$ and $n = 30$ alone, the results appear to converge reasonably well for roughly $n \leq 18$.

REFERENCES

Austin, J. F., 1980: The blocking of middle latitude westerly winds by planetary waves. *Quart. J. Roy Meteor. Soc.*, **106**, 327–350.

Baer, F., 1972: An alternate scale representation of atmospheric energy spectra. *J. Atmos. Sci.*, **29**, 649–664.

Blackmon, M. L., 1976: A climatological spectral study of the 500 mb geopotential height of the Northern Hemisphere. *J. Atmos. Sci.*, **33**, 1607–1623.

Boer, G. J., and T. G. Shepherd, 1983: Large-scale two-dimensional turbulence in the atmosphere. *J. Atmos. Sci.*, **40**, 164–184.

Charney, J. G., J. Shukla and K. C. Mo, 1981: Comparison of a barotropic blocking theory with observation. *J. Atmos. Sci.*, **38**, 762–779.

Chen, T. C., and A. Wiin-Nielsen, 1978: On nonlinear cascades of atmospheric energy and enstrophy in a two-dimensional spectral index. *Tellus*, **30**, 313–322.

Ellsaesser, H. W., 1966: Expansion of hemispheric meteorological data in antisymmetric surface spherical harmonic (Laplace) series. *J. Appl. Meteor.*, **5**, 263–276.

Fredrickson, J. S., 1979: The effects of long planetary waves on the regions of cyclogenesis: Linear Theory. *J. Atmos. Sci.*, **36**, 195–204.

Hansen, A. R., and T. C. Chen, 1982: A spectral energetics analysis of atmospheric blocking. *Mon. Wea. Rev.*, **110**, 1146–1165.

——, and A. Sutera, 1984: A comparison of the spectral energy and enstrophy budgets of blocking versus nonblocking periods. *Tellus*, **36A**, 52–63.

Hobson, E. W., 1931: *The Theory of Spherical and Ellipsoidal Harmonics*. Cambridge University Press, 500 pp.

Holopainen, E. O., and A. H. Oort, 1981: On the role of large-scale transient eddies in the maintenance of the vorticity and enstrophy of the time-mean atmospheric flow. *J. Atmos. Sci.*, **38**, 270–280.

——, L. Rontu and N. C. Lau, 1982: The effect of large-scale transient eddies on the time-mean flow in the atmosphere. *J. Atmos. Sci.*, **39**, 1972–1984.

Kallen, E., 1981: The nonlinear effects of orographic and momentum forcing in a low-order, barotropic model. *J. Atmos. Sci.*, **39**, 2100–2163.

——, 1982: Bifurcation properties of quasi-geostrophic, barotropic models and their relation to atmosphere blocking. *Tellus*, **34**, 255–265.

Lambert, S. J., 1981: A diagnostic study of global energy and enstrophy fluxes and spectra. *Tellus*, **33**, 411–414.

Lau, N.-C., and E. O. Holopainen, 1984: Transient eddy forcing of the time-mean flow as identified by geopotential tendencies. *J. Atmos. Sci.*, **41**, 313–328.

Panofsky, H. A., and G. W. Brier, 1958: *Some Applications of Statistics to Meteorology*. The Pennsylvania State University Press, 224 pp.

Reinhold, B., and R. T. Pierrehumbert, 1982: Dynamics of weather regimes: Quasi-stationary waves and blocking. *Mon. Wea. Rev.*, **110**, 1105–1145.

Saltzman, B., 1959: On the maintenance of large-scale quasi-permanent disturbances in the atmosphere. *Tellus*, **11**, 427–431.

——, 1970: Large-scale atmospheric energetics in wavenumber domain. *Rev. Geophys. Space Phys.*, **8**, 289–302.

——, and A. Fleisher, 1960: The exchange of kinetic energy between larger scales of atmospheric motion. *Tellus*, **12**, 374–377.

Steinberg, H. L., A. Wiin-Nielsen and C. H. Yang, 1971: On nonlinear cascades in large-scale atmospheric flow. *J. Geophys. Res.*, **76**, 8629–8640.

Youngblut, C., and T. Sasamori, 1980: The nonlinear effects of transient and stationary eddies on the winter mean circulation. Part I: Diagnostic analysis. *J. Atmos. Sci.*, **37**, 1944–1957.

Van den Dool, H. M., 1983: A possible explanation of the observed persistence of monthly mean circulation anomalies. *Mon. Wea. Rev.*, **111**, 539–544.

Wiin-Nielsen, A., J. A. Brown and M. Drake, 1963: On atmospheric energy conversions between the zonal flow and the eddies. *Tellus*, **15**, 261–279.